


2005

Molecular Dynamics Simulations of Amphiphilic Molecules

Roger L. McMullen Jr.
Seton Hall University

Follow this and additional works at: <https://scholarship.shu.edu/dissertations>

 Part of the [Biological and Chemical Physics Commons](#), and the [Chemistry Commons](#)

Recommended Citation

McMullen Jr., Roger L., "Molecular Dynamics Simulations of Amphiphilic Molecules" (2005). *Seton Hall University Dissertations and Theses (ETDs)*. 1304.

<https://scholarship.shu.edu/dissertations/1304>

Molecular Dynamics Simulations of Amphiphilic Molecules

by

Roger L. McMullen, Jr.

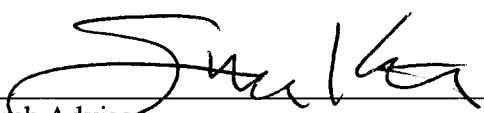
Dissertation

Submitted to the Department of Chemistry and Biochemistry and the Graduate School of Arts and Sciences at Seton Hall University in partial fulfillment of the requirements for the degree of Doctor of Philosophy

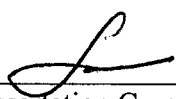
2005

We certify that we have read this thesis and that in our opinion it is adequate in scientific scope and quality as a dissertation for the degree of Doctor of Philosophy.

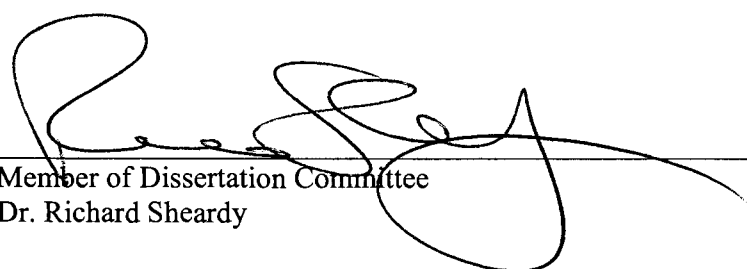
Approved



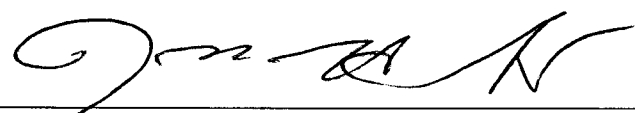
Research Advisor
Dr. Stephen P. Kelty



Member of Dissertation Committee
Dr. Alexander Fadeev



Member of Dissertation Committee
Dr. Richard Sheardy



Approved for the Department of Chemistry and Biochemistry
Chairman, Department of Chemistry and Biochemistry
Dr. Nicholas Snow

Dedication

To the Late Roger L. McMullen

Acknowledgements

It would be most appropriate to start this section by paying my most humble respects to the one who has guided me on this journey for the last six years. My adviser, Dr. Stephen P. Kelty, and I have had a wonderful working relationship throughout this time and I hope we can continue it in the future. The story began when a young student went knocking at the door of Professor Kelty some six years ago. It is difficult to imagine what he thought when a student approached him with such a wild idea as to study human hair fibers. However, without hesitation Dr. Kelty eagerly embraced this endeavor which eventually became a successful story in science. We learned and shared with others many interesting and important details about the fine structure of human hair. I am very grateful for all of the knowledge Dr. Kelty shared with me on this undertaking as well as our more recent journey into the world of Molecular Dynamics Simulations. Steve, I hope in the future we can continue our occasional evening gatherings consisting of intellectual conversation along with a cup of fresh-pressed coffee.

Throughout my residency at Seton Hall University, several people have come and gone from our research group. It is fitting to first mention Chang Kim, who I have spent the most time with at SHU, as well as some of our former group members (Deborah Hills-Haney and Chris Jurgensen). More recently, Fang Mou has joined the group and I wish him continued success during his time at SHU. Through group meetings or just from laboratory conversation, many ideas have been shared among us and I am indebted to each of you for input and discussion.

Many thanks are due to Professors Sheardy and Fadeev. Both were readers of this dissertation as well as committee members for the matriculation exam. Such matters require a great deal of dedication and professionalism on the part of the readers. Once again, thank you both. In addition, I would also like to thank the other members of the matriculation examination board who were Doctors Snow and Murphy.

I would like to take the opportunity to express my sincere gratitude to some of my colleagues at work, especially Tim Gillece and John Katirgis. During the years that I embarked on this journey, there were many times that I entered their laboratory in search of scientific advice and they unselfishly shared their wealth of knowledge. I would also like to thank Tim and John again, as well Sam D'Archangelis and Herb Ulmer, for previewing several of my presentations and providing honest, critical, and constructive criticism. In addition, I am also indebted to my very good friend and colleague, Bret Clark, who on many occasions has been extremely unselfish with his time and very supportive throughout.

During the time I spent working in the area of molecular dynamics simulations, I came into contact with many people in this field who have helped me in many ways. Briefly, the help of Ryan Dougherty, a student at North Carolina University, was invaluable in helping me with the program Swiss PDB Viewer. I would like to especially express my gratefulness to the GROMACS development crew and all participating members of the GROMACS mailing list. This has been a great forum where one is able to learn such valuable information from leading experts in the field.

Aside from professional debts of gratitude, there were many who played vital roles in my personal life, providing support, hope, and happiness throughout this period. It is with great sadness that I complete this degree in the absence of my father. I am very grateful to my parents for their pride and support throughout these years, but especially to my father who never doubted my ability to complete this expedition. The last year was extraordinarily difficult and I was only able to bring it to a conclusion with the help of another. Thank you, Silvia, for breathing fresh air into my life.

Last, my indebtedness goes to Dr. Janusz Jachowicz. Over the last nine years, Janusz has been a mentor, instructor, and much cherished friend to me. I wish to thank him for his unselfish support in allowing me to set out and complete this venture. It has required a great deal of patience on his part as a supervisor. In addition, he has always been encouraging of this work, from the very beginning when we were studying hair fibers with scanning probe microscopy until much later during the molecular dynamics studies. Janusz, it is certain that some day I will look back upon this period as the very best of times of my life. Thank you.

Table of Contents

<u>Chapter</u>	<u>Page</u>
Dedication	ii
Acknowledgements	iii
List of Tables	vii
List of Figures	viii-xii
Abstract	xiii-xiv
I. Introduction	1
II. Computational Methods	20
III. Molecular Dynamics Simulations of Langmuir Monolayers	54
IV. Molecular Dynamics Simulations of Phospholipid Bilayers	87
V. Scanning Probe Microscopy of Human Hair Fibers	110
VI. References	136
VII. Appendix A. Suggested Reading	144
VIII. Appendix B. Computational Instructions	146

List of Tables

- I. The frequency of appearance of micropores in various types of hair. (Page 122)
- II. Coefficient of friction for various hair types based on average slopes of $\Delta(\text{LFM V})$ versus loading force plots. (Page 131)
- III. Column widths and PDB file information corresponding to Figure 72. (Page 150)
- IV. Column widths and Gromos file information corresponding to Figure 73. (Page 152)

List of Figures

- Figure 1.** Structures of two fatty acids investigated in this work. Please note that eicosanoic acid is often referred to as arachidic acid in the literature.
- Figure 2.** (a) Scanning electron microscope image of a human hair fiber. (b) 18-MEA covalently attached to the surface of hair. SEM micrograph courtesy of Dr. J. Jachowicz.
- Figure 3.** Diagram of a hair fiber cuticle cell. Reproduced from Ref. [5].
- Figure 4.** Schematic of a Langmuir trough.
- Figure 5.** Isothermal phase diagram of a hypothetical long chain amphiphile. Reproduced from Ref. [24].
- Figure 6.** Illustration of biological lipid bilayer membrane. Reproduced from Ref. [61].
- Figure 7.** Structures of the phospholipids studied in this work.
- Figure 8.** Inter- and intramolecular interactions described by molecular dynamics force fields.
- Figure 9.** The use of periodic boundary conditions in MD simulations. Adapted from Ref. [147].
- Figure 10.** Treatment of long-range electrostatic interactions in MD simulations.
- Figure 11.** Starting structure of a dual monolayer system of 18-MEA.
- Figure 12.** Typical series of steps followed in a molecular dynamics simulation using GROMACS. Adapted from Ref. [159].
- Figure 13.** Starting arrangements for mixed bilayer systems of DMPC and DPPC
- Figure 14.** Plot of density as a function of distance along the z-axis of the simulation box for eicosanoic acid and H₂O.
- Figure 15.** Graphical representation of tilt angle for molecules containing long alkyl chains.
- Figure 16.** Graphical representation of the radial distribution function. Black circle = reference atom, grey circles = atoms that fall within selected radius, clear circles = all other atoms.

- Figure 17.** Radial distribution function between various atoms along the backbone of eicosanoic acid and the H₂O oxygen.
- Figure 18.** Deuterium NMR experimental order parameter (C-D vector orientation).
- Figure 19.** Bond order parameter as defined using united atom models in MD simulations.
- Figure 20.** Dihedral angle distribution for the first dihedral set (closest to the headgroup) in eicosanoic acid.
- Figure 21.** Isothermal phase diagram of several long chain fatty acids obtained from a Langmuir trough experiment. Please note arachidic acid refers to eicosanoic acid. Reproduced from Ref. [26].
- Figure 22.** Isothermal phase diagram of eicosanoic acid obtained from a molecular dynamics simulation. Reproduced from Ref. [51].
- Figure 23.** Isothermal phase diagram of eicosanoic acid obtained from a molecular dynamics simulation. Reproduced from Ref. [50].
- Figure 24.** Isothermal phase diagram of eicosanoic acid obtained from a molecular dynamics simulation.
- Figure 25.** Snapshots from MD simulations of Eicosanoic Acid at various packing densities.
- Figure 26.** Potential Energy as a function of packing density for eicosanoic acid.
- Figure 27.** Kinetic Energy as a function of packing density for eicosanoic acid.
- Figure 28.** Film thickness as a function of packing density for Eicosanoic Acid.
- Figure 29.** Monolayer tilt as a function of packing density for Eicosanoic Acid.
- Figure 30.** Monolayer tilt as a function of packing density for Eicosanoic Acid. Reproduced from Ref. [17].
- Figure 31.** Radial distribution function of Carbon-3 relative to Carbon-2 for Eicosanoic Acid at various packing densities.
- Figure 32.** Deuterium Order Parameters for Eicosanoic Acid as a function of chain length at various packing densities.
- Figure 33.** Fraction of dihedral angles in the *trans* conformation as a function of chain length for Eicosanoic Acid.

- Figure 34.** Isothermal phase diagrams of eicosanoic acid obtained using the indicated forcefields and united atom groups.
- Figure 35.** Isothermal phase diagrams of Eicosanoic Acid obtained using the Particle-mesh Ewald or Cut-Offs method for the treatment of long range electrostatics. $r_1 = 0.9$ nm, $r_2 = 1.4$ nm.
- Figure 36.** Isothermal phase diagrams of Eicosanoic Acid obtained using different system sizes.
- Figure 37.** Isothermal phase diagrams of Eicosanoic Acid obtained using Short Range and Long Range Cut-Offs with a 256 monolayer system.
- Figure 38.** Isothermal phase diagrams of Eicosanoic Acid after 1000 ps and 5000 ps.
- Figure 39.** Isothermal phase diagram of Eicosanoic Acid after compression from 18.5 \AA^2 to 17.5 \AA^2 .
- Figure 40.** Isothermal phase diagrams of Eicosanoic Acid obtained by expansion and compression of the simulation box.
- Figure 41.** Film thickness as a function of packing density for eicosanoic acid monolayer simulation under conditions of compression and expansion.
- Figure 42.** Deuterium Order Parameters for eicosanoic acid (compression simulation) as a function of chain length at various packing densities.
- Figure 43.** Snapshots from MD simulations of 18-MEA at various packing densities.
- Figure 44.** Film thickness as a function of packing density for eicosanoic acid and 18-MEA.
- Figure 45.** Monolayer tilt as a function of packing density for eicosanoic acid and 18-MEA.
- Figure 46.** Deuterium Order Parameters for 18-MEA as a function of chain length at various packing densities.
- Figure 47.** Snapshots from MD simulations of (a) DPPC and (b) DMPC after 50 ns.
- Figure 48.** Snapshots from MD simulations of (a) DPPC-DMPC I and (b) DPPC-DMPC II after 50 ns.
- Figure 49.** Packing density as a function of simulation time for lipid bilayers of DPPC, DMPC, DPPC-DMPC I, and DPPC-DMPC-II.

- Figure 50.** Plot of density as a function of distance along the z-axis of the simulation box for (a) DPPC and (b) DMPC.
- Figure 51.** Plot of density as a function of distance along the z-axis of the simulation box for (a) DPPC and (b) DMPC. Each figure contains plots for the pure, DPPC-DMPC I, and DPPC-DMPC II systems.
- Figure 52.** Deuterium order parameters as a function of chain length for both aliphatic chains of pure systems of DPPC and DMPC. Results from last 10 ns of the 50 ns simulation.
- Figure 53.** Deuterium order parameters as a function of chain length for the aliphatic chains (average of both chains) of a pure DPPC bilayer at various points during the simulation.
- Figure 54.** Deuterium order parameters as a function of chain length for the aliphatic chains (average of both chains) of DPPC from the DPPC-DMPC I bilayer at various points during the simulation.
- Figure 55.** Deuterium order parameters as a function of chain length for the aliphatic chains (average of both chains) of DPPC from the DPPC-DMPC II bilayer at various points during the simulation.
- Figure 56.** Deuterium order parameters as a function of chain length for the aliphatic chains (average of both chains) of DPPC from the pure, DPPC-DMPC I, and DPPC-DMPC II bilayers. Results from last 10 ns of the 50 ns simulation.
- Figure 57.** Deuterium order parameters as a function of chain length for the aliphatic chains (average of both chains) of DMPC from the pure, DPPC-DMPC I, and DPPC-DMPC II bilayers. Results from last 10 ns of the 50 ns simulation.
- Figure 58.** Radial distribution function of N-P pairs for DPPC. Results from last 10 ns of the 50 ns simulation.
- Figure 59.** Radial distribution function of P-H₂O and N-H₂O pairs for DPPC. Results from last 10 ns of the 50 ns simulation.
- Figure 60.** General scheme of a scanning probe microscope. Adapted from Howland *et. al.*
- Figure 61.** Typical image data scans (30 μ m) obtained during AFM/LFM analysis: (a) topography, (b) error signal, (c) LFM-Forward, (d) LFM-reverse.

- Figure 62.** Three-dimensional representation of topography.
- Figure 63.** (a) Error signal, (b) LFM-forward, and (c) LFM-reverse images (10 μm) for virgin hair, illustrating surface deposits on hair.
- Figure 64.** (a) Error signal, (b) LFM-forward, and (c) LFM-reverse images (10 μm) for solvent extracted hair.
- Figure 65.** Error signal image (10 μm) of solvent extracted hair revealing micro-pores on the hair surface.
- Figure 66.** Error signal image (10 μm) of virgin hair revealing micro-grooves on the surface.
- Figure 67.** Error signal images [(a) - 10 μm , (b) - 5 μm] of hair treated with PVP/MAPTAC.
- Figure 68.** (a) LFM forward, (b) LFM reverse, (c) Difference Image, and (d) Difference Image histogram for a 10 μm scan of solvent extracted hair.
- Figure 69.** Arbitrary voltage difference as a function of set point (normal force) for various hair treatment protocols. The average slope is reported for each data set.
- Figure 70.** Demonstration of the program Swiss PDB Viewer.
- Figure 71.** Calculations for simulation box vectors, based on desired packing density, for eicosanoic acid using Mathcad Plus 6.0.
- Figure 72.** Example of a PDB file construction using Microsoft Excel.
- Figure 73.** Example of a GRO file construction using Microsoft Excel.

Abstract

The molecular dynamics (MD) simulation method is a technique which falls under the umbrella of computational chemistry. During the last twenty years, this method has experienced explosive growth due to the significant advances that have been accomplished in computational architecture. We have employed this technique to probe the behavior of Langmuir monolayers as well as lipid bilayers. In our molecular dynamics simulations all atoms in the system under consideration are treated classically. Successive configurations of the system are generated by integrating Newton's laws of motion, resulting in a trajectory, which provides the positions and velocities of the particles as a function of time. Interactions between atoms consist of intramolecular (bonded) and intermolecular (non-bonded) interactions. Intramolecular interactions consist of bond stretching, bond angle, and dihedral interactions between covalently attached atoms. Intermolecular interactions, within a certain cut-off radius, occur between neighboring atoms and consist of van der Waals and electrostatic interactions. By performing MD simulations we are able to obtain conformational and thermodynamic information about the system under investigation. For example when studying systems with long alkyl chains, it is highly desirable to determine the tilt of the chains as well as the packing order (deuterium order parameter).

In the case of Langmuir monolayers, we examined the behavior of two different fatty acids, namely eicosanoic acid and 18-methyleicosanoic acid (18-MEA). The aim of this work was to gain an understanding the fundamental properties of 18-MEA by performing molecular dynamics simulations of Langmuir monolayers of this compound.

While this unusual anteiso fatty acid has been found in minor amounts in various biological materials, its presence in mammalian hair fibers as the major covalently bound fatty acid has inspired the research described herein. It is believed to form a monolayer at the surface of human and animal fibers and is covalently attached to underlying structural proteins by a thioester bond. We have completed a significant amount of work for eicosanoic acid (arachidic acid), which is the parent form of 18-MEA. In past studies of eicosanoic acid, it was reported that a phase transition occurs when performing an MD simulation in order to obtain an isothermal phase diagram. Our studies demonstrate that this transition is actually an artifact of the method employed in the simulation. Further, it has been found that molecular dynamic simulation studies of Langmuir monolayers of these compounds has provided some insight into the structure/function relationship of the methyl group position on the behavior of these fatty acids in thin films.

The investigated phospholipid lipid membranes consisted of pure and mixed systems of dipalmitoylphosphatidylcholine (DPPC) and dimyristoylphosphatidylcholine (DMPC). DPPC is the most studied lipid bilayer system, both experimentally and by MD simulations. Typically, DPPC and DMPC are the major phospholipids present in cell membrane structures. While these two phospholipids only differ in their length by two methylene groups, we have found significant differences in terms of their conformation behavior.

Chapter I

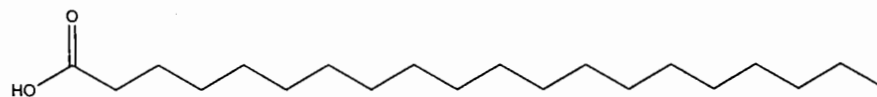
Introduction

Mozart's music is so pure and beautiful that I see it as a reflection of the inner beauty of the universe.

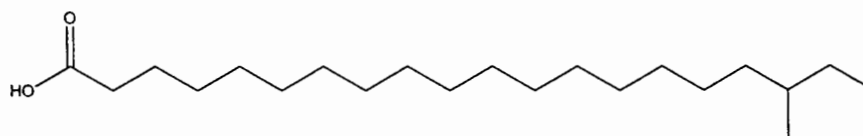
Dr. Albert Einstein

The aim of this work is to gain an understanding the fundamental properties of 18-methyl eicosanoic acid (18-MEA) by performing molecular dynamics simulations of Langmuir monolayers of this compound. Our interest in this fatty acid stemmed from earlier work we completed in the area of scanning probe microscopy studies of human hair fibers. We published two articles on this topic and have included an overview of this work in Chapter V. ^{1,2}

Our interest in 18-MEA arises from the presence of this unusual anteiso fatty acid in animal fibers. While it has been found in minor amounts in various biological materials, its presence in mammalian hair fibers as the major covalently bound fatty acid has inspired the research proposed herein. It is believed to form a monolayer at the surface of human and animal fibers and is covalently attached to underlying structural proteins by a thioester bond. ³⁻⁶ Figure 1 contains the structures of 18-MEA and its parent form, eicosanoic acid. For further illustration, Figure 2 provides a scanning electron microscope image of a human hair fiber along with a diagram that illustrates the covalent attachment of 18-MEA to the fiber surface. Please note that Figure 2b is an idealized diagram of 18-MEA bound to the surface of the fiber and it is likely that many molecules can be found on the surface, which are not covalently linked to the underlying protein.



eicosanoic acid – normal fatty acid

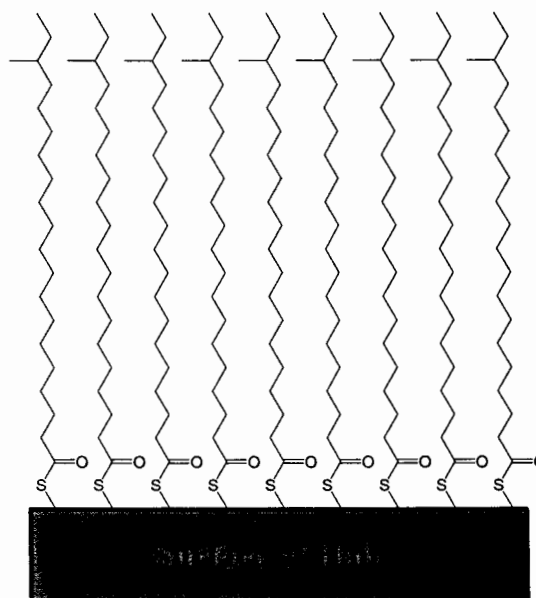


18-methyl eicosanoic acid (18-MEA) – anteiso fatty acid

Figure 1. Structures of two fatty acids investigated in this work. Please note that eicosanoic acid is often referred to as arachidic acid in the literature.



(a)



(b)

Figure 2. (a) Scanning electron microscope image of a human hair fiber. (b) 18-MEA covalently attached to the surface of hair. SEM micrograph courtesy of Dr. J. Jachowicz.

The morphological structure of human hair consists of an inner core, the cortex, which is surrounded by overlapping flat cuticle cells that are arranged in a manner analogous to fish scales or roof shingles. Each cuticle cell, which is *ca.* 0.5 μm thick and 60 μm square, consists of an Upper β -layer, A-layer, exocuticle, endocuticle, inner layer, and Lower β -layer (See Figure 3). These cuticular subcomponents are lamellar and arranged in the order listed above from the exterior of the fiber to its interior. The Upper and Lower β -layers constitute what is known as the cell membrane complex (CMC), which is unlike most biological phospholipid bilayer cell membranes. It is believed that the Upper β -layer, exposed to the surface and to overlying cuticle cells, consists predominantly of 18-MEA. Additionally, the cell membrane complex contains a δ layer, which is the intercellular cement that joins the Lower β -layer of one cuticle cell with the Upper β -layer of an underlying cuticle cell. The A-layer, exocuticle, and inner layer are thought to be proteinaceous in nature and have been shown to be extremely rich in disulphide bonds. The endocuticle, on the other hand, is generally low in cystine, but is also comprised of proteinaceous material. Human hair usually contains *ca.* 10 layers of cuticle cells at the root of the fiber, however, this number diminishes along the length of the fiber toward the tip direction (see Figure 3).⁵

In the past fifteen years a considerable amount of interest has evolved due to the detection of the unusual fatty acid, 18-MEA, on the surface of each cuticle cell.³⁻⁷ The current belief, in regard to the reason for its presence in human and animal fibers, is that 18-MEA possesses some special structure/function properties making it an essential component of the morphology of the hair fiber as well as the surface properties of hair.

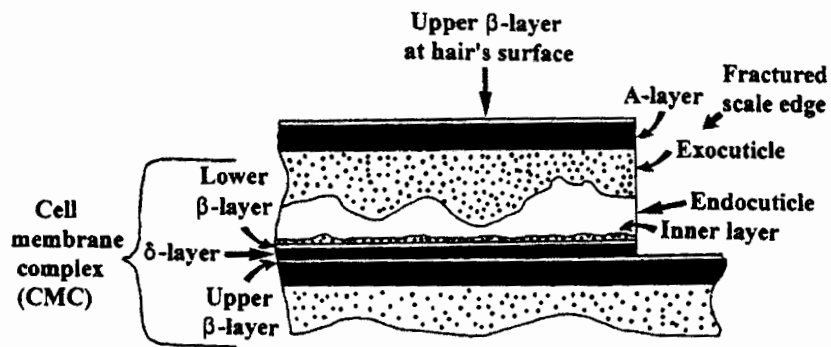


Figure 3. Diagram of a hair fiber cuticle cell. Reproduced from Ref. [5].

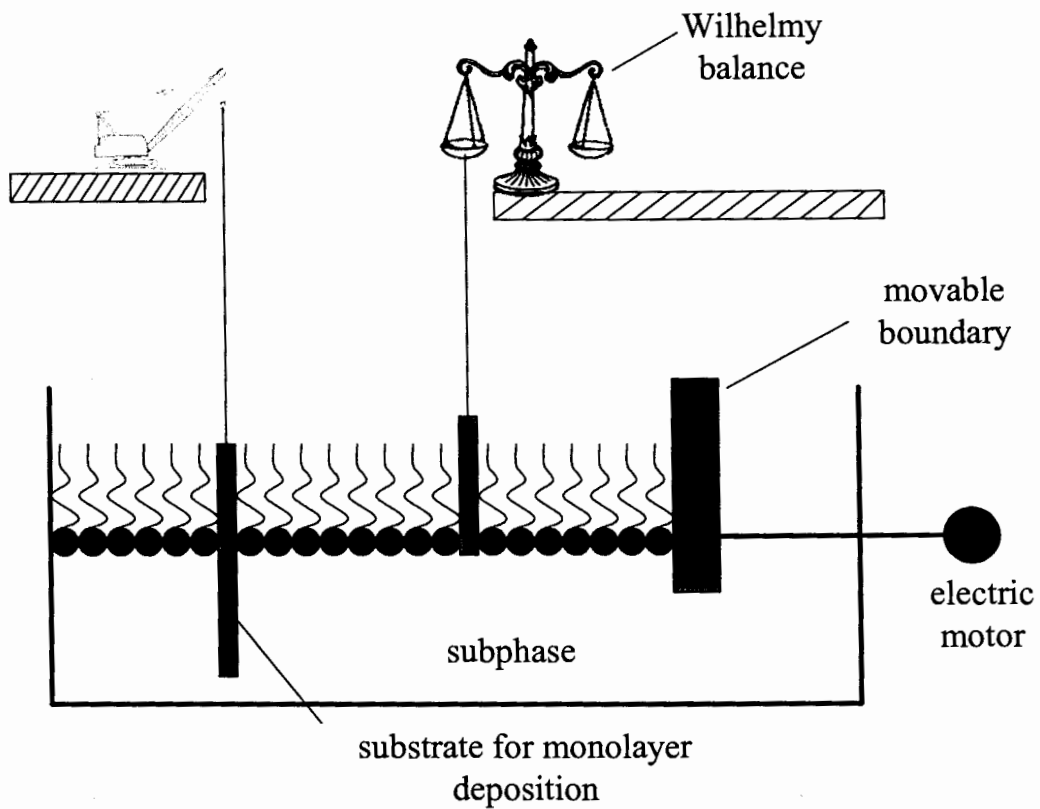


Figure 4. Schematic of a Langmuir trough.

For example, it has been shown that patients with Maple Syrup Urine Disease and are deficient in this fatty acid, possess hair fibers in which the cuticle cells are delaminated.⁸ Since this material is extremely difficult to synthesize and to obtain pure samples,⁹⁻¹² we have elected to utilize molecular dynamics (MD) simulations to study its behavior as a fatty acid monolayer. We have conducted a significant amount of research on its parent compound, eicosanoic acid, as it has been extensively studied experimentally, thus providing us with a link to experimental data.¹³⁻²¹ Furthermore, we have chosen to study molecular dynamics simulations of Langmuir monolayers of 18-MEA as it permits us to examine the conformational behavior of this fatty acid at various packing densities. Initially, we had postulated about simulating alkane thiol monolayers of this material since, in its natural state on hair, 18-MEA is covalently bound to the surface by a thioester cleavage. However, this would restrict our studies to the packing density permitted by a gold or silicon surface. To date, the packing density of this material on the surface of hair fibers is still unknown.⁴

We have also undertaken MD investigations of the dynamical behavior of phospholipid bilayer membranes. Specifically, we conducted MD simulations of pure and mixed bilayer systems of dipalmitoylphosphatidylcholine (DPPC) and dimyristoylphosphatidylcholine (DMPC). DPPC has been the most extensively studied bilayer forming phospholipid both experimentally and by molecular dynamics simulations. DMPC has also received considerable attention in the literature presumably due to its predominance in plasma membranes. Our interests in the studying these systems evolved from collaborations with Dr. George Turner from the Department of

Chemistry and Biochemistry at Seton Hall University. He is studying the behavior of Bacteriorhodopsin, which is integral membrane protein of the Halobacter halobium bacterium and is comprised of a bundle of seven α -helical rods. Professor Turner is modifying the integral protein by introducing proline substitutions to the protein backbone. Initially, we want to fully characterize pure bilayer systems of DPPC and DMPC as these are the most predominant phospholipids in the plasma membrane of this bacterium. In addition, we are examining mixed bilayer systems of DPPC and DMPC. It is the hope of this author that future work in this area will encompass the incorporation of bacteriorhodopsin into the bilayer systems as well as the modeling of structure modifications which are introduced experimentally by Dr. Turner.

I. Experimental Studies of Langmuir Monolayers

It is well known that a variety of amphiphilic molecules form monolayers at the air-water interface. Using a Langmuir trough, as shown in Figure 4, one can compress the monolayer with a movable boundary at the air-water interface and monitor the pressure as a function of the boundary area. The trough normally contains an aqueous subphase, which often consists of water and a divalent ion. To this, a solution of an amphiphile in, for example, chloroform is applied to the surface of the subphase. The chloroform eventually evaporates leaving the amphiphilic molecule at the surface of the water. The boundaries, which are located at the air-water interface, can then be manipulated so as to compress the monolayer resulting in changes in its two-dimensional phase behavior. The phase diagram for a monolayer of a hypothetical amphiphilic molecule is shown in Figure 5, in which case surface pressure is plotted as a function of

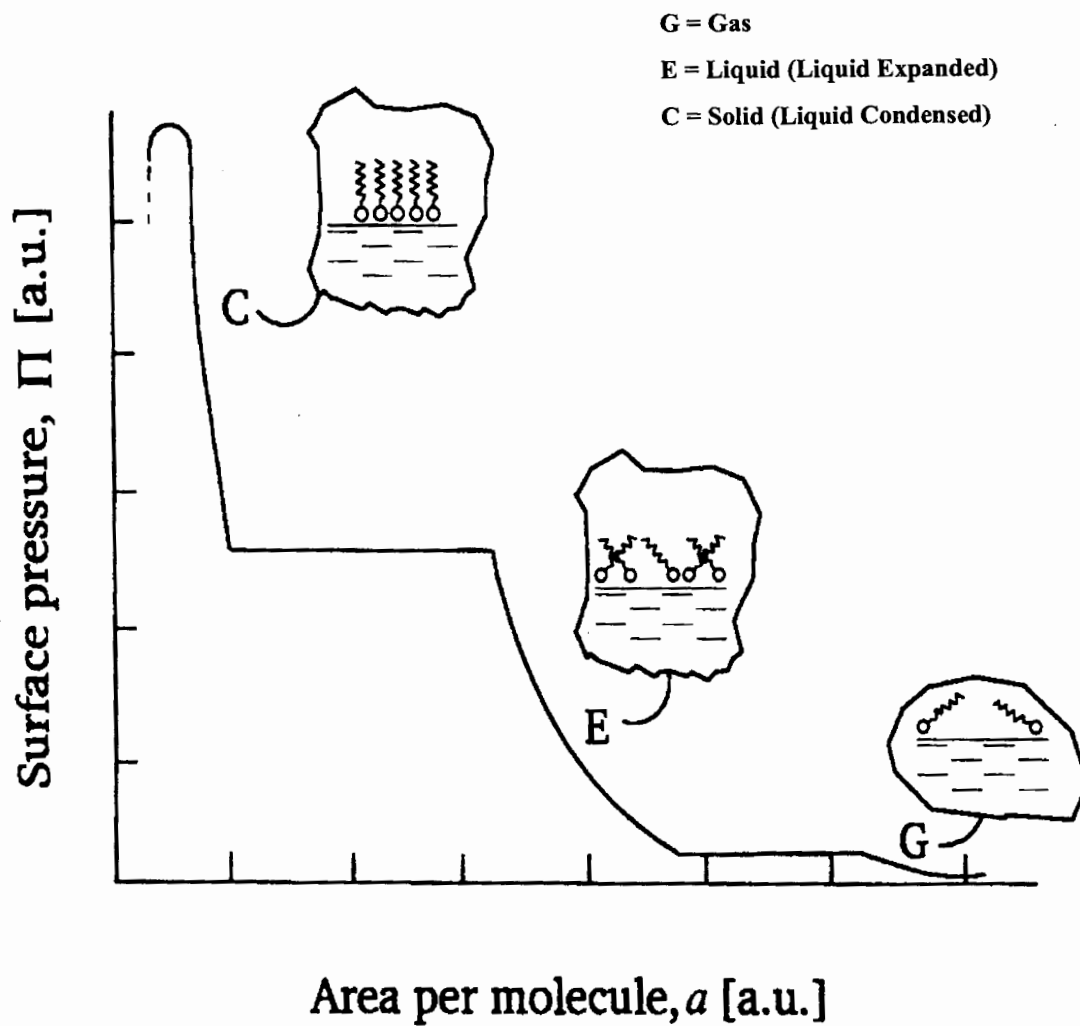


Figure 5. Isothermal phase diagram of a hypothetical long chain amphiphile. Reproduced from Ref. [24].

the area per molecule. As shown in the plot, three phases can be distinguished, namely, gas, liquid and solid. It is noteworthy that the liquid and solid phases are often referred to as the liquid expanded and liquid condensed phases, respectively. As shown in Figure 5, at high values of area per molecule the surface pressure is low and the monolayer exists in the gaseous state. However, as the monolayer is compressed and the area per molecule decreases, the film undergoes a transition to the liquid expanded phase and eventually to the liquid condensed phase. Monolayers, prepared in the trough and whose two-dimensional phase behavior is studied, are often referred to as Langmuir Monolayers.

In 1917, Irving Langmuir demonstrated that a monolayer could be transferred from the trough subphase to a suitable solid substrate.²² Langmuir's assistant, Katherine Blodgett, continued work in this area and contributed extensively to our current understanding of film deposition. Typically, silicon wafers, gold, silver, gallium arsenide, and freshly cleaved mica, to name a few examples, are used as substrates. If one were to choose a hydrophilic substrate, this would result in deposition of, for example, a fatty acid monolayer in which the headgroups would be bound to the substrate with the hydrocarbon tails oriented perpendicular to the surface. Films prepared in this way are known as Langmuir-Blodgett films.

Experimentally, there are a variety of techniques that can be utilized to study the structural properties of Langmuir-Blodgett films and Langmuir monolayers. More often, these experiments are performed on Langmuir-Blodgett films, since single or multilayers of the monolayers can be deposited onto a substrate and then be easily analyzed. The use

of multilayers results in thicker films, which can be analyzed with a wider variety of techniques. Analysis of a single monolayer is extremely difficult due to the limited thickness of the film; however, sophisticated techniques have evolved which permit researchers to monitor the behavior of Langmuir monolayers in a Langmuir trough as well as single layers deposited onto a substrate. Briefly, I would like to mention some of these techniques and their applications to either Langmuir monolayers or Langmuir-Blodgett films, however a more comprehensive review can be found elsewhere.²³⁻²⁶ In order to measure structural properties of a film, one can employ wave diffraction techniques such as X-ray diffraction, neutron diffraction, or electron diffraction. The X-ray and electron diffraction techniques can be utilized for a monolayer, while neutron diffraction typically requires multiple layers.²³ Characterization of the orientation of the molecules within the film can be accomplished using Fourier Transform Infrared Spectroscopy (FTIR), Raman Spectroscopy, or Fluorescence Spectrophotometry. FTIR has been used the most extensively to study monolayers and is principally utilized in the Attenuated Total Reflection or Grazing-Angle modes of operation. Ellipsometry is an extremely important surface technique that can measure the thickness of a film.²⁵

Although Langmuir monolayers have been studied in great detail since the early work of Langmuir and Harkins, the level of activity in this field has not subsided, presumably due to advances in instrumentation and many unanswered questions in regard to phase transitions.^{27,22} As stated previously, we are interested primarily in eicosanoic acid, which has been extensively reported on in the literature, due to its similarity in structure to 18-MEA. A number of examples can be found in the current literature where

various properties of eicosanoic acid monolayers have been studied as a function of packing density.^{14,15,21,17,16,18-20,13} Typically, these studies focus on various structural aspects of the film phases at various pH conditions and upon addition of foreign compounds into the film. We will refer to the results of these studies in order to provide a comparison between the experimental work completed for eicosanoic acid and our MD simulation studies of the same compound.

II. MD Simulations of Langmuir Monolayers

A considerable amount of simulation work has been conducted in the modeling of alkanethiol monolayers chemisorbed to various gold surfaces, known as self-assembled monolayers (SAMs).²⁸⁻³⁹ Unfortunately, considerably less research has been completed with regard to Langmuir monolayers⁴⁰⁻⁵² and LB films.⁵³⁻⁵⁹ This is surprising since an understanding of these systems could provide a fundamental understanding of chain interactions that would further lend to their use in practical applications. Molecular dynamics studies have been used to examine the conformational behavior of Langmuir monolayers and LB films of stearic acid,^{55,56} eicosanoic acid,^{52,57-59} pentadecanoic acid,⁴² pentacosadiynoic acid,⁵³ and (octadecylamino) dihydroxysalicylaldehyde.⁴⁴ Similarly, a molecular dynamics study of an arachidic acid monolayer (a Langmuir monolayer) was performed at various lateral pressures providing a simulated phase diagram of this compound's behavior.⁴⁸⁻⁵¹ These studies are particularly interesting due to a strange phase transition that appears in the isothermal phase diagram. In fact, a large portion of our work discusses the nature and occurrence of the reported phase transition. Moreover, MD studies based on coarse-grained models^{47,43} as well as Monte Carlo

simulations^{54,46,45,40,41} have been conducted for various Langmuir monolayer systems. In general, these studies use very similar force fields and calculate common parameters, which are discussed in Chapter II. A major limitation of the MD and Monte Carlo simulations that have been completed for Langmuir monolayers is the lack of a water substrate. In most of these studies a generic potential function was employed to model the interaction of water with the fatty acid molecules. This is a major difference between our work with Langmuir monolayers and that of previous authors, as we utilize actual water molecules for the subphase. Further, considering the limited amount of simulation research conducted in the area of Langmuir monolayers and LB films, much can be accomplished by borrowing knowledge obtained through studies on lipid bilayer and SAM systems.^{34,60}

III. Phospholipid Bilayers of DPPC and DMPC

The major constituents of biological membranes are phospholipids, which form a bilayer structure in which the tails of two monolayers face each other and the head groups are in contact with aqueous environments. Accordingly, there has been an extensive amount of research conducted in the area of model membranes for various phospholipids. Figure 6 provides an illustration of a phospholipid membrane where one can see the bilayer arrangement of the phospholipids as well as the incorporation of membrane proteins within this structure.⁶¹ Also present in the membrane are such molecules as carbohydrates, glycoproteins, glycolipids and cholesterol. Our work focuses on two important phospholipids, DPPC and DMPC, which only differ by two methylene groups in terms of length in the aliphatic portion of the phospholipid. The head groups, of

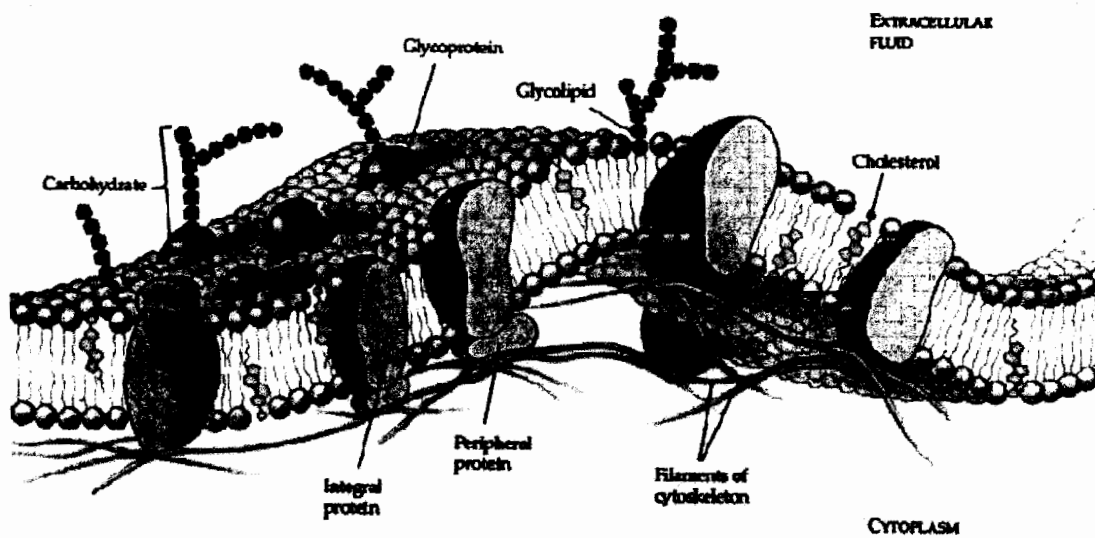


Figure 6. Illustration of biological lipid bilayer membrane. Reproduced from Ref. [61].

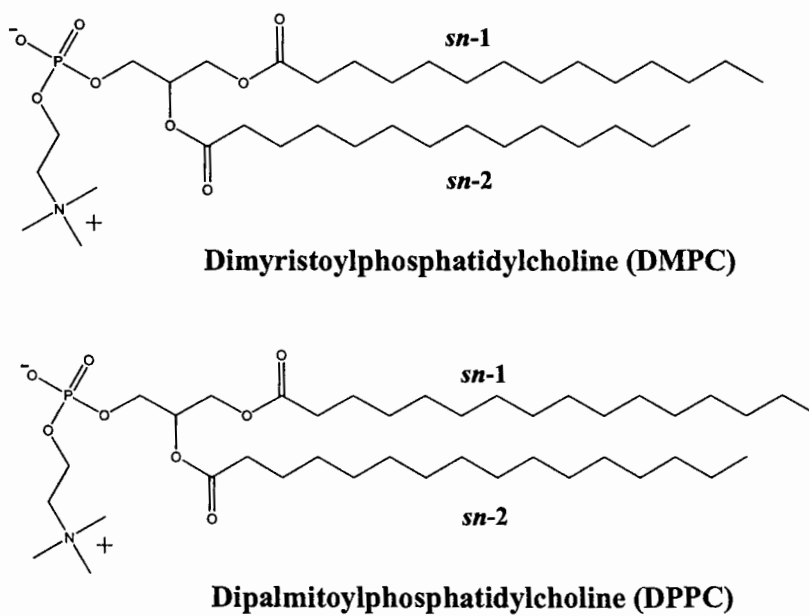


Figure 7. Structures of the phospholipids studied in this work.

course, are identical as shown in Figure 7. These phospholipids are the most abundant species in bilayer membranes, hence our motivation to study them. In addition, there have been many experimental studies of these systems providing a solid foundation for comparison to our computational results. As will be discussed in later chapters, we examined pure systems of each lipid as well as complex mixtures where the starting structure of the bilayer was manipulated in order to monitor diffusion and miscibility.

The most extensively studied bilayer systems are those of DPPC, as it has been established as the 'benchmark' phospholipid of bilayer studies.⁶⁰ Presumably, this is due to its natural abundance in bilayers, typically constituting a large percentage of the membrane lipids. Almost universally, studies of phospholipid bilayers are carried out in the liquid crystalline state (L_α), also referred to as the fluid phase, as this is the most biologically relevant state. For DPPC, most studies have been conducted at a temperature of 50 °C, which is well above the transition (41 °C) from the gel to fluid phase. In the L_α phase, the phospholipid molecules are disordered and experience translational diffusion as well as trans-gauche isomerizations.

There are a variety of methods to study bilayers, with the most important of these being the neutron and X-ray diffraction techniques as well as NMR studies. Typically, these techniques can provide information that can be compared to simulations which includes the three-dimensional structure of the bilayer, the order of the aliphatic chains, the packing density, electronic/atomic densities, electrostatic dipole potentials and the number of bound water molecules.⁶⁰ The reader is referred to several excellent accounts

that summarize experimental research conducted in the area of lipid membranes.⁶²⁻⁶⁵ A common approach to determining phospholipid bilayer structure and behavior is to perform deuterium NMR experiments in which the deuterium order parameter is measured. A description of this parameter is provided in Chapter II, however, it is worthy to briefly mention that the experiment is conducted in such a manner that the hydrogen atoms along the aliphatic tail of the phospholipid are selectively replaced by deuterium atoms. By measuring the quadrupolar interaction tensor of the C-D bonds, one can obtain information concerning the angle of these bonds relative to the bilayer normal leading to calculation of the deuterium order parameter. Thus, as will be discussed in subsequent chapters, comparisons can be made between experiments and simulations.

Experimental diffraction studies typically utilize multilamellar structures to investigate bilayer properties. Neutron and X-ray diffraction studies provide atomic resolution, however, the fluidity and disorder of lipid bilayers often presents challenges for the use of these techniques to study membrane structure. For example, when analyzing the crystal structure of phospholipids at low hydration, one can resolve the three dimensional coordinates of the system. However, when analyzing the L_{α} phase of bilayers, the diffraction techniques can only provide a one dimensional projection of the lipids onto a line normal to the plane of the membrane without any information about the other two dimensions (bilayer plane).⁶⁶ Thus, molecular dynamics simulations have evolved as an indispensable technique to provide a three-dimensional perspective of L_{α} phase membranes.

A thorough review of the experimental studies that have been conducted for DPPC and DMPC bilayers is beyond the scope of this text, however, we shall at least discuss some of the recent issues in the literature. Most importantly, there have been large discrepancies among experimental techniques in the determination of the interfacial area per lipid for DPPC membranes.⁶⁷ Values ranging from 56 Å² to 72 Å² have been reported, however, earlier commentaries suggests that 62 Å² is reasonable based on the merits of the studies that were conducted to obtain this value.^{68,69} Historically, experimental studies have been hampered by the difficulty in examining the L_α phase of membranes. This is not at all unusual when one takes into account the large degree of fluidity within the bilayer structure. Nevertheless, advances in experimental techniques and data analysis have led to a more accurate prediction of lipid bilayer three-dimensional structure.^{70,66,71-73}

IV. MD Simulations of DPPC and DMPC Bilayers

Much progress has been made in the last ten years in the molecular dynamic modeling of phospholipid bilayers, especially for DPPC, which has been the most extensively studied bilayer forming phospholipid. A large part of this success can be attributed to the immense advances that have been accomplished in the design of computer architecture. Throughout the nineteen nineties and into the early part of the twenty-first century we have witnessed desktop computer systems evolve from machines containing 33 MHz processors with 8 MB of random access memory (RAM) to systems with 2.5 GHz processors and 2 GB of RAM. As a notable example, in 1996 a simulation on the order of 1 ns for a DPPC bilayer⁷⁴ was considered to be a reasonable simulation

time, while only 8 years later simulation times up to 150 ns have been accomplished for similar systems.⁷⁵ In addition, many studies have led to the refinement of forcefields as well as an understanding of what parameters work best for a particular system. For example, it is now generally agreed upon that the treatment of electrostatic interactions in bilayer simulations is best handled with the particle-mesh ewald summation.⁷⁵⁻⁷⁷ The majority of membrane studies have been conducted for DPPC^{78-80,74,81-83,75-77,84-101}, however, other phospholipid membranes have been investigated as well and include DMPC^{102-110,95,111}, dioleoylphosphatidylcholine (DOPC)^{112-114,86} and palmitoyloleoylphosphatidylcholine (POPC)¹¹⁵ as well as various unsaturated and modified lipids.^{105,116,106,117-119} These studies have all contributed greatly to our current understanding of membrane dynamics on the molecular level. Large leaps in technology now allow us to investigate such complicated phenomena as the structure of membrane proteins within a phospholipid bilayer environment.¹²⁰

In most cases, MD studies of phospholipid membranes investigate the structure of the bilayer in terms of the order parameter, electron density plots, atom density plots, trans-gauche states of the aliphatic chains and interfacial area per molecule.

^{81,121,122,74,102,103,82,104,83,87} A great number of studies have focused on improvements in the forcefields and a thorough examination of the simulation parameters.^{84,123,76,77,75,85,124-126}

There have also been several contributions aiding the development of analysis techniques, with a specific emphasis on results from lipid bilayer simulations.^{80,78,79}

Numerous studies have investigated the effect of small molecules on bilayer structural properties, with cholesterol representing the molecule of most interest due to its unique

influence on the phase behavior of the bilayer.^{92,86,127,88-90,107,91,108} Despite its importance, fewer studies have investigated the structure of H₂O around the headgroup region of the phospholipids.^{110,109,128,93,94,129} It has been established that complex hydrogen bonding association occurs in lipid bilayers systems, resulting in lipid-lipid bridging via hydrogen bonds.^{109,110}

During the middle to late nineteen nineties, several discussions emerged in regard to the surface tension of lipid bilayer systems.^{130-132,99-101} By this time it was clear that constant volume simulations of bilayers systems less accurately described the real system being simulated. However, there were still arguments on whether to employ an applied surface tension to account for undulations in the bilayer or to apply a constant force with zero surface tension. Despite these efforts, the most recent studies of lipid bilayers utilize a pressure coupling scheme in which a constant pressure, typically 1 atm, is applied isotropically to the simulation box.^{76,77,75} This allows the x-, y- and z-box vectors to adjust accordingly in order to accommodate the proper pressure. Elegant work, which can be classified as special topics encountered in lipid bilayer simulations, has been completed mostly at the University of Groningen. These studies consisted of such topics as bilayer formation, analysis of bilayer undulations, measurement of the force to withdraw a lipid from the membrane and the simulation of NMR relaxation rates.^{97,96,133-135,98,111} In almost all simulation studies, comparisons are made with previous literature data obtained both by simulations and experimentally. If there is no experimental data available for comparison, one is left without any type of validation as to the credibility of his results. There are a few examples in the literature in which this topic is specifically

discussed.^{136,137,95,138} In general, several reviews on the subject of MD simulations of lipid bilayers have been reported in the literature.^{139,60,140,120,141-143} The most thorough of these, with respect to pure bilayer systems, is that by Tieleman *et al.*, however, it has been almost seven years since this report appeared in the literature.⁶⁰ A more recent overview was provided by Ash *et al.* albeit on the topic simulations of membrane proteins.¹²⁰

Chapter II

Computational Methods

*Anyone who lives within their means
suffers from a lack of imagination.*

Oscar Wilde

I. Introduction to the Molecular Dynamics Method

In a molecular dynamics simulation all atoms in the system under consideration are treated classically. Successive configurations of the system are generated by integrating Newton's laws of motion, resulting in a trajectory, which provides the positions and velocities of the particles as a function of time. In this section, we will briefly describe the general theory of molecular dynamics simulations with a particular emphasis on the aspects related to the MD forcefield and other algorithms which are employed in MD simulations. There are several texts which deal with this topic in great detail and the reader is referred to these publications for a more comprehensive overview.

144-147

Interactions between atoms consist of intramolecular (bonded) and intermolecular (non-bonded) interactions. Intramolecular interactions consist of bond stretching, bond angle, and dihedral interactions between covalently attached atoms. Intermolecular interactions, within a certain cut-off radius, occur between neighboring atoms and consist of van der Waals and electrostatic interactions. A typical potential function corresponding to the intramolecular interactions in a system is shown in Equation 1.

$$V_{intra} = \sum_{bonds} \frac{1}{2} k_{ij}^{bonds} (r_{ij} - r_{ij}^{equil})^2 + \sum_{angles} \frac{1}{2} k_{ijk}^{angles} (\theta_{ijk} - \theta_{ijk}^{equil})^2 + \sum_{dihedrals} k_{ijkl}^{dihedrals} (1 + \cos(a(\phi_{ijkl} - \phi_{ijkl}^{equil}))) \quad (1)$$

where k represents the force constants for the bonds, angles, and dihedrals, respectively, for each term in the equation. The bond lengths, bond angles, and dihedral angles are represented by r , θ , and ϕ , respectively. The equilibrium values for the bond length, angle, and dihedral angles are indicated with the superscript “*equil*”. In the dihedral term of Equation 1, a represents the dihedral multiplicity. The intermolecular potential energy, on the other hand, consists of a Lennard-Jones (LJ) potential (1st term in Equation 2) to describe the van der Waals interactions and a second term to describe the electrostatic interactions (2nd term in Equation 2) in the system.

$$V_{inter} = \sum_{i < j} 4\epsilon_{ij} \left[\left(\frac{\sigma_{ij}}{r_{ij}} \right)^{12} - \left(\frac{\sigma_{ij}}{r_{ij}} \right)^6 \right] + \sum_{i < j} \frac{q_i q_j}{4\pi\mu_0 r_{ij}} \quad (2)$$

where ϵ is the depth of the LJ potential well and σ the distance between two atoms when the LJ potential is zero. In the electrostatic portion of Equation 2, q is the charge of atoms i and j , μ_0 the dielectric constant of the medium, and r the distance between the charges. Nonbonded intramolecular interactions within the same molecule are treated using the V_{inter} potential described in Equation 2.

In summary, the total potential function includes: intramolecular interactions such as bond stretching, bond angle, and torsion; intermolecular interactions between the amphiphiles including van der Waals (LJ 12-6 potential) and electrostatic interactions. Energetically speaking, these interactions can best be described by the qualitative plots shown Figure 8. The intramolecular bond stretching and bond bending are described by

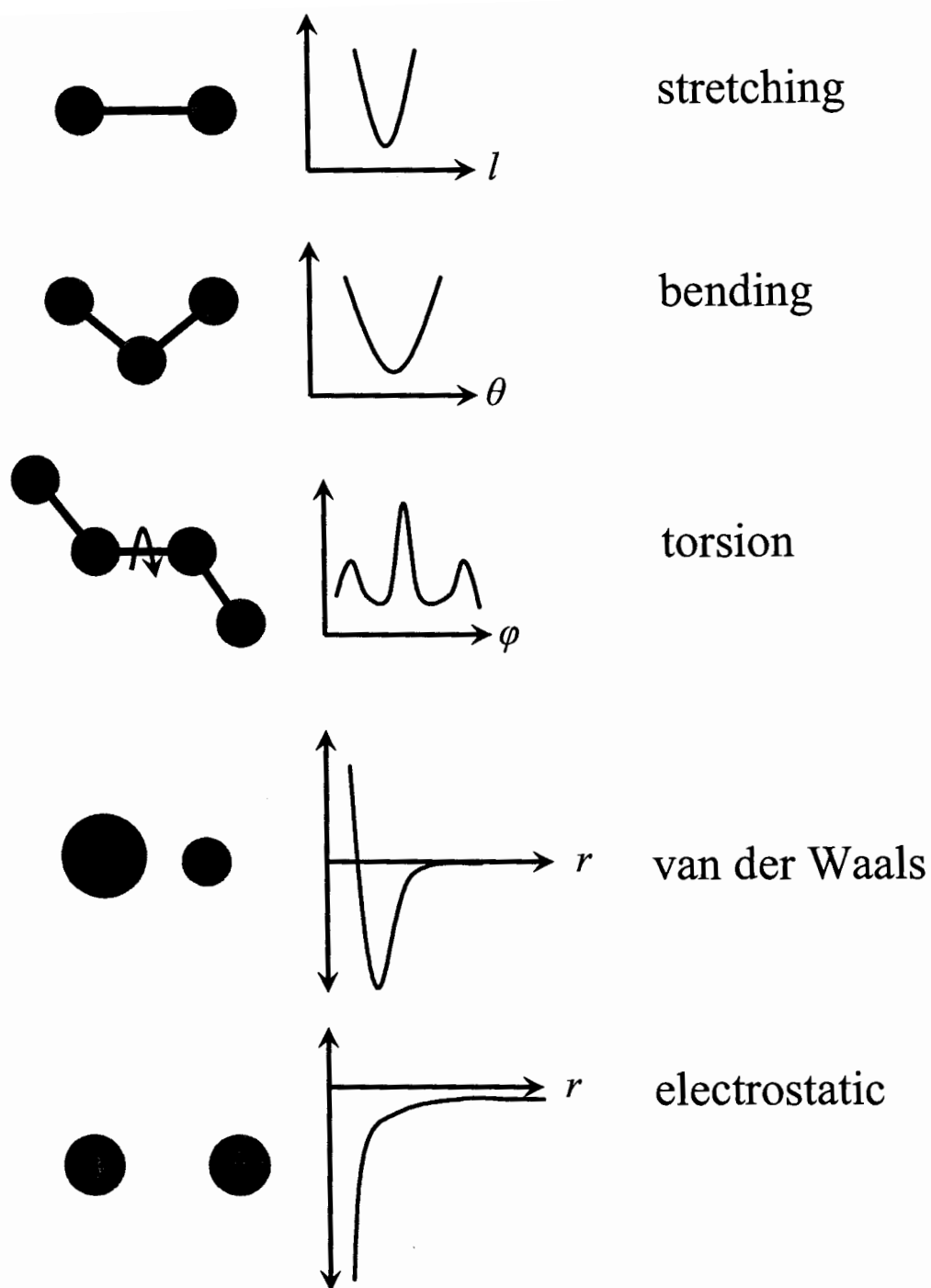


Figure 8. Inter- and intramolecular interactions described by molecular dynamics force fields.

derivations of Hooke's Law, which result in parabolic energy functions that depend on a bond force constant and bend force constant. The torsional interactions are described by the familiar cosine series expansion, shown in Equation 1, and graphically portrayed in Figure 8. Typically, rather large fluctuations in energy are required for a shift to occur from the equilibrium values of bond stretching and bending. However, much lower energies are required for torsional transformations to occur. These transitions are mostly responsible for the changes in conformational behavior we observe with molecular systems in which long alkyl chains play a predominant role.¹⁴⁷ Also shown in Figure 8 are the plots accounting for the intermolecular interactions. In our simulation work, the Lennard-Jones 6-12 potential is employed to account for the van der Waals interactions, however, depending on the needs of the researcher the Buckingham potential can be used as well.

$$V_{buck}(r_{ij}) = A \cdot e^{-\rho/r_{ij}} + \frac{C}{r_{ij}} \quad (3)$$

in which A , ρ and C are adjustable fitting parameters. For Coulombic interactions the classic equation for electrostatic interactions is employed. In the plot, we show a curve corresponding to the attraction between a positive and negative charge, however, this function takes into account positive-positive and negative-negative interactions also.

At the start of a simulation, the initial geometry of the system is used to compute a force on each atomic and molecular species in the system according to the potentials described in equations 1-3. The computed forces are then used to determine the instantaneous velocity of each atom and molecule. Over a set length of time, the atoms are moved to a new position according to Newton's equations of motion given the force

and velocity on each. The new positions at the end of the timestep are then used to calculate new velocities and forces which determine the motion of the atoms in the next step. This process is repeated until the forces on each atom in the system have decayed (converged) to some user-selected minimal value. Once the forces have been minimized, the system is said to be equilibrated. All positions, velocities and forces resulting from further timesteps represent fluctuations in the equilibrated system as the system samples equi-energetic states. A listing of the positions, velocities, and forces on all atoms in the system for each time step is called a fluctuation trajectory. From the fluctuation data, ensemble average properties can be calculated using standard time average sampling techniques viz.:

$$\langle A \rangle = \frac{1}{M} \sum_i^M A(t_i) \quad (4)$$

where M is the number of samples (timesteps).

II. Temperature and Pressure Coupling in MD Simulations

Aside from the forcefield parameters, discussed above, there are many other aspects to consider when performing an MD simulation. There are special algorithms that need to be employed, for example, to control either the temperature or the pressure of the system. Molecular dynamics simulations have evolved over the years and are now capable of sampling from all of the statistical thermodynamic ensembles. The Microcanonical ensemble (NVE) can be considered the typical MD ensemble, where the number of particles, the volume, and the energy of the system are all conserved.¹⁴⁸ The use of other thermodynamic ensembles requires that system variables be controlled utilizing special algorithms. For example when sampling from the Canonical (NVT) or

the Isothermal-Isobaric (*NPT*) ensembles, the temperature and pressure must be controlled. For control of temperature, the two most well known methods are Berendsen¹⁴⁹ and Nosé-Hoover^{150,151} temperature coupling. In general to control temperature in a simulation, the velocities of all of the particles must be scaled. Such manipulations, however, would cause the system to behave in a non-Newtonian manner.¹⁴⁸ Therefore, the necessity arises for an algorithm, such as that provided by the Berendsen technique, which decreases the speed of the scaling by coupling to an external temperature bath. The Nosé-Hoover temperature scaling procedure, on the other hand, functions by adding a thermal reservoir and friction term to the equations of motion.¹⁵² The Berendsen temperature coupling scheme is a very efficient algorithm for reaching a particular temperature, however, if a proper canonical ensemble is required, the Nosé-Hoover scheme should be employed.¹⁵² For pressure coupling, the box vectors and atom coordinates are scaled at each time step. In GROMACS, one can employ the Berendsen or Parinello-Rahman pressure coupling schemes. The Berendsen pressure coupling algorithm operates on the same principal as the Berendsen temperature coupling. Unlike the Berendsen scheme, the Parinello-Rahman pressure coupling algorithm maintains an ensemble system and operates in a similar manner as the Nosé-Hoover temperature coupling algorithm.^{153,154} In the case of pressure and temperature coupling, we utilized the Berendsen coupling method.

We utilized the canonical (*NVT*) ensemble for our studies of fatty acid monolayers as it is necessary to maintain constant volume, especially along the x- and y-axes, in order to replicate the constant boundary conditions in a Langmuir trough experiment. In

our studies of lipid bilayers we employed the Isothermal-Isobaric (*NPT*) ensemble, which allows the box vectors to adjust as necessary to accommodate a specified constant pressure value, thus permitting us to monitor the packing density of the bilayer.

III. Periodic Boundary Conditions

In order to eliminate any edge-effects in a molecular dynamics system, periodic boundary conditions (PBC) must be employed. If we were to simulate an MD system without PBC, artifacts would appear at the edges of the simulation box where the molecules at the edges of the box would be in contact with rest of the system on the interior and with nothing at the periphery. Typically, very small systems are simulated in molecular dynamics, on the order of tens to hundreds of molecules. Therefore, one can not afford to sacrifice part of the system of molecules due to the edge effects. Figure 9 provides an illustration of periodic boundary conditions in which replicas of the primary simulation box are generated, first in two-dimensions and then in three-dimensions. As seen in the two-dimensional case, replicas of the original system are created on each of its sides. This allows, for example, the black particle in the central simulation box to interact with the grey particles in several of the periodic images. In actuality, PBC can be applied in three-dimensions as shown in the second part of Figure 9.

IV. Treatment of Long-Range Interactions

The treatment of long-range non-bonded interactions, which is deemed important enough to constitute its own section in this text, represents yet another facet of the MD simulation. The treatment of electrostatic and van der Waals interactions during a

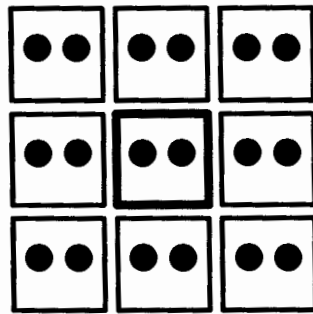


Illustration of Periodic Boundary Conditions in 2D
(Central Box is Primary Simulation Cell)



Illustration of Periodic Boundary Conditions in 3D
(Central Box is Primary Simulation Cell)

Figure 9. The use of periodic boundary conditions in MD simulations. Adapted from Ref. [147].

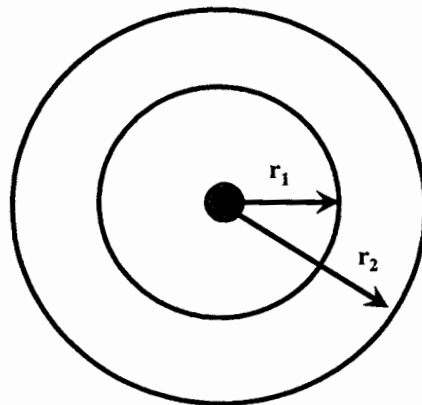
molecular dynamics simulations has become an increasingly controversial subject, especially in the case of lipid bilayer membrane systems.⁷⁵⁻⁷⁷ It is particularly troublesome with regard to electrostatic interactions. Since electrostatic pair interactions decay as a function of $1/r$, they have considerably longer range than the van der Waals interactions which decay as $1/r^6$. Traditionally, the cut-offs method has been employed for both van der Waals and coulombic interactions. Cut-offs function by terminating any interactions beyond a specified radius (r), however this radius cannot exceed one half the length of the simulation box. While this method is suitable for the less long-range van der Waals interaction (r^{-12} and r^{-6}), it has been found not to be ideal for electrostatic interactions (r^{-1}). For example if a cut-off of 1 nm is employed in a simulation, then the interactions of any atoms beyond this radius with the reference particle would be ignored. Therefore, an abrupt change is experienced at the cut-off where the forces are truncated. One way to deal with this situation would be to increase the cut-off, to e.g. 2 nm, which would require an increase in the simulation box size to at least 4 nm in any dimension. In the case of our monolayer systems, we are dealing with monolayers that contain a grid of 8 x 8 fatty acids, with box lengths on the order of 3 to 4 nm. Thus, we typically can not use cut-offs greater than 1.5 nm as this would be half the length of the simulation box in the x- or y- directions. Therefore, in order to use larger cut-offs it is necessary to increase the size of the system. Increasing the system size in MD simulations is usually impractical as it greatly increases the computational cost.

Another alternative for dealing with long-range electrostatic interactions is to employ the Ewald summation technique.¹⁵⁵ This method effectively deals with the

interaction of a particle with all other particles in the periodic images of the primary simulation box. Briefly, the Ewald method involves treating the slowly converging real-space charge distribution as a sum of two reciprocal space distribution which converges much more rapidly. A mathematical enhancement to this technique, which we employ in our studies, is the Particle-mesh Ewald Summation.^{156,157} For a graphical comparison of the cut-off and PME methods the reader is referred to Figure 10. Other techniques include the reaction field method or the use of a shift or switch function. Like the other techniques, a cut-off is utilized with the reaction field method in which all interactions within the cut-off are treated as before. However, any space beyond the cut-off is treated as a homogenous medium with a given dielectric constant.¹⁴⁷ The purpose of the shift and switch function is to eliminate the sharp truncation of forces at the cut-off by providing a smooth transition in which the energy becomes asymptotic to a minimum value. Both functions ultimately achieve the same outcome, however the shift function multiplies the potential with a function while the switch function adds a function to the potential.¹⁵²

V. Time Scale of Events in Chemical and Biological Processes

When performing MD simulations it is essential to have an understanding of the time scales one is dealing with in terms of chemical and biological processes. MD simulations are conducted in such a way that the interactions of the particles that constitute our system are monitored in the time domain, thus providing the position and velocities of all atoms as a function of time. Chemical transitions occur at much more rapid pace than biological processes. In general, these include bond vibrations (10^{-14} s),



Cut-Off Method - At r_2 the electrostatic interactions are abruptly cut off.

The Particle-mesh Ewald Sum - Cut-offs are applied up to r_1 , then from r_1 to r_2 the PME Summation is applied.

Figure 10. Treatment of long-range electrostatic interactions in MD simulations.

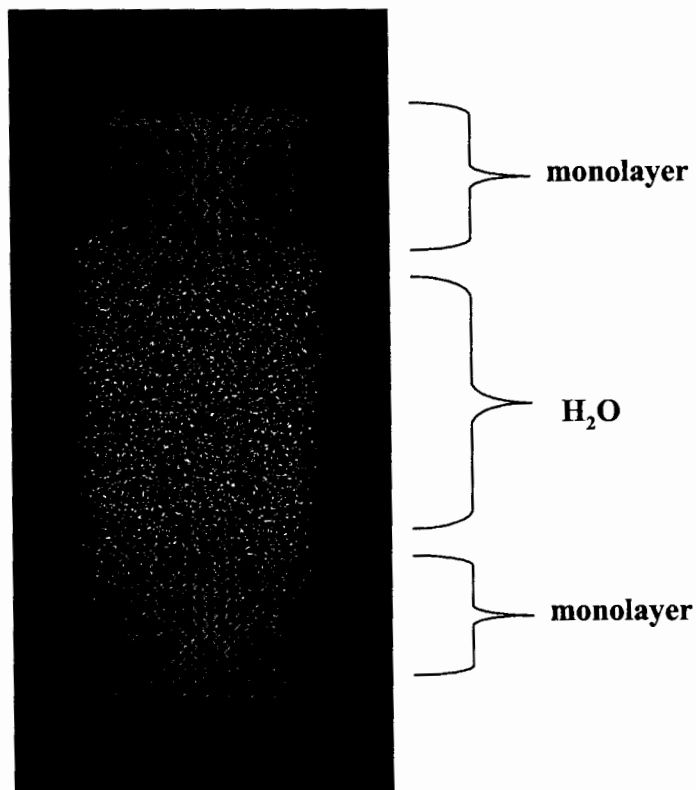


Figure 11. Starting structure of a dual monolayer system of 18-MEA.

angle vibrations (10^{-12} s) and trans/gauche isomerizations (10^{-11} s - 10^{-10} s). Therefore, the time-step in our simulation must be of a magnitude that it is less than that of the fastest process, which is the bond vibration. For this reason, a time-step of 1 to 2 fs (10^{-15} s) is typically employed in MD simulations. The size of our time-step will then be the limiting factor as to what type of biological processes we can simulate, since the longer a process is the more steps that are required to perform the simulation. Some examples for biological processes include lipid bilayer formation (10^{-8} s - 10^{-7} s), the R to T conformational transition in Hemoglobin (10^{-6} s), and protein folding (10^{-6} s - min). Therefore, such processes as protein folding are as of yet still not feasible for MD simulations due to their long duration and given the limited resources at our disposal in terms of computational power. More specific to processes that occur in lipid bilayer systems, there are trans/gauche isomerizations (10^{-11} s - 10^{-10} s), flexing of the hydrocarbon chain (10^{-9} s), rotation about the molecular axis ($3 \cdot 10^{-9}$ s), lateral movement within the bilayer (10^{-7} s), flip-flop across bilayers (10^5 s), and undulatory motions.

VI. Molecular Dynamics Simulations

The MD simulations were completed using the software package GROMACS (Groningen University),^{158,159} operating on a Microway Cluster Server with 16 nodes containing 1.4 GHz Athlon processors on each node, which utilized the Linux 8.0 operating system. The GROMACS suite of programs is a very versatile package whose primary design is for the examination of biomacromolecules, however, this software has been used extensively to model lipid membranes. Briefly, we would like to review a few

of the steps involved in a typical molecular dynamics simulation. First, a molecular structure and topology file for the system of interest must be constructed. A detailed description for the construction of molecular structure file is provided in Section I of the Appendix. The topology file, which must be in ASCII format, contains information about how and what atoms in a molecule will interact with each other. This includes information with regard to bond length, bond angle, dihedral angles, charge interactions, and non-bonded pair interactions. In most cases we constructed the topology files ourselves, however, other times we utilized a web-based program entitled "The Dundee PRODRG2 Server" which generates various types of topology files.¹⁶⁰ This allowed us to compare the files we constructed to those produced by the server. For the lipid bilayer simulations we used topology files for DPPC and DMPC that were obtained from Peter Tieleman's website.¹⁶¹ Example topology files for eicosanoic acid and DPPC are given in Sections III and IV of the Appendix.

Once the pdb and topology files have been constructed, they can then be used for input with the GROMACS software. In addition to the file types described above, one must also construct an input file for both an energy minimization step and the actual molecular dynamics simulation. These file types contain all of the information about the simulation settings and parameters. For instance, the total length of the run, the length of each step, details of the electrostatic/van der Waals interactions, temperature coupling, and pressure coupling are just a few examples of the parameters that are defined in energy minimization and molecular dynamics parameter files. Sections V and VI of the Appendix provide examples for both of these file types. Once the file types described

above are constructed, there are series of steps that must be completed before a molecular dynamics simulation can be performed. These consist of placing the structure in a periodic box, solvating the system, and performing an energy minimization. Then, the desired molecular dynamics run can be executed. Figure 12 provides an outline of the series of steps typically followed when performing a molecular dynamics simulation with GROMACS. Again, examples of each file type are provided in the Appendix of this text.

Thus far we have outlined and discussed many of the essential parameters for a MD simulation. In addition to this, we need only to mention the rationale for the logistics of the series of simulations that are typically conducted for a system under study. When conducting MD studies it is common to perform, what is termed, an Equilibration Simulation followed by the Production Simulation. The Equilibration Simulation allows the system to reach equilibrium before one begins to determine various quantities he is interested in calculating. After this, a separate Production Simulation can be conducted at which time all of the parameters and quantities of interest can be determined. In our case the Equilibrium Simulation consists of a series of simulations which are conducted in a step-by-step procedure to ensure energy conservation of the system. In all our studies, we first simulated the system with position restraints in which case the movements of all atoms that constitute system were constrained by a harmonic potential. This removes strain from the molecules and only permits small motions during the simulation. In a subsequent simulation, the lipids are allowed to move freely (as they normally would in a simulation) and the H₂O molecules are subjected to the same restrain potential as previously. This allows the alkyl chains of the lipids to interact while

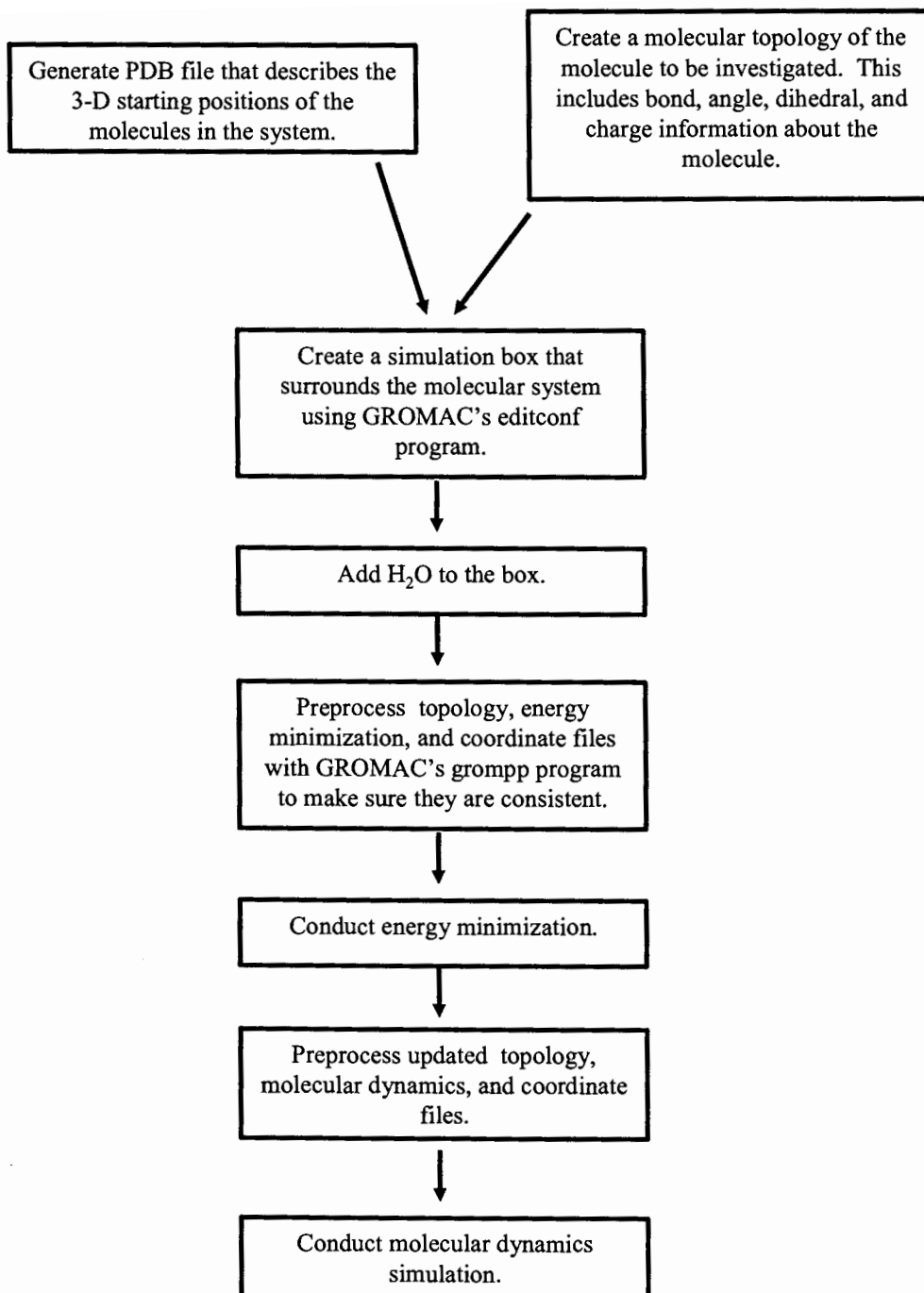


Figure 12. Typical series of steps followed in a molecular dynamics simulation using GROMACS. Adapted from Ref. [159].

preventing any H₂O from entering the aliphatic portion of the monolayer or bilayer and in the case of the monolayer simulations it prevents H₂O from entering the vacuum space.

More specific details for each simulation set is provided below.

Monolayer Simulations

The majority of the monolayer studies examined systems containing two 8 x 8 monolayers for a total of 128 fatty acids or two 16 x 16 monolayers resulting in 512 fatty acids. As an example, the starting structure for an 8 x 8 monolayer of eicosanoic acid is shown in Figure 11, in which a dual monolayer system was constructed consisting of an approximately 4 nm slab of H₂O in between.¹⁶² We take this approach in order to institute two-dimensional PBC and also to prevent the water from migrating to any vacuum areas of the simulation box. The total number of water molecules ranged from 1800 - 1850 molecules for 8 x 8 and 7750 - 7800 for the 16 x 16 systems. The number of water molecules in any given simulation system is chosen so as to maintain a consistent water density as the physical size of the simulation box is varied. The starting packing density was important for the monolayer systems as we employed the NVT ensemble in the MD simulations. Initially, the monolayer system was constructed in a hexagonal lattice arrangement at a packing density of 18.5 Å²/molecule. In increments of 0.5 Å²/molecule, the packing density of the monolayer system was increased up to 25 Å²/molecule and measurements were obtained at every point. We also conducted an experiment where the packing density was reduced in increments of 0.5 Å²/molecule from 25 Å²/molecule to 18.5 Å²/molecule.

The GROMOS 96 forcefield (ffG43a2) with modified united-atoms was employed for the bulk of the simulations. However, we also performed simulations using other forcefields that were compatible with GROMACS. The GROMACS forcefield (gmx) was employed using two different types of united-atom models to represent the methyl and methylene groups, one set in which the dihedrals are based on the GROMOS periodic function¹⁵² and the other optimized with the Ryckaert-Belleman potential.¹⁶³ In addition, we also utilized a forcefield¹⁶¹ that utilizes united-atom potentials that were optimized for pentadecane.⁸¹

The choice of the GROMOS 96 modified forcefield for most of the studies stems from its optimization of the united-atoms for phospholipid bilayer systems. The united atom model treats the methylene groups as single species thus reducing the total number of atomic species in the simulation and the computational cost. The single-point-charge (SPC) model was used to model water.¹⁶⁴ Prior to the actual MD simulations, energy minimizations were conducted using the Steepest Descent method.^{144,147} After energy minimization, a position-restrained MD simulation was conducted for all atoms in the system. This was followed by a subsequent position-restrained simulation in which all of the SPC water molecules were restrained; however, the fatty acids were not subject to restraints. Next, the system was subjected to a series of steps that permitted study of the monolayer system at various packing densities. As stated previously, the initial structure of the monolayer imposed a packing density of $18.5 \text{ \AA}^2/\text{molecule}$ on the system. In increments of $0.5 \text{ \AA}^2/\text{molecule}$, the packing density of the monolayer system was increased up to $25 \text{ \AA}^2/\text{molecule}$ by modifying the simulation box vectors; and

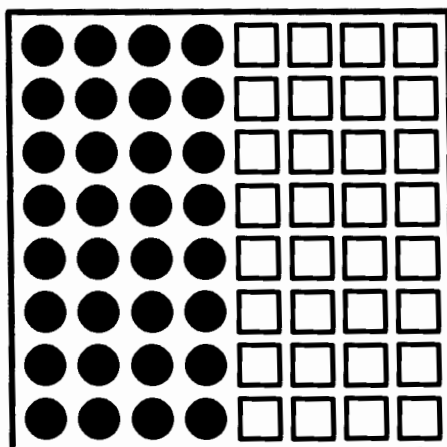
measurements were obtained at every position.⁵¹ In order to accomplish this procedure, equilibration simulations were conducted for 400 ps at each packing density followed by 1000 ps production runs. All measurements were performed by analysis of the 1000 ps simulations. We have carried out the same simulations for longer periods of time (5000 ps) and all of the measured parameters remain constant. Thus, the 400 ps equilibration and 1000 ps analysis period are sufficient quantities of time for the systems under study. A timestep of 1 fs was employed for all simulations. The temperature was maintained at 298 K using the Berendsen Temperature Coupling Bath scheme with a time constant of 0.1 ps.¹⁴⁹ Bond lengths were constrained using the SHAKE algorithm¹⁶⁵ for the fatty acids and the SETTLE algorithm¹⁶⁶ for SPC water. Typically, the cut-off method was utilized for the Lennard-Jones interactions at a distance of 0.9 nm, while long-range electrostatic interactions were treated using the Particle-Mesh Ewald algorithm.¹⁵⁶ However, we have also examined the effect of modifying the various long-range interactions parameters. This included using cut-offs for the both the van der Waals and the electrostatic interactions as well as adjusting the distance of these cut-offs. The reaction-field and shift functions were also examined, however, as stated above most of the simulations utilized normal cut-offs (0.9 nm) for LJ interactions and PME for Coulombic interactions. We also examined the effect of system size on the simulation in which 64 and 256 fatty acid monolayer systems were employed.

Phospholipid Bilayer Simulations

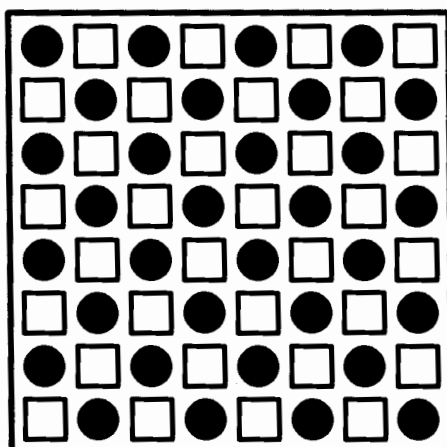
In contrast to the NVT simulations, which were conducted for the monolayers, the bilayer simulations were carried out using the NPT ensemble thereby allowing the box

vectors to adjust accordingly in order to accommodate a constant pressure, typically 1 atm. The starting structure of the phospholipid systems were constructed as 8 x 8 monolayer systems with H₂O placed above and below the bilayer. We examined pure bilayer systems of DPPC and DMPC as well as mixtures of these phospholipids. As shown in Figure 13, the mixed systems of the two phospholipids were constructed in a block arrangement, in which each half of the simulation box contained one species of phospholipid, or an alternating scheme in which the phospholipids are dispersed among each other in a repeating fashion. The amount H₂O in the systems ranged from 2900 - 3300 molecules.

For the initial series of MD runs, we utilized a similar procedure to that employed for the monolayer system. After the energy minimization, the first MD simulation (400 ps) was conducted in which all atoms in the system were position-restrained in the NVT ensemble. This was followed by a subsequent simulation (400 ps) in which only the H₂O molecules were position-restrained and the lipids were allowed to move freely about. Next, all position-restraints were removed from the system and both the lipids and H₂O were allowed to freely interact, still employing the NVT ensemble. After these equilibrations had been achieved, the series of NPT simulations were carried out, initially in 4 ns increments but later in units of 10 ns until a total simulation time of 50 ns in the NPT ensemble was achieved. In this case, we can define the production run from 10 ns to 50 ns. Thus, any averaged values, such as the deuterium order parameter or interfacial area per molecule, that are reported in this text will be taken from this period of the simulation.



Block Formation



Alternating Formation

● Dimyristoylphosphatidylcholine (DMPC)

□ Dipalmitoylphosphatidylcholine (DPPC)

Figure 13. Starting arrangements for mixed bilayer systems of DMPC and DPPC

Similar parameter settings were employed as in the monolayer studies, however, accommodations to these were required to conduct the simulations in the NPT ensemble. We employed a forcefield¹⁶¹ that utilizes united-atom potentials that were optimized for pentadecane.⁸¹ This is the forcefield available from Peter Tieleman, which is specifically parameterized for lipid bilayer studies, and recently has gained recognition by its use in several important studies of DPPC.⁷⁵⁻⁷⁷ A timestep of 2 fs was employed for all simulations. The temperature was maintained at 298 K using the Berendsen Temperature Coupling Bath with a time constant of 0.1 ps.¹⁴⁹ Likewise, the pressure was kept constant at 1 atm using the Berendsen Pressure Coupling Bath with a time constant of 2 ps.¹⁴⁹ Bond lengths were constrained using the SHAKE algorithm¹⁶⁵ for the phospholipids and the SETTLE algorithm¹⁶⁶ for SPC water. In all cases the cut-off method was utilized for the Lennard-Jones interactions at a distance of 0.9 nm, while long-range electrostatic interactions were treated using the Particle-Mesh Ewald algorithm.¹⁵⁶

VII. Analysis of Molecular Dynamics Data

Potential & Kinetic Energy

As described above, the potential energy is the underlying factor of a MD simulation. Therefore, the various contributions of potential energy from bonded and nonbonded interactions are determined at each time step of the simulation. Thus, Equations 1 and 2 are responsible for determining the contributions of each potential energy term to the overall scheme. In accordance with classical mechanics, the kinetic energy is calculated from the mass (m) and velocity (v) of each particle.

$$E_{kin} = \frac{1}{2} \sum_{i=1}^N m_i v_i^2 \quad (5)$$

Further, the absolute temperature of the system is related to the kinetic energy by the following relation:

$$E_{kin} = \frac{1}{2} k_B T (3N - N_C) \quad (6)$$

in which case k_B represents Boltzmann's constant ($1.38 \cdot 10^{-23}$ J/K) and T corresponds to the temperature. In Equation 6 it is assumed that each particle, N , has three degrees of freedom and any constraints on the system are accounted for by N_C .

Pressure & Surface Tension

Surface tension represents one of the parameters we were most interested in this work. In MD simulations, surface tension is derived from pressure tensors. First, we shall explore the concept of pressure from a MD perspective which is defined as a 3 x 3 matrix of the various tensor components:

$$\mathbf{P} = \begin{pmatrix} P_{xx} & P_{xy} & P_{xz} \\ P_{yx} & P_{yy} & P_{yz} \\ P_{zx} & P_{zy} & P_{zz} \end{pmatrix} \quad (7)$$

Each tensor component represents the pressure (force per unit area) that acts on the surface where the first index of each component refers to the normal axis of the plane on which the force acts and the second index to the direction of the force. In our simulation studies, we are only interested in the diagonal elements (P_{xx} , P_{yy} , and P_{zz}) as our simulation box is not deformed by shear during the simulation. Thus, the values of the off-diagonal elements are typically on the order of zero.

The surface tension for a system in which the interface is perpendicular to z axis, such as the case in our simulations of monolayers and bilayers, may be calculated using the relationship developed by Hill¹⁶⁷:

$$\gamma = - \int (P'(z) - P) dz \quad (8)$$

Where $P'(z)$ and P are the lateral and bulk pressure, respectively. Further, using the diagonal elements of the matrix in Equation 7, we can calculate the surface tension of our system with the following:¹⁶²

$$\gamma = -\frac{1}{2} \left(\frac{P_x + P_y}{2} - P_z \right) L_z \quad (9)$$

where L_z is the length of the simulation box in the z-direction. During the study of Langmuir monolayers, one is typically interested in the surface pressure of the monolayer film which is defined as the difference between surface tension of the subphase (γ_o) and that of the subphase with the film (γ):

$$\pi = \gamma_o - \gamma \quad (10)$$

Film Thickness

During characterization of the various system properties for both monolayers and lipid bilayers it is of interest to determine the thickness of the amphiphilic structure. Since the equilibrated films have a finite degree of surface roughness, an exact determination of the film thickness is not generally meaningful. However, one can determine the atomic density of the film as a function of z-axis dimension which undergoes a sharp decay at the film upper boundary. This is accomplished using a program within the GROMACS software package named **g_density**. It measures the

density for a group of molecules along a specified axis permitting the determination of film thickness. For example, Figure 14 provides a plot of density along the z-axis of the simulation box for two eicosanoic acid monolayers separated by a layer of H₂O. The reader is instructed to take note of the curve for water (dashed lines), which is situated in the center of the simulation box and hence in the center of the density plot. Eicosanoic acid, on the other hand, is represented by the solid line in Figure 14. For each monolayer of eicosanoic acid there is one point on the curve that is much higher in intensity than the remainder, which corresponds to the headgroup region of each fatty acid monolayer. In both cases, the tails are represented by the plateau adjacent to the high intensity peak. In order to determine the thickness of the monolayer, the distance between the highest point on the curve (corresponding to the headgroup) and the end of the tails (the end of the plateau region) is measured.

Monolayer Tilt

Typically, we only measure the tilt angle for the monolayer films as there is little collective tilt in the lipid bilayer systems. As an illustration, Figure 15 defines the tilt angle (θ) pictorially. Using Equation 11, we measure the tilt angle utilizing monolayer thickness values obtained from density plots, which were discussed in the preceding section.

$$\cos(\theta) = \frac{l}{l_o} \quad (11)$$

Where l_o is the thickness of a monolayer at 18.5 Å² and l the thickness at a given packing density.⁴⁸

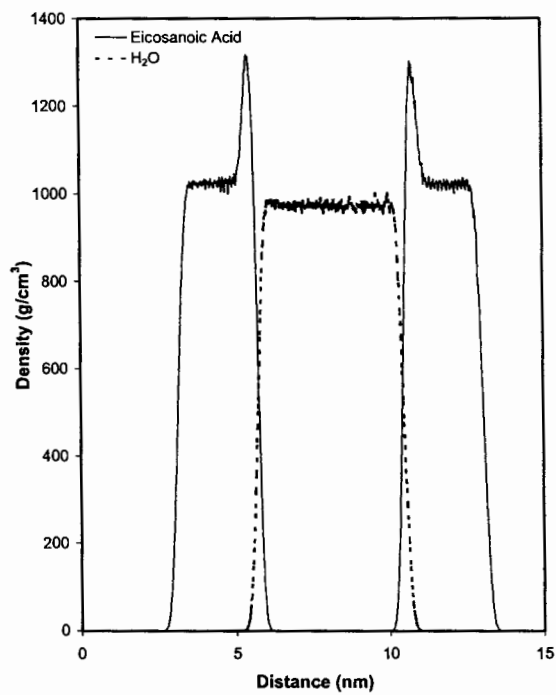


Figure 14. Plot of density as a function of distance along the z-axis of the simulation box for eicosanoic acid and H₂O.

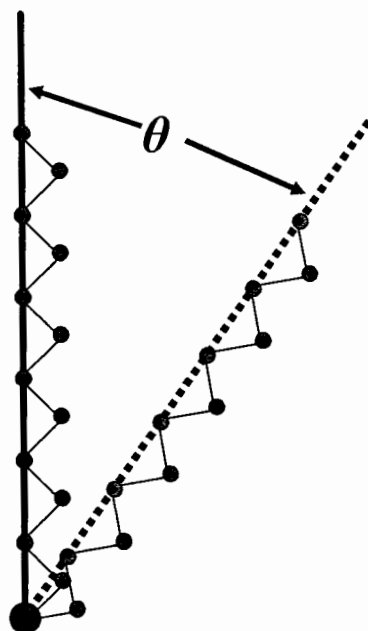


Figure 15. Graphical representation of tilt angle for molecules containing long alkyl chains.

Radial Distribution Function

When analyzing MD simulation data, one of the most common methods to describe the structure of molecules that constitute the system is the Radial Distribution Function (RDF) $g(r)$ (also referred to as the Pair Distribution Function or Pair Correlation Function). This parameter can also be determined experimentally from X-ray or neutron diffraction. The RDF provides the probability of finding an atom B within a particular distance range ($r \rightarrow \Delta r$) from another atom A.

$$P\{i, j, r, \Delta r\} = \frac{4\pi r^2}{V} g_{ij}(r) \cdot \Delta r \quad (12)$$

More specifically, one can determine the number of atoms that can be found at a distance $r + dr$ from the reference atom. Graphically, this can be envisioned as illustrated in Figure 16 in which case the black-filled reference atom is at the center of the ring. Of the remaining atoms the gray-filled circles represent atoms that fall within the range $r + dr$ and the hollow circles correspond to all other atoms in the system. Mathematically, the radial distribution function is defined as¹⁶⁸:

$$g(\mathbf{r}) = \frac{1}{\rho} \frac{1}{N} \left\langle \sum_i^N \sum_{j \neq i}^N \delta[\mathbf{r} - \mathbf{r}_{ij}] \right\rangle \quad (13)$$

In which case N is the total number of atoms, ρ the number density (N/V), and \mathbf{r}_{ij} the vector between atoms i and j . The reader shall take note of the use of the δ -symbol which is a special notation that used with spatial distribution functions. For example, the δ -symbol can take values of¹⁶⁸:

$$\delta(x - x_i) = \begin{cases} \infty \\ 0 \end{cases} \quad (14)$$

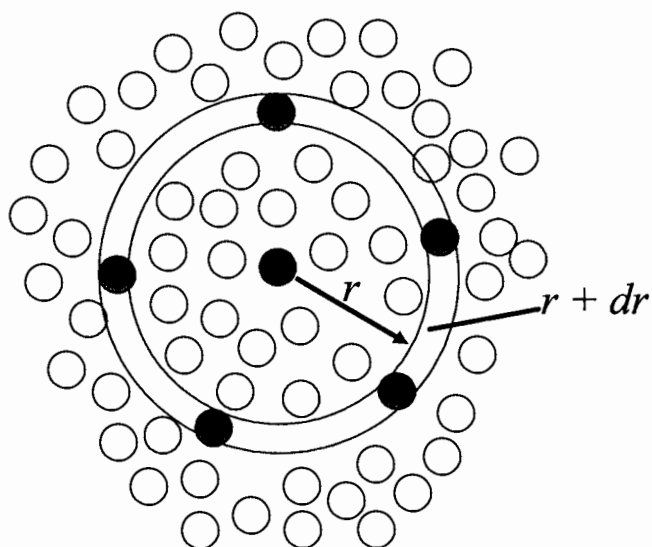


Figure 16. Graphical representation of the radial distribution function. Black circle = reference atom, grey circles = atoms that fall within selected radius, clear circles = all other atoms.

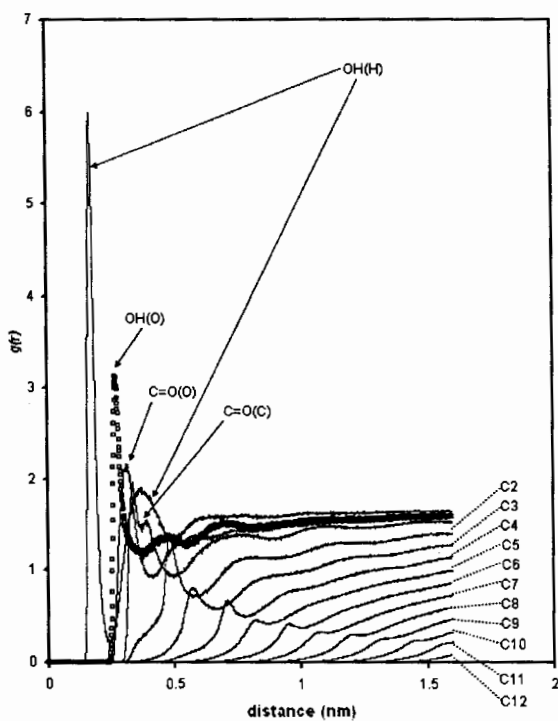


Figure 17. Radial distribution function between various atoms along the backbone of eicosanoic acid and the H₂O oxygen.

where ∞ is the case when the center of atom i is located at x while values of 0 are obtained if the center of atom i is not at x . As a practical example, we have included Figure 17 which provides the radial distribution function for various atoms along the backbone of an eicosanoic acid molecule and the oxygen atom of water in the case of a monolayer system. From the Figure, it is evident that H_2O forms the most intimate structure with the hydroxyl hydrogen [OH(H)] of the carboxylic acid headgroup. Two peaks can be identified OH(H) - H_2O pair indicating that two ordered shells of H_2O form around OH(H). At least two or more peaks are discernible for the hydroxyl oxygen [OH(O)] - H_2O pair as well as for the pairs of the carbonyl oxygen C=O(O) and carbonyl carbon C=O(C) with H_2O . Upon examination of the first methylene group (C2), as well as subsequent methylene groups (C3-C12), we observe one distinct peak that shifts to greater distances as we traverse along the chain. This can be expected since H_2O will be further away the higher we are positioned on the chain.

Deuterium Order Parameter

During investigations of monolayers or bilayers, which contain molecules with long alkyl chains, it is often desirable to characterize the order of the chains relative to a reference axis. Experimentally, one may determine the Deuterium Order Parameter from NMR experiments of lipid bilayer systems. In this experiment, lipid molecules are selectively deuterated and the angle made from deuterium to the carbon backbone is determined relative an axis perpendicular to the bilayer. This is illustrated graphically in Figure 18. As shown below, this parameter can be determined utilizing the angle measured in NMR experiments.

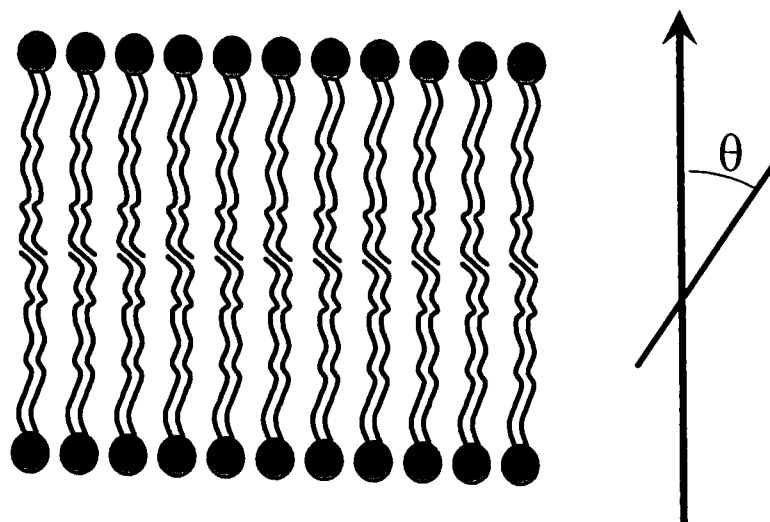


Figure 18. Deuterium NMR experimental order parameter (C-D vector orientation).

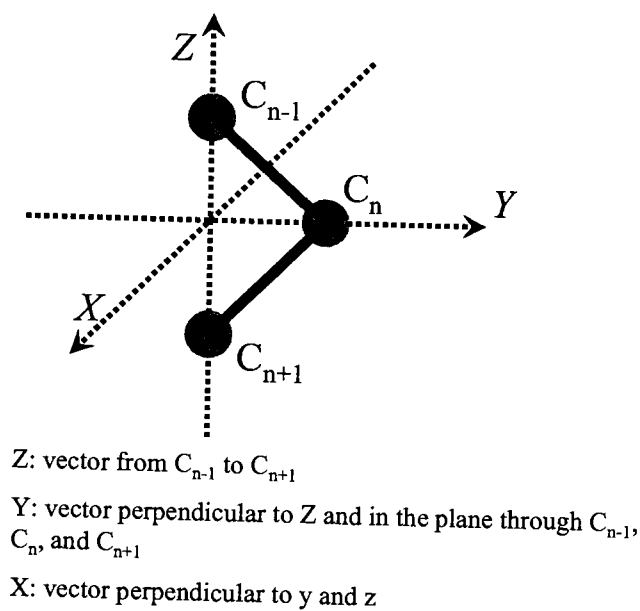


Figure 19. Bond order parameter as defined using united atom models in MD simulations.

$$S_{i,j} = \frac{1}{2} [3 \cos \theta_i \cos \theta_j - \delta_{i,j}] \quad (15)$$

in which case, θ is the angle between the i th or j th molecular axis and the monolayer or bilayer normal. In the above equation, the Kronecker delta ($\delta_{i,j}$) equals one if $i=j$ and zero if $i \neq j$. Values for the order parameter can range from 1 (indicating full order along the monolayer normal) to -0.5 (full order perpendicular to the monolayer normal).¹⁶⁹

In the case of MD simulations, where united atoms are used to model methyl and methylene groups, a different approach must be adopted as C-D bonds do not exist. Thus, a method such as that illustrated in Figure 19 must be employed in which a Z-vector is drawn from united atom C_{n+1} to C_{n-1} and a vector perpendicular to Z is drawn through the plane C_{n-1} , C_n , and C_{n+1} to signify the Y-vector. Finally, an X-vector is taken to be perpendicular to the Z- and Y-vectors. Based on these definitions the various components of the molecular order tensor parameters can be calculated.¹⁷⁰ For example, S_{zz} is determined by measuring the angle between the Z-molecular axis and the bilayer or monolayer normal. Using this method, the deuterium order parameter is related to the molecular order parameter through the following relation:

$$S_{CD} = \frac{2}{3} S_{xx} + \frac{1}{3} S_{yy} \quad (16)$$

Chain Conformation

One of the most important characterizations of the order within a hydrocarbon chain while performing MD simulations is the fraction of dihedral angles that are in the *trans* and *gauche* conformations. Using the program `g_angle` in GROMACS it is

possible to determine the angle distribution for the dihedral interactions and thus calculate the fraction of dihedrals in the *trans* or *gauche* states. Using the "Biochemical Convention", we can define the absolute *gauche* conformation, which is synonymous with the *totally eclipsed or cis state*, as the conformation where the angle of rotation between the first and fourth methylene group is 0° . In accordance with previously published work, we define dihedrals in the *trans* configuration when $\cos(\varphi) \leq -0.5$.⁴⁸ Thus, dihedral angles in the range from 120° to 240° fall into this category. Furthermore, based on the trigonometric requirement imposed above, the *gauche* conformation comprises of dihedral angles ranging from 0° to 119° and 241° to 359° . For illustration, Figure 20 provides a plot of angle distribution as a function of the dihedral angle. In this example, the first dihedral angle closest to the fatty acid headgroup for eicosanoic acid was monitored and the results represent the average for all 128 fatty acids in the simulation over a simulation time of 1 ns. The largest peak, centered at 180° , is due to the population of dihedral angles in the *trans* conformation, while the two smaller peaks in Figure 20 correspond to *gauche* conformations of the dihedrals.

Translational Diffusion

In lipid bilayer and monolayer simulations it is often desirable to monitor the diffusion of individual molecules within the bilayer/monolayer plane. Even though the system may be considered to be at equilibrium, Brownian motion may occur for molecules in a monolayer or bilayer system resulting in lateral diffusion within the lamellar plane. Brownian motion was first described by Robert Brown, who observed

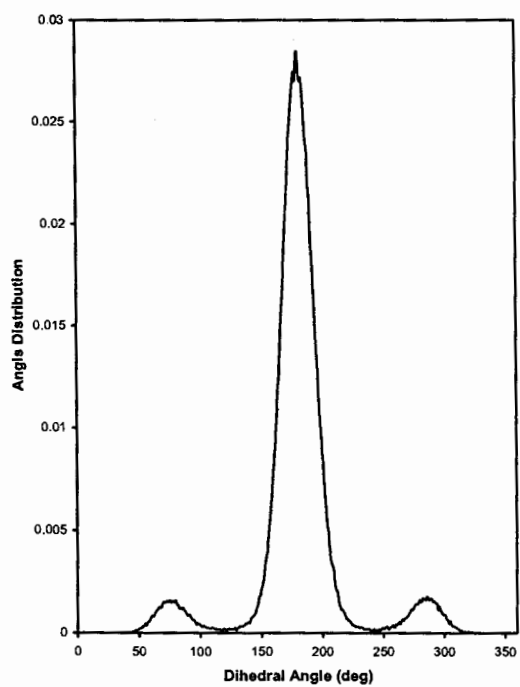


Figure 20. Dihedral angle distribution for the first dihedral set (closest to the headgroup) in eicosanoic acid.

erratic motions of particles suspended in fluids. In 1905, Einstein described these random collisions using the following relationship:

$$\langle(\Delta r)^2\rangle = \langle(r(t) - r(0))^2\rangle = 6D_o t = \frac{k_B T}{\pi\eta R} \quad (17)$$

Where $\langle(\Delta r)^2\rangle$ is the mean-squared displacement of a particle, which is averaged over time and is equivalent to the expression above that takes the difference between r at time, t , and r at the initial time 0. Further, D_o represents the diffusion constant, k_B corresponds to Boltzmann's constant, T symbolizes the temperature, η signifies Avogadro's number, and R denotes the radius of the particle.

Chapter III

Molecular Dynamics Simulations of Langmuir Monolayers

We shall see

Dr. Bruce H. Locke

Molecular dynamics simulations provide us with thermodynamic data as well as information about the conformational behavior of the system under study. In particular, we are interested in the properties and behavior of the fatty acids constituting the film or the phospholipids that make up the bilayer. Many different parameters can be calculated in order to gain an understanding of the monolayer. For the simulations of the monolayer systems we employed a canonical (NVT) thermodynamic ensemble, which enabled us to monitor the **surface tension** of the system. This allowed us to control the simulation box size in a similar manner to what is done experimentally with the boundaries used in a Langmuir trough. Initially, we start with a box size that corresponds to a monolayer packing density of $18.5 \text{ \AA}^2/\text{molecule}$. Then we incrementally increase the size of the box along the x- and y-axes until a packing density of $25 \text{ \AA}^2/\text{molecule}$ is reached. At each point in between we perform MD simulations of the system and are able to perform measurements at each packing density. Thus, we eventually obtain an isothermal phase diagram for the monolayer under investigation in which surface pressure is plotted as a function of packing density.

For monolayers, an important calculated parameter is the **tilt angle** relative to an axis perpendicular to the substrate plane. For example, MD and experimental studies of Langmuir monolayers have shown that the tilt angle increases with decreasing packing density.^{25,51} Another important parameter for characterizing chain orientation is the **bond orientational parameter (S_{ij})**. In molecular dynamics studies of Langmuir monolayers and phospholipid bilayers, it is commonly found that gauche defects occur in the hydrocarbon chains (as opposed to an all trans conformation). Usually, these occur at

the ends of the alkyl chains, however, kinks also develop in the middle and at the beginning (near the headgroup) of the chains under certain conditions. Therefore, it is useful to monitor the **fraction of gauche defects** along the hydrocarbon chain, which essentially provides the same results as calculating the **fraction of trans bonds**. We also determined the density profile along the normal of the substrate, which provides us with a measure of **film thickness**. Comparing various systems provides us with insight as to the disposition of the alkyl chains and the headgroup. We can also calculate the **radial distribution function**, which is a useful tool for monitoring the structure of liquids. It can be used to monitor the probability distribution of atoms relative to a reference atom or group. A related parameter is the **mean square displacement**, which can indicate as to whether a solid lattice has melted. It can also be used to calculate the **lateral diffusion** within the monolayer or bilayer. In addition to all of the methods listed above that are used to measure conformational behavior of the monolayer or bilayer, we always probe the energies of the system, specifically the **potential energy** and **kinetic energy**.

I. Monolayers of Eicosanoic Acid

As stated in Chapter I, one of our first objectives at the beginning of this research was to fully characterize the dynamical properties of eicosanoic acid. This was primarily due to its structural similarity to 18-MEA, which only differs from eicosanoic acid by a pendant methyl group at the 18-position of the fatty acid backbone. In addition, eicosanoic acid has been well characterized experimentally in Langmuir trough experiments as well as other studies of LB films. Phase diagrams obtained from a Langmuir trough experiment can provide extremely informative data with regard to the

interactions of a group of molecules within a monolayer. As indicated in Chapter II of this text, pressure tensors can be determined within a simulation box and surface tension for the entire system can be calculated based on these values. **Surface pressure** is then measured as the difference between the surface tension of H₂O (72 mN/m) and the surface tension of the entire simulated system, similar to the procedure carried out in experiments. A typical phase diagram from a Langmuir trough experiment for protonated eicosanoic acid is shown in Figure 21. In the Figure, one can follow the smooth transition from the gaseous state directly to the solid state for arachidic acid, which is the common name as opposed to the IUPAC nomenclature for eicosanoic acid. While this data was generated in 1939, when the purity of the materials can be considered suspect, the same phase diagram has been obtained more recently.^{14,19} In addition to isothermal phase diagrams we will also peruse other MD simulation data in order to gain fundamental understanding of the behavior of eicosanoic acid as a Langmuir monolayer.

Characterization of the Isothermal Phase Diagram

In the isothermal phase diagram shown in Figure 21, there do not appear to be any kinks or abrupt changes in the curve obtained for eicosanoic acid. Such features could indicate a phase transition or another phenomenon. Contrary to the experimental results, previous simulation studies of eicosanoic acid revealed a phase transition in the phase diagram as shown in Figures 22 and 23. The group responsible for this work published a series papers describing the nature of this transition in excruciating detail.⁴⁸⁻⁵¹ In two of these studies the transition occurs at 24 - 25 Å²/molecule,^{50,51} however, in the other two accounts the transition occurs at 21.5 - 22 Å²/molecule.^{48,49} This may be attributed to

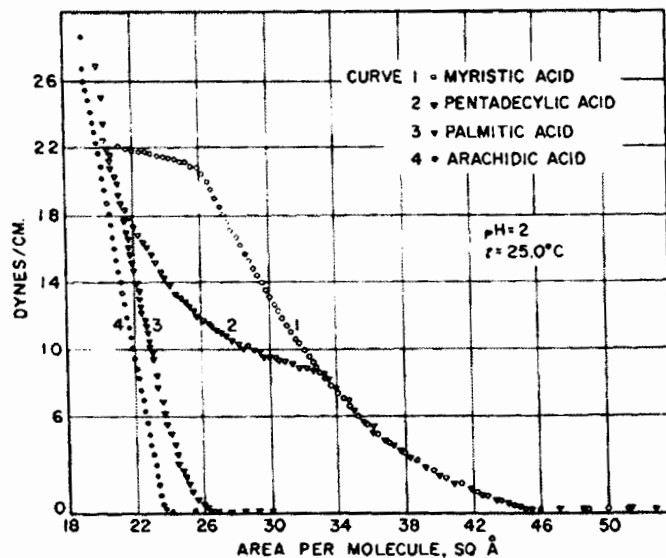


Figure 21. Isothermal phase diagram of several long chain fatty acids obtained from a Langmuir trough experiment. Please note arachidic acid refers to eicosanoic acid. Reproduced from Ref. [26].

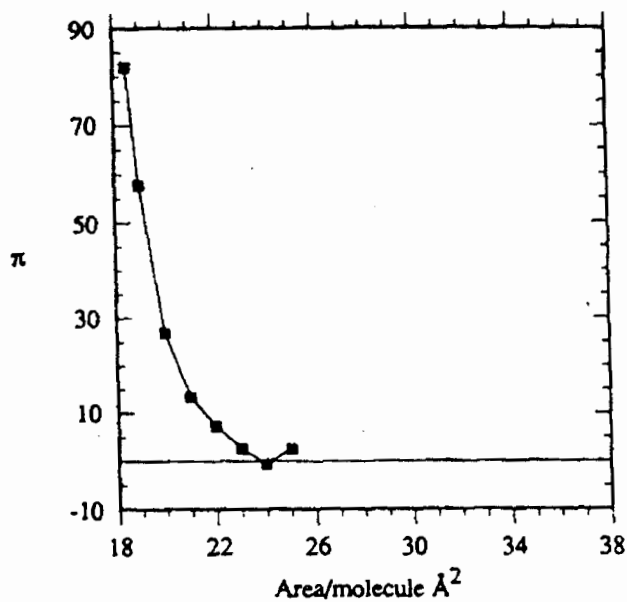


Figure 22. Isothermal phase diagram of eicosanoic acid obtained from a molecular dynamics simulation. Reproduced from Ref. [51].

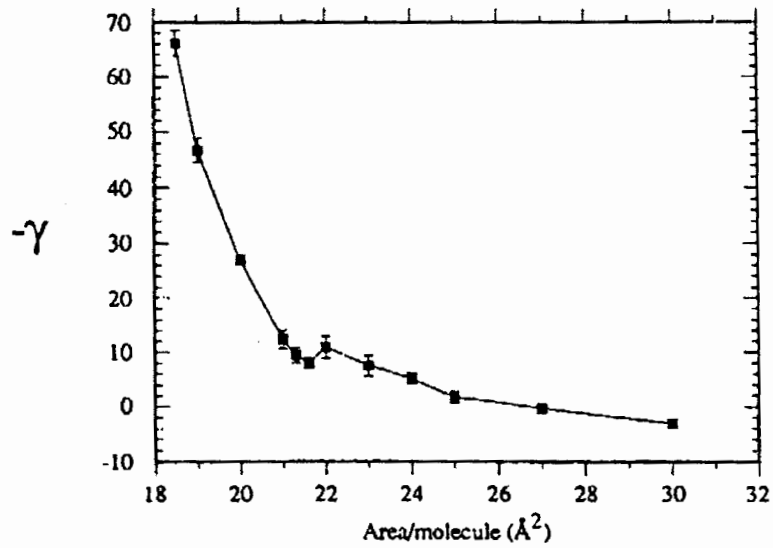


Figure 23. Isothermal phase diagram of eicosanoic acid obtained from a molecular dynamics simulation. Reproduced from Ref. [50].

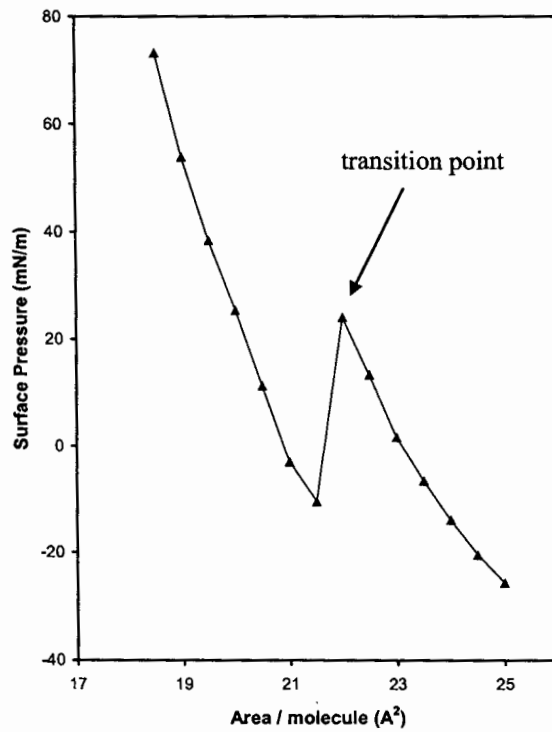
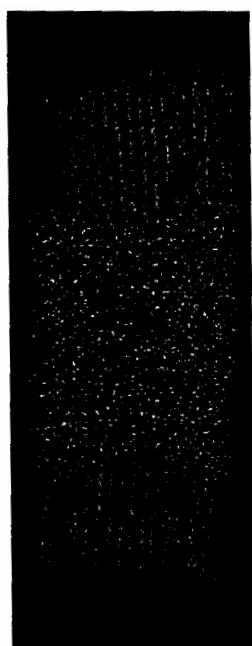


Figure 24. Isothermal phase diagram of eicosanoic acid obtained from a molecular dynamics simulation.

changes the authors made to their forcefield in between publications. As shown in Figure 24, we see a similar transition in our simulation work, however, it is more pronounced than those reported by Karaborni *et. al.* When examining such a transition, the first question that comes to mind is what could possibly cause an increase in the surface pressure in a particular region of the π -A diagram. We address this question in the following paragraphs by performing a series of different data analyses.

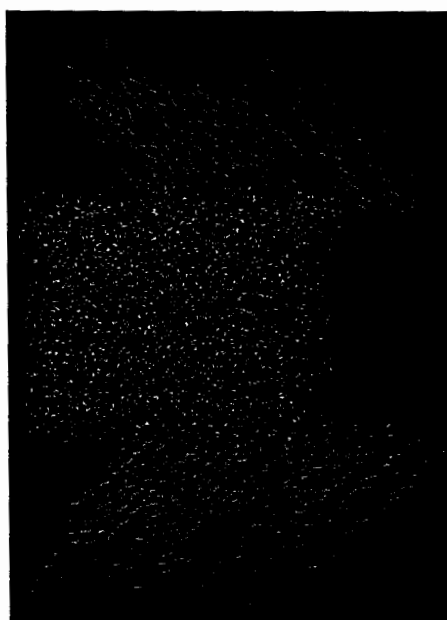
In an attempt to understand the anomaly in the simulated π -A diagrams, we performed various analyses of the MD simulation data. Typically, one visually examines the trajectory before performing any data analysis for a MD simulation set. The trajectory is essentially a movie that displays how the molecules interact over the duration of the simulation. Essentially, the trajectory represents the x, y, and z coordinates of each atom in the system as a function of simulation time. By monitoring the trajectory, it allows the observer to examine whether there were any catastrophic failures in the system. We did not observe any unusual behavior in the trajectories of the system at or near the packing density where the phase transition takes place. Included in Figure 25 are snapshots from the trajectories at three different packing densities. As illustrated in the Figure, when the packing density is decreased from 18.5 Å²/molecule to 21.5 Å²/molecule and further to 24.5 Å²/molecule, we observe the formation of collective tilt in the monolayer, which is what one should expect for such a system. In the snapshots at higher packing densities (21.5 and 24.5 Å²/molecule) it appears that there are regions in the simulation box where H₂O and the fatty acid headgroups are not interacting with any molecules rather than with each other. This is a result of the periodic



18.5 Å²/molecule



21.5 Å²/molecule



24.5 Å²/molecule

Figure 25. Snapshots from MD simulations of Eicosanoic Acid at various packing densities.

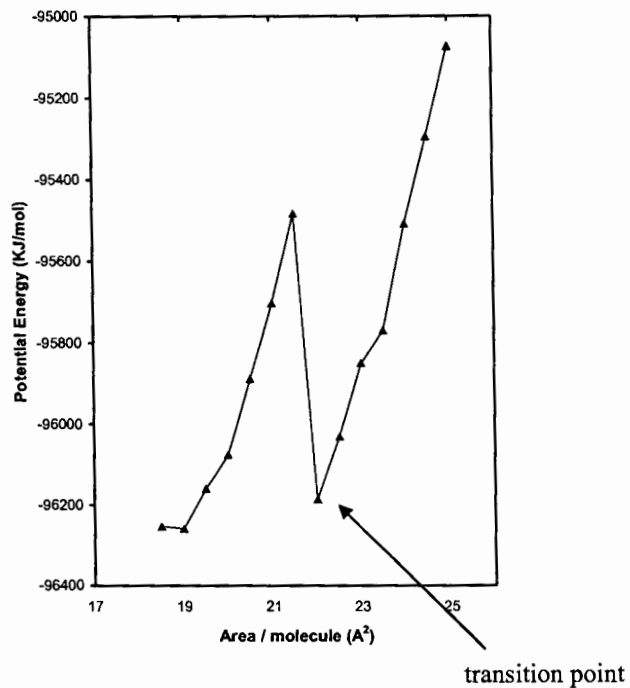


Figure 26. Potential Energy as a function of packing density for eicosanoic acid.

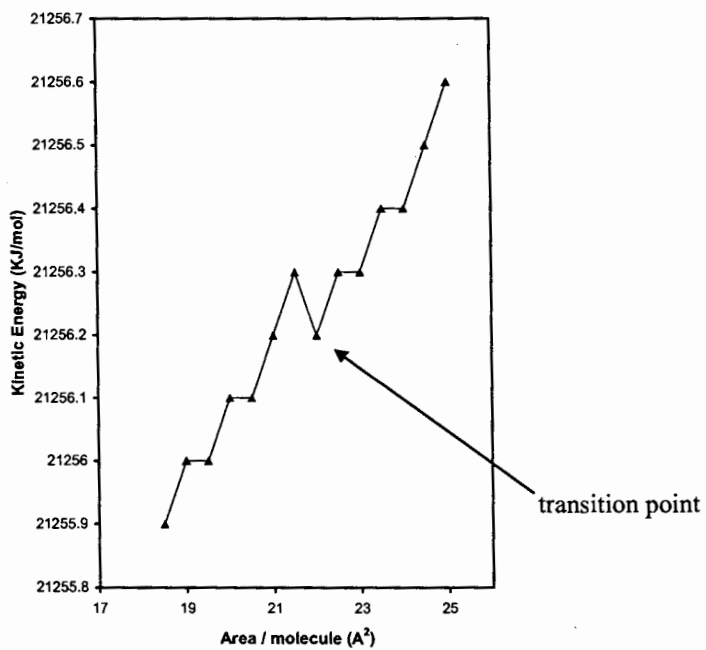


Figure 27. Kinetic Energy as a function of packing density for eicosanoic acid.

boundary conditions in which case interactions between the fatty acid headgroups and H₂O do take place, however, they are not revealed in the snapshots as these molecules are accounted for by the periodic boundary conditions and only the molecules that belong to the primary simulation box are shown. In addition to the snapshots, we also monitored the potential and kinetic energies as a function of packing density, which can be found in Figures 26 and 27, respectively. As evident in the Figures, a strange disruption occurs in both the potential and kinetic energies at 22 Å²/molecule, in accordance with the phase diagram in Figure 24. In terms of the potential energy, an increase in energy was observed up until the transition point, where a large drop in energy is experienced just before the transition point followed by another rise in energy. A similar trend can be observed with the kinetic energy, however, it is less pronounced than in the case with the potential energy.

The thickness of the monolayer was determined at all of the sample packing densities and a plot of such is provided in Figure 28. As expected, we observe a decrease in monolayer thickness as a function of packing density. This is directly in line with our expectations as we would presume that the monolayer collectively tilt in one direction, thus making the overall film less thick. One interesting aspect of the plot in Figure 28 is the behavior of the film at the transition point. At this point, there is a decrease in film thickness. The tilt angle of the eicosanoic acid monolayer as a function of packing density is reported in Figure 29. We find that the monolayer tilt follows a similar pattern to that observed experimentally; however, the tilt is slightly more pronounced in the case of the simulation studies. For comparison, Figure 30 contains a plot of tilt angle as a

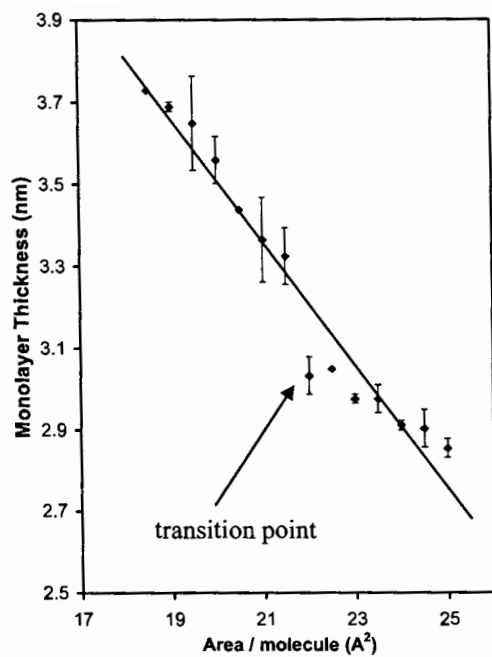


Figure 28. Film thickness as a function of packing density for Eicosanoic Acid.

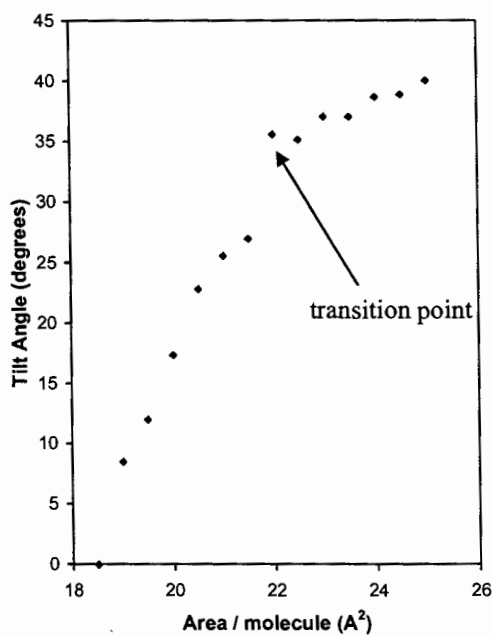


Figure 29. Monolayer tilt as a function of packing density for Eicosanoic Acid.

function of packing density for eicosanoic acid that was determined using X-ray reflection and diffraction.¹⁷ Again, in the simulation studies we see an effect on tilt angle in the region where the transition takes place. Specifically, we see an instantaneous rise in the tilt angle from 27° to 35°, which then appears to stabilize at 22 Å²/molecule and continues to steadily increase.

The radial distribution function of the third methylene group relative to the second methylene group is plotted in Figure 31 for selected packing densities of eicosanoic acid. As expected, we observe an initial peak corresponding to the first shell of atoms surrounding the reference atom followed by two peaks with lower intensities and greater widths. It has been postulated that an intensification of the first peak could be indicative of a phase transition for the material under study.¹⁴⁷ In fact, when we examine the curves for the various packing densities, we do observe an increase in peak height for packing densities of 21.5 Å²/molecule and 22 Å²/molecule. Upon examination of the second and third peaks, we observe a shift in the peaks to greater distances, a decrease in intensity, and widening of the peaks as the packing density is decreased. This can be expected given the conditions of decreasing the packing density.

In order to monitor the conformation of the fatty acid alky chains we measured several parameters. The deuterium order parameter (S_{CD}), which is commonly determined by ²H nuclear magnetic resonance (NMR) experiments of lipid bilayer systems, can provide us with some indication of the orientation of the alky tails relative to the monolayer normal. Experimentally, S_{CD} describes the orientation or angle of the

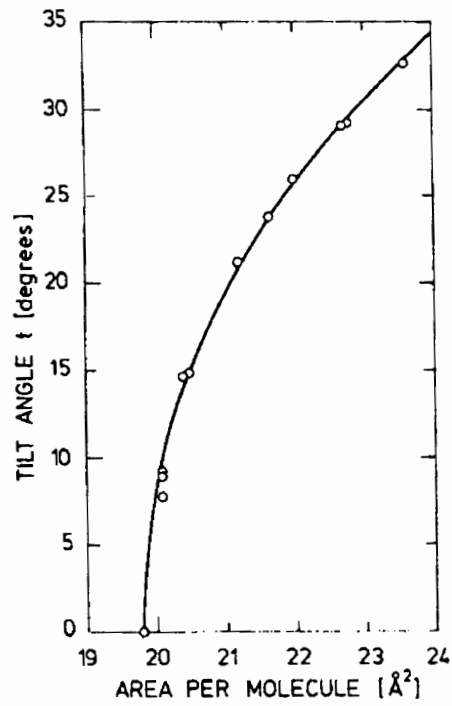


Figure 30. Monolayer tilt as a function of packing density for Eicosanoic Acid. Reproduced from Ref. [17].

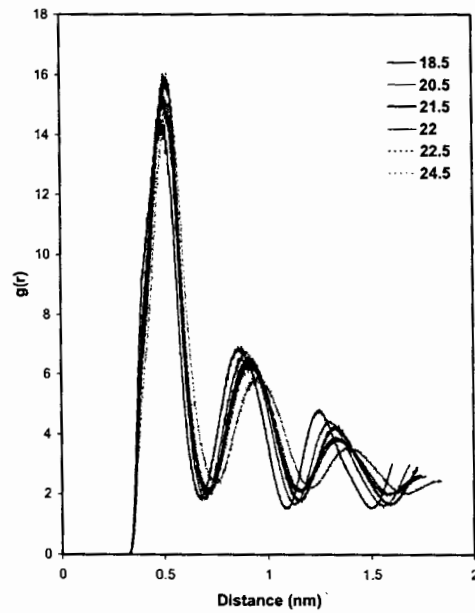


Figure 31. Radial distribution function of Carbon-3 relative to Carbon-2 for Eicosanoic Acid at various packing densities.

carbon-deuterium bond relative to the bilayer normal. As described in Chapter II, the order parameter can provide us with similar information in MD simulations in which case higher values of S_{CD} indicate higher order. In Figure 32, S_{CD} is plotted as a function of chain length for various packing densities. At higher packing densities we find that S_{CD} is greater in the middle of the chains and decreases near the headgroup and at the ends of the chains. However, at the transition point, i.e. 22 \AA^2 , and at lower packing densities the opposite effect takes place where greater order is found at the end of the chains than in the middle.

The conformation of aliphatic chains can also be characterized in terms of the dihedral angles. As elaborated upon in Chapter II, dihedral angles in the range of 120° to 240° can be considered to be in the *trans* conformation, while the remaining angles are representative of the *gauche* state. For each dihedral angle along the chain, the fraction of angles in the *trans* conformation are plotted for all of the studied packing densities of Eicosanoic Acid. These data are included in Figure 33, in which case low dihedral angle numbers correspond to the atom groups which are closest to the headgroup. Thus, from the Figure we observe that more *gauche* defects exist at the beginning and end of the chains than in the middle. This is expected as monolayer films usually contain greater order in the middle of the chains than at the ends due to stronger van der Waals interactions. Further, lower packing densities result in lower levels of dihedral sets in the *trans* conformation. This is especially evident at the ends of the chains, i.e. at the sixteenth dihedral angle.

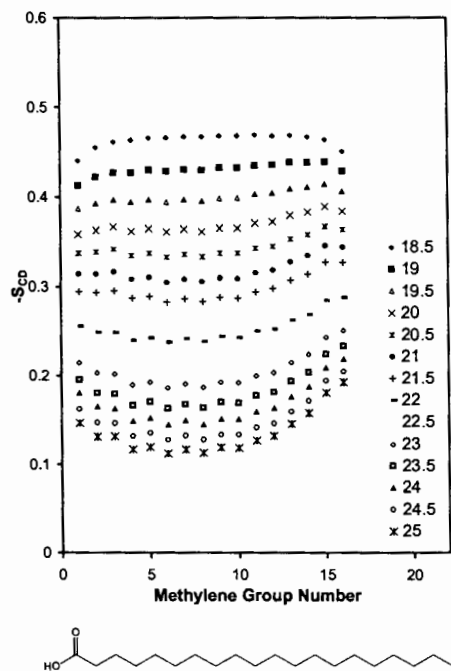


Figure 32. Deuterium Order Parameters for Eicosanoic Acid as a function of chain length at various packing densities.

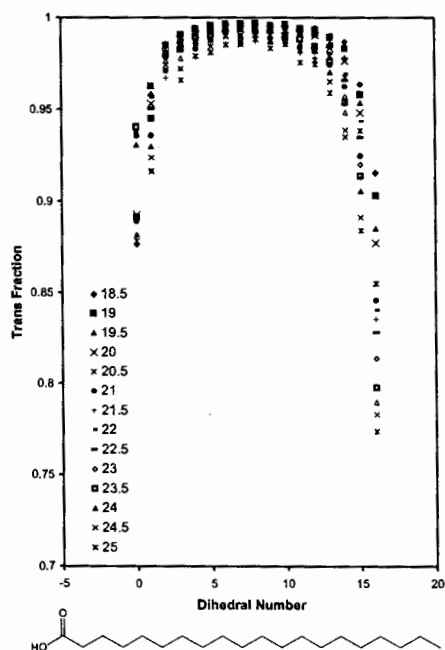


Figure 33. Fraction of dihedral angles in the *trans* conformation as a function of chain length for Eicosanoic Acid.

Choice of Forcefield

In order to assess the validity of our initial findings in regard to the phase transition, we performed the same simulations using several different parameter sets to describe the bonded and nonbonded interactions. In addition to the GROMOS-96 forcefield, we also utilized the GROMACS forcefield, which is based on the GROMOS-87 forcefield.¹⁷¹ Use of the GROMACS forcefield permits the choice of two different types of united-atom groups for CH₂ and CH₃, one in which the dihedrals are based on the GROMOS periodic function¹⁵² and another based on Ryckaert-Belleman dihedral interactions.¹⁶³ In Figure 34, these two different atom types are distinguished as **GROMACS-CH2** and **GROMACS-CP2**, respectively. The surface pressure isotherms that were obtained using the GROMACS forcefields appear less characteristic of the experimentally determined π -A diagram for eicosanoic acid than that provided by the GROMOS-96 forcefield (**GROMOS-CH2** in Figure 34). A phase transition can be identified in the isotherms, however, the fluctuation in surface pressure is much greater with these two forcefields. In addition, we examined another forcefield,¹⁶¹ which takes parameters for the methyl and methylene groups from an optimization with pentadecane⁸¹ and parameters for the remainder of the atoms from the GROMACS forcefield (Denoted as **GROMACS-LP2** in Figure 34.). The phase diagram generated by this forcefield was very similar to that obtained with GROMOS-96 forcefield with only a shift in the position of the transition by approximately 1 Å²/molecule. Overall, the surface pressure isotherm provided by the GROMOS-96 forcefield contained the least amount of noise as compared to others and appeared most like those obtained experimentally and previous simulations, thus leading to the decision of utilizing this

lipid parameterized forcefield for the experiments published in this text, with the exception of those data shown in Figure 34. One has to bear in mind that with the exception of the lipid parameter set based on the pentadecane parameterization, the other two GROMACS forcefields are optimized for protein simulations and are less suitable for long chain aliphatic molecules.

Effects of Treatment of Long-Range Interactions and System Size

As demonstrated in recent work with phospholipid bilayers, the treatment of non-bonded long-range interactions plays an important role in molecular dynamics simulations.^{76,77,75} While the treatment of shorter-range van der Waals interactions is less problematic in MD simulations, it is often necessary to employ more computationally advanced techniques, such as PME, to handle the longer-range coulombic interactions.¹⁵⁶ In this work we adjusted the distance at which these interactions can take place as well as several different methods to treat the electrostatic interactions. The rationale for this is that the anomaly might be caused by the introduction of a sharp cutoff in the forcefield such that expanding the system beyond a particular packing density, the system undergoes a sudden drop in potential energy. In order to accommodate larger cut-off values it is necessary to probe the behavior of much larger systems. Thus our typical box size, which can house two 64 lipid monolayers, is increased to accommodate two 256 lipid monolayers (each 16 x 16 molecules). In the examples that will be discussed, we utilized cut-off values that are considered reasonable in terms of accuracy without comprising computation efficiency, and also cut-offs that would not typically be employed in a simulation due to high computational cost. In all

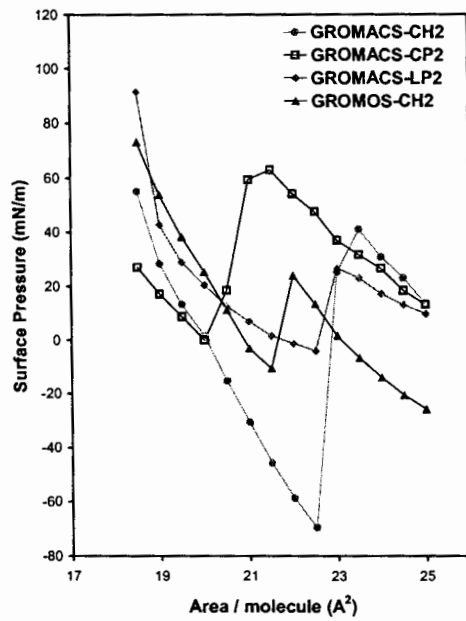


Figure 34. Isothermal phase diagrams of eicosanoic acid obtained using the indicated forcefields and united atom groups.

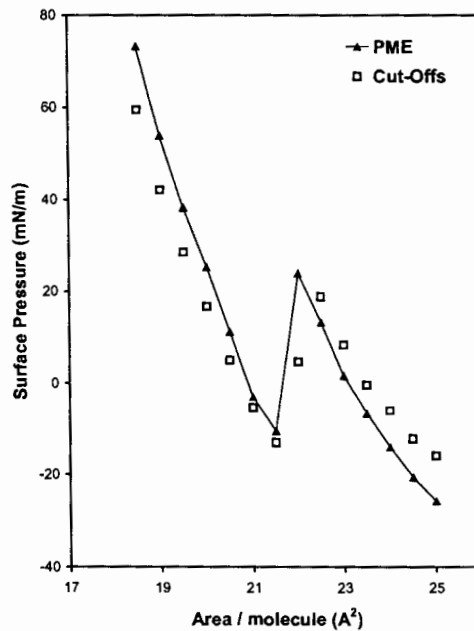


Figure 35. Isothermal phase diagrams of Eicosanoic Acid obtained using the Particle-mesh Ewald or Cut-Offs method for the treatment of long range electrostatics. $r_1 = 0.9$ nm, $r_2 = 1.4$ nm.

cases the cut-off method is employed for the treatment of the van der Waals interactions, however, we explore several different approaches for dealing with long-range Coulombic interactions.

As a first attempt to understand the consequences of choice for a particular treatment of the electrostatic interactions, we compared the use of cut-offs with the PME technique for a monolayer containing 64 fatty acids. The surface pressure data are plotted as a function of time for both sets of data in Figure 35, where in both cases $r_1 = 0.9$ nm and $r_2 = 1.4$ nm. The twin-range method was utilized in both cases in which the van der Waals interactions were cut-off at 0.9 nm and the electrostatic interactions were updated every time step up to 0.9 nm and every ten timesteps up to 1.4 nm. From this data alone we do not see any significant effect of electrostatic treatment on the surface tension of the system with both plots following almost identical paths.

In order to gain an understanding of the effect of system size on surface tension we compared a monolayer containing 64 fatty acids with one containing 256 molecules. Again, we employed the cut-off method for the van der Waals interactions and PME for the electrostatics, with $r_1 = 0.9$ nm and $r_2 = 1.4$ nm. Examination of the isothermal phase diagrams only revealed slight differences between the two monolayer systems in which the primary phase transition occurs at a higher packing density for the larger system and is less pronounced (See Figure 36). If we examine a system containing 256 molecules and compare short-range cut-offs ($r_1 = 0.9$, $r_2 = 1.4$) with long-range cut-offs ($r_1 = 1.8$, $r_2 = 2.8$) we also observe a similar transition; however, it is more obscure (See Figure 37).

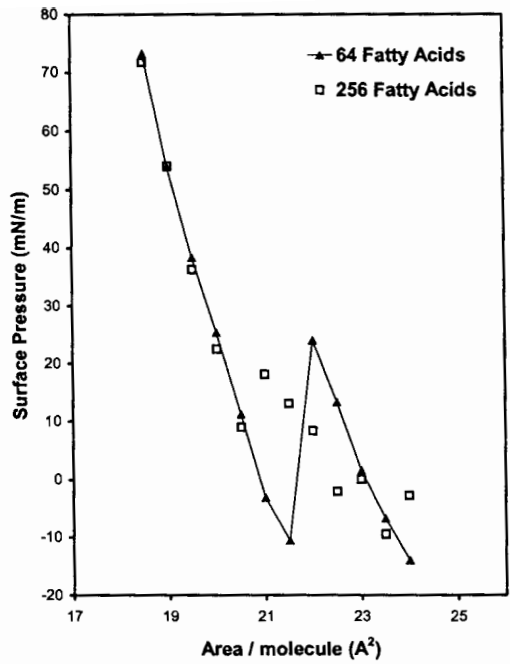


Figure 36. Isothermal phase diagrams of Eicosanoic Acid obtained using different system sizes.

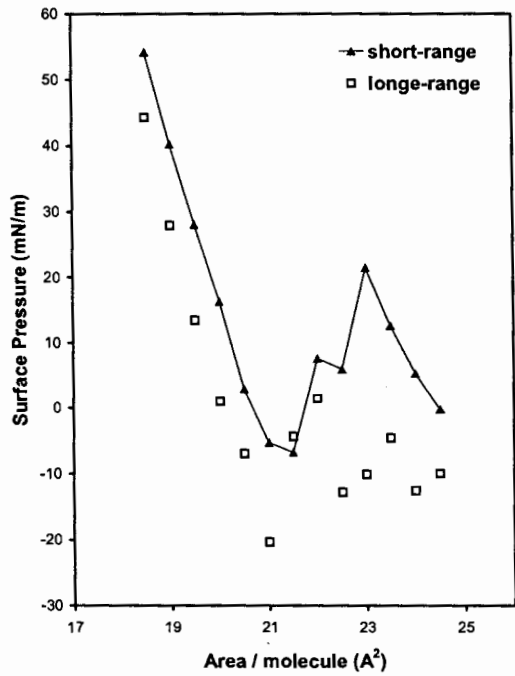


Figure 37. Isothermal phase diagrams of Eicosanoic Acid obtained using Short Range and Long Range Cut-Offs with a 256 monolayer system.

In this case, the cut-off method is used for the van der Waals and the electrostatic interactions. The same is true, in regard to the phase diagram, if we compare the same size system (256 lipids) and use the PME method for the electrostatic treatment where $r_1 = 0.9$ and $r_2 = 1.4$. It is possible that the position of the transition may be affected by the system size as larger groups of lipids may have a greater affinity for each other and may not permit them to break free of each other until much lower packing densities are reached. This could be explained by hydrophobic association where there are greater energy barriers to overcome with increasing system sizes. It should also be noted that the reaction field and switch methods were also employed, which also led to comparable isothermal phase diagrams as compared to that shown in Figure 24.

Simulation Length

In addition to monitoring the effect of the treatment of long-range interactions on the system, we also examined the effects various parameters have on the outcome of the simulation. First, we wanted to determine if our analyzed systems were at equilibrium. The equilibrium of a real system and hence in a system being studied by molecular dynamics simulations depends on the time of the process. Since most of our simulations were conducted for 1 ns we elected to examine systems that were simulated for 5 ns. Indeed, we found the same results after 5 ns, in terms of surface tension and other energy parameters, that were observed at 1 ns providing evidence that the surface tension is stabilized at 1ns. These results are shown in Figure 38 and little difference is observed between the two different time scales.

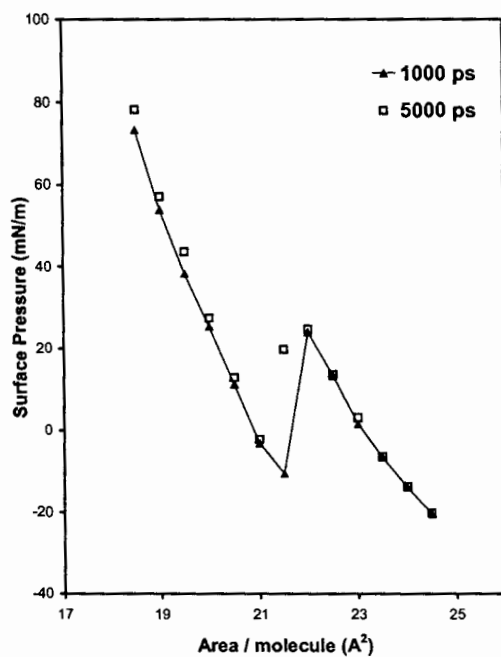


Figure 38. Isothermal phase diagrams of Eicosanoic Acid after 1000 ps and 5000 ps.

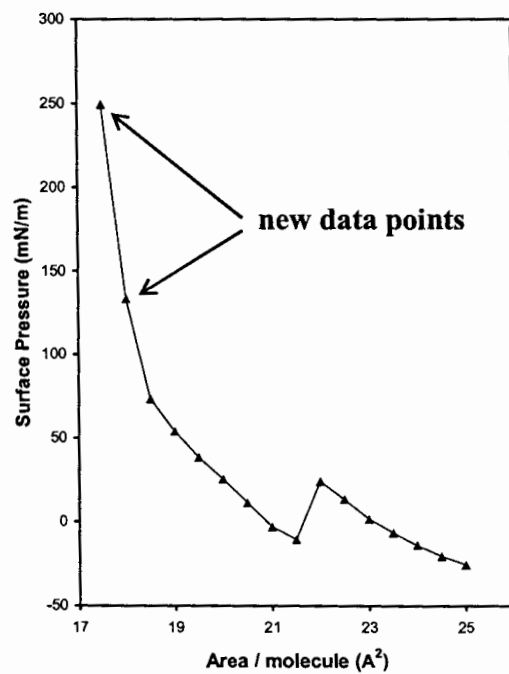


Figure 39. Isothermal phase diagram of Eicosanoic Acid after compression from 18.5 Å² to 17.5 Å².

Comparison of Expansion and Compression of the Monolayer

As compared to the work of Karaborni, the transition in our isothermal phase diagrams is exaggerated in terms of its intensity.⁴⁸⁻⁵¹ It is plausible that our system contains united-atom groups with a lower spherical density in terms of the Lennard-Jones potential. If this is true, then our system would provide π -A diagrams with lower intensities and the phase transition would appear much greater in intensity than would otherwise be expected. For example, our surface pressure plots would hypothetically only sample the packing densities from 19.5 Å²/molecule to 26 Å²/molecule, when in fact we are obtaining readings from 18.5 Å²/molecule to 25 Å²/molecule. Therefore, we monitored the behavior of the system when the monolayer is taken from a packing density of 18.5 Å²/molecule and compressed to 17.5 Å²/molecule. These results, shown in Figure 39, are similar to the results obtained from Karaborni *et. al.*⁴⁸⁻⁵¹

In our final attempt to test the validity of the phase transition in the π -A diagram, we attempted to simulate the system as close as possible to the conditions experienced in a Langmuir trough experiment. First we conducted our usual expansion MD simulations, where we begin at 18.5 Å²/molecule and incrementally increase the size of the box. We then monitored the behavior of the system by generating a series of contraction experiments where the box size was incrementally decreased from 25 Å²/molecule to 18.5 Å²/molecule. As shown in Figure 40, we find that the transition disappears indicating that two energy surfaces exist in the phase diagram. At a particular density in the expansion plot, the system discontinuously jumps from one energy surface to the other. We do not observe this jump under compression.

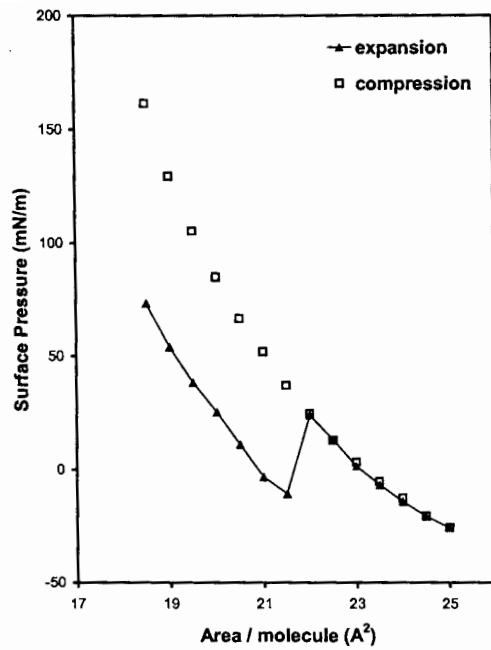


Figure 40. Isothermal phase diagrams of Eicosanoic Acid obtained by expansion and compression of the simulation box.

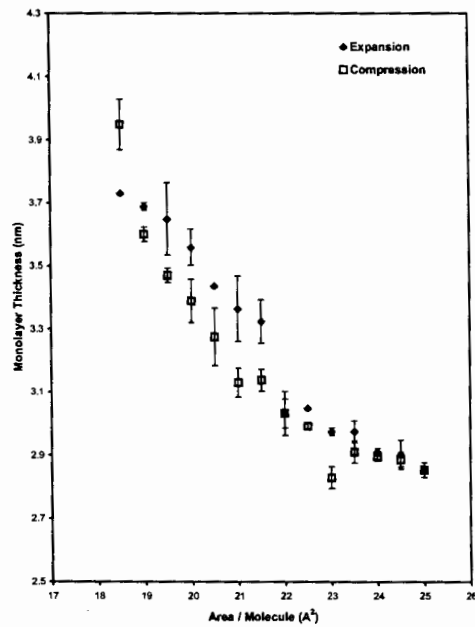


Figure 41. Film thickness as a function of packing density for eicosanoic acid monolayer simulation under conditions of compression and expansion.

We also analyzed conformational data from the compression set in the form of the monolayer thickness and the deuterium order parameter. Figure 41 presents the monolayer thickness data for both the expansion and compression simulation data sets. Both series of simulations demonstrate a decrease in the thickness of the monolayer as a function of packing density. As noted earlier, there is an abrupt decrease in the thickness of the eicosanoic acid monolayer (expansion simulation) at the transition point, i.e. between 21.5 - 22 Å². In contrast, the abrupt change in monolayer thickness is not present in the compression simulation series. Clearly, there is a direct correlation between the energetics and conformational state of the system. In addition, order parameter plots at all of the packing densities for the compression simulation series is provided in Figure 42, which should be compared to expansion simulation series shown in Figure 32. Although minute differences may be discerned between the two monolayer systems, we did not observe drastic changes that would be in accordance with the difference that is observed in the isothermal phase diagram. Overall, the S_{CD} values for the compression simulations are lower than for those from the expansion simulation. An even more notable difference between the two simulation sets is the uniform distribution between packing densities for the compression simulations and the lack of uniformity in the expansion set. This is most obvious when comparing both data sets at packing densities of 21.5, 22, and 22.5 Å². In the case of the expansion simulations (Figure 42), there are larger differences in the order parameters at these three packing densities as is the case for the compression simulations (Figure 32). This may be explained as being a result of the transition that occurs in the expansion series as this phenomenon is observed at 22 Å.

Conclusions - Monolayers of Eicosanoic Acid

A series of MD simulation studies at various packing densities were completed for monolayers of eicosanoic acid in which several conclusions were drawn.

- A phase transition was observed in the isothermal phase diagram that was computed from the simulation trajectories.
- Four different forcefields were examined in terms of the generated isothermal phase diagrams. We find dependence in the computed phase diagram on the forcefield or parameter set that is employed.
- The conformational behavior of arachidic acid was thoroughly investigated by analysis of system trajectories, potential energy, kinetic energy, film thickness, monolayer tilt, radial distribution functions, trans-gauche behavior, and deuterium order parameters.
- Two different techniques were employed to obtain the isothermal phase diagrams, in which case we find a phase transition at 22 Å in the expansion series of simulations, which is not present in the compression simulations.
- Conformational comparisons were made for the expansion and compression simulation data sets in terms of the monolayer thickness, monolayer tilt and the deuterium order parameter (S_{CD}). In accordance with phase diagrams, a conformational change is evident in the expansion simulations but not in the compression data set.

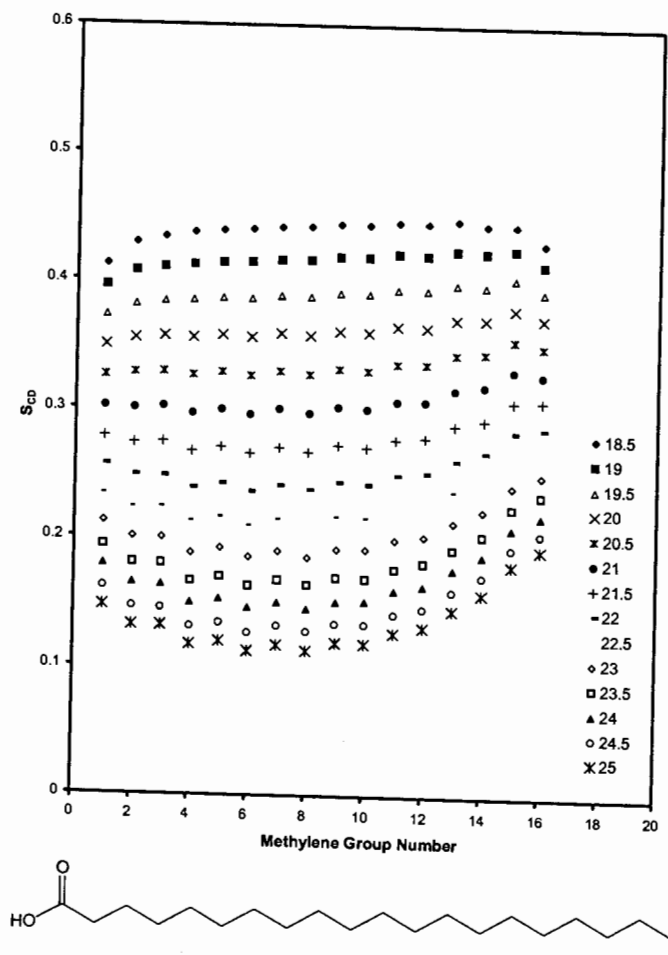
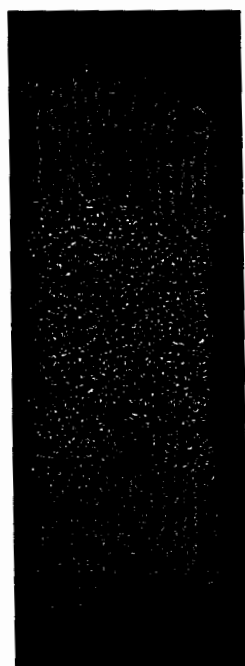


Figure 42. Deuterium Order Parameters for eicosanoic acid (compression simulation) as a function of chain length at various packing densities.

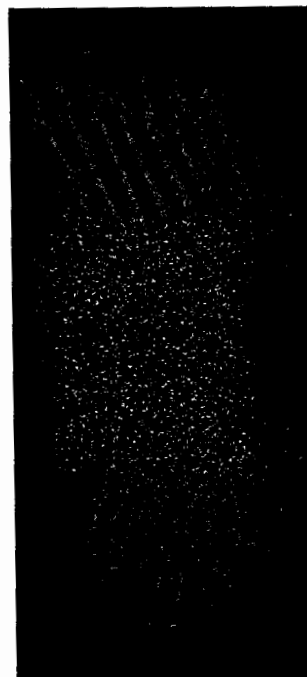
II. Monolayers of 18-MEA

The same analysis that we performed for eicosanoic acid was also completed for 18-MEA. First, we examined the trajectories of 18-MEA to determine if any unusual behavior occurs at the various packing densities. Snapshots from the 18-MEA trajectories are provided in Figure 43 for selected packing densities. Similarly to what was found with eicosanoic acid, we observe a collective tilt in the monolayer when the packing density is decreased. Upon visual observation, we find more disorder in the 18-MEA monolayer and even cases where fatty acids extrude from the body of the monolayer. This is presumably to steric effects, which are introduced as a result of the methyl group at the end of the alky chain. As shown in Figure 44, a similar pattern as was seen with eicosanoic acid was observed in which we found a decrease in the thickness of the monolayer as a function of the packing density. As evident in the plot, the 18-MEA monolayer is thicker than its parent compound. Based on our visual observations of the trajectory snapshots this observation is not surprising as the monolayer appears thicker due to the single molecule protrusions. In terms of tilt angle, the 18-MEA monolayer follows the same pattern as eicosanoic acid, however, there is more variation as a function of packing density as compared to the parent compound (See Figure 45).

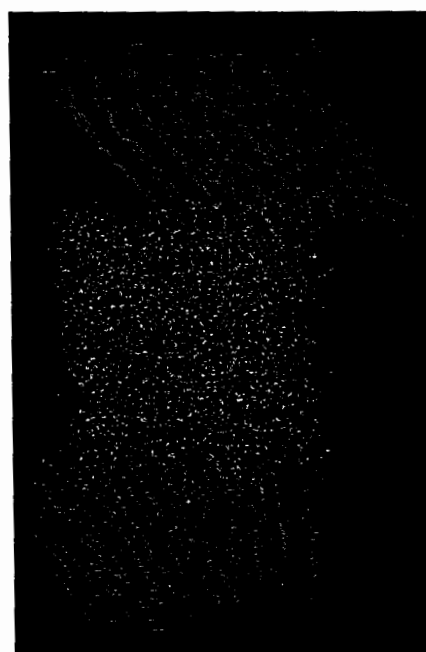
We also monitored the deuterium order parameter for 18-MEA. In this case we find that a similar pattern is observed at higher packing densities in which there is less order at the ends of the chains than in the middle (see Figure 46). However, this effect is much more pronounced in 18-MEA than in eicosanoic acid. For example, the difference



18.5 Å²/molecule



21.5 Å²/molecule



24.5 Å²/molecule

Figure 43. Snapshots from MD simulations of 18-MEA at various packing densities.

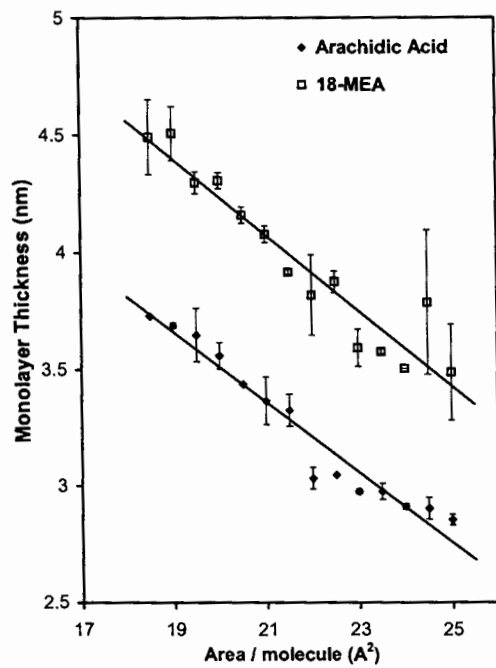


Figure 44. Film thickness as a function of packing density for eicosanoic acid and 18-MEA.

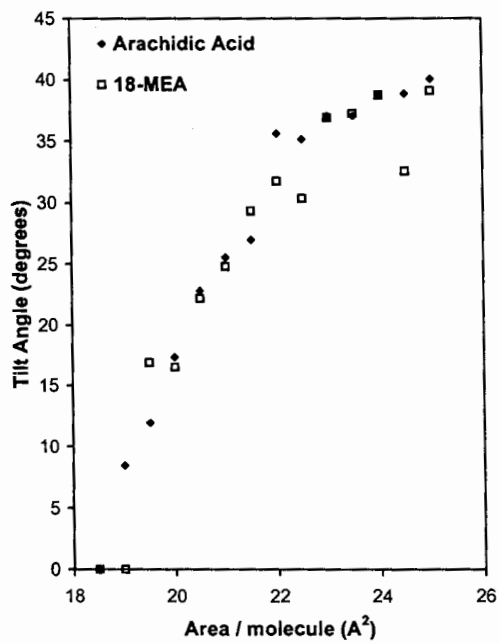


Figure 45. Monolayer tilt as a function of packing density for eicosanoic acid and 18-MEA.

in the order parameter at the middle of the chain to that at the end for a packing density of $18.5 \text{ \AA}^2/\text{molecule}$ is significantly greater for 18-MEA than for arachidic acid. Again we find that at 22 to $22.5 \text{ \AA}^2/\text{molecule}$ there is an anomalous transition that takes place in which the order is similar at all positions of the chain. When we examine lower packing densities, we find that an opposite effect takes place in which there is more order at the ends of the alky chains than in the middle. This observation is in accordance with what we found in monolayers of eicosanoic acid. Again this effect is much more pronounced for 18-MEA. Also, if we compare the order parameter at the end of the alkyl chains we see that there is greater similarity in S_{CD} for 18-MEA than for eicosanoic acid (compare Figures 32 and 46). For 18-MEA at all of the packing densities, the order parameter converges at the tail end of the alky chains. One explanation for this phenomenon is that 18-MEA may be able to maintain the same degree of order even at low packing densities. This might account for its presence in mammalian fibers where the packing density may be highly variable.

Conclusions - Monolayers of 18-MEA

A series of MD simulation studies at various packing densities were completed for monolayers of 18-MEA, which structurally differs from eicosanoic acid only by a methyl group at the 18-position of the hydrocarbon chain. We find that conformational defects are introduced by the presence of a methyl group at this unusual position along the backbone of the fatty acid. These defects are especially evident in the comparison of trajectory snapshots of both monolayers as well as in the analysis of film thickness and the deuterium order parameter. The thickness of 18-MEA monolayer films is

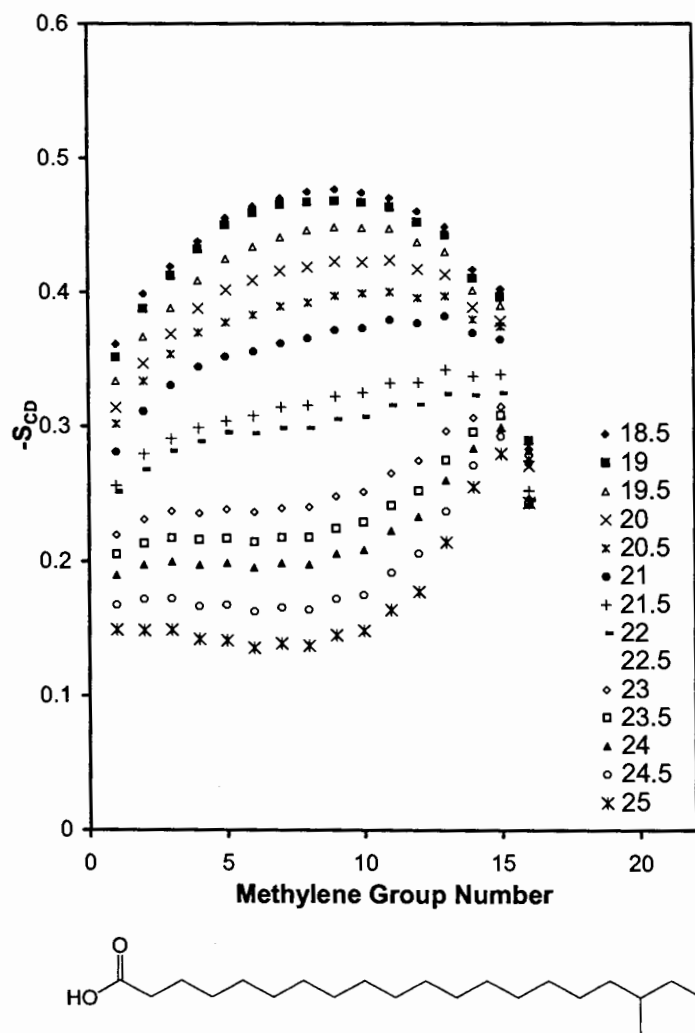


Figure 46. Deuterium Order Parameters for 18-MEA as a function of chain length at various packing densities.

significantly greater than those of eicosanoic acid. In addition, the deuterium order parameters of the 18-MEA monolayers are drastically different from the eicosanoic films. This is especially evident at the ends of the chains where much greater differences between the middle and end of the chains are observed for the 18-MEA monolayers. Most importantly, we find much smaller differences in S_{CD} between the highest and lowest packing densities for 18-MEA as compared to the parent compound. Hence, the degree of disorder at the end of the chain for monolayers of 18-MEA is within a fairly small range. This may explain the structure-property relationships of 18-MEA, which permit it to reside at various packing densities on the surface of mammalian fibers, while maintaining a similar degree of order.

Chapter IV

Molecular Dynamics Simulations of Phospholipid Bilayers

An investment in knowledge always pays the best interest.

Benjamin Franklin

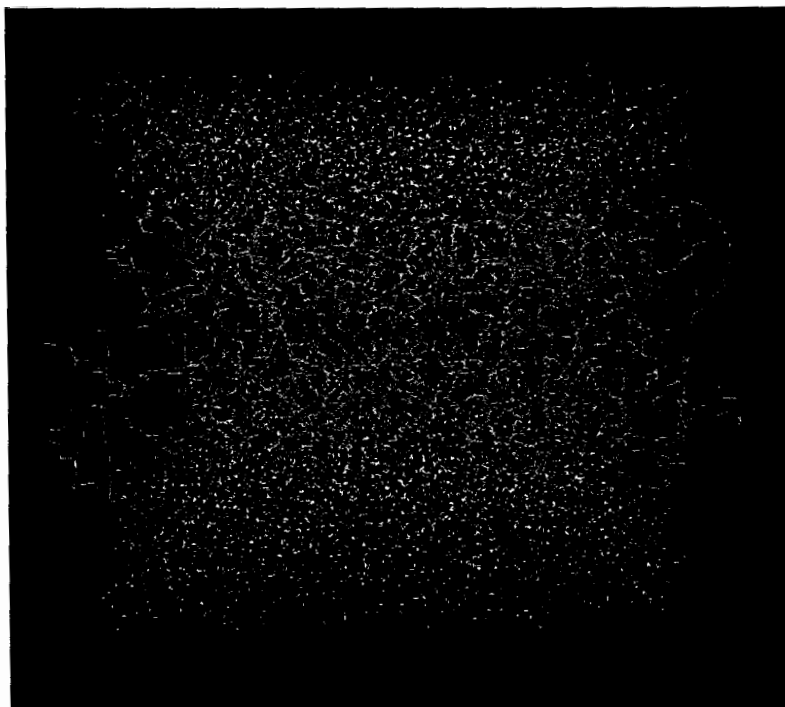
As discussed in the literature review provided in Chapter I, molecular dynamics simulations of lipid bilayer systems have evolved as one of the most thoroughly studied biological systems in the last decade. DPPC has, of course, been the most widely studied system presumably due to its ubiquitous nature in many different types of plasma membranes. DMPC, on other hand, has received less attention in the literature although it probably represents a close second or third most studied bilayer forming material. Our interest in studying both of these phospholipids stems from their abundance in the membrane of the *Halobacter halobium* bacterium, which provides residence for the integral membrane protein Bacteriorhodopsin. Thus, we have undertaken MD investigations of pure bilayer systems of these phospholipids as well as mixtures of the two components in an effort to identify dynamical properties which contribute to the observed physiological phenomenon. The starting structures of the blends were varied in order to monitor the behavior of each phospholipid in two different environments: one in which block domains of each lipid are phase segregated in the bilayer and the other in which the two lipids are distributed in an alternating matrix of the molecules. Throughout this chapter, we will refer to mixed systems of DPPC and DMPC as DPPC-DMPC I and DPPC-DMPC II corresponding to the starting configurations of the block and alternating formations, respectively (See Figure 13.) The goal of these studies is to shed light on the distinct types of behavior one can expect to see when each lipid is placed in a different environment.

By employing pressure coupling schemes in the MD simulations, the bilayer systems were studied using a isobaric isothermal canonical (NPT) ensemble in which a

constant pressure, typically 1 atm, was applied in all directions of the simulation box. This, of course, corresponds to the standard state which is experienced under normal biological conditions. Employing a pressure coupling scheme allows the box vectors to adjust as necessary in order to accommodate the pressure induction. Thus, we can monitor the box size along the x- and y-axes and calculate the **packing density** of the bilayer. The packing density represents one of the key parameters that can be determined by MD simulations and allows for comparison to experimentally derived values, which are typically obtained using neutron or x-ray diffraction techniques. Experimentally, there have been issues with respect to measurements of this kind on the L_{α} phase of bilayers. It is, of course, much simpler to study phospholipid bilayers in the gel phase using these techniques as there is a greater degree order in the system under study.

Aside from this, we are almost always interested in the conformational behavior of the aliphatic chains of the phospholipids which constitute the bilayer. The most common approach has been to measure the **deuterium order parameter** from the MD simulation trajectories. These data can be compared to experimentally measured S_{CD} values in which the quadrupolar splitting is determined from ^2H NMR data (See Chapter II for a more detailed explanation.). Thus, two links may be established between experiment and simulation. In addition to this, we can measure the **atom density** for each of the components in a simulation box, thus providing a clear depiction as to the distribution of the various atoms or molecules within the box. We also calculate the **radial distribution functions (RDF)** for several atom types that constitute the system in order to gain structural information about particular molecular groups in relation to

(a)



(b)



Figure 47. Snapshots from MD simulations of (a) DPPC and (b) DMPC after 50 ns.

another. For example, the structure of the solvent around the headgroup of the phospholipids can be determined by calculating the RDF. More specifically, one may monitor the distribution of water around the phosphorous atom in the phospholipid, thus providing information with respect to the solvation, and hence the ordered shells, formed around the headgroup of the lipids.

I. Trajectory Observations

For visual observation, we have provided snapshots for each system at the end of the 50 ns simulation. During the course of the simulations, we periodically examined the trajectories and did not observe any unusual behavior other than the normal classical interactions that take place between the all of the atoms that constitute the system. Figure 47 contains snapshots for DPPC and DMPC, in which a layer of water above and below the lipid bilayers can clearly be resolved as well as the bilayer itself in which the aliphatic portions of each monolayer are in contact with each other. When comparing the two bilayers in Figure 47, one may visually observe less order in the DMPC system where chain entanglement appears more predominant than in the case of DPPC. It is, however, difficult to ascertain these differences solely based on visual observations. Thus, a more quantitative analysis of the chain conformations is provided in a subsequent section of this Chapter. The trajectory snapshots for the mixed bilayer systems are provided in Figure 48 in which case DPPC and DMPC lipids are colored grey and orange in the images, respectively. As seen in the Figure, the positions of the lipids in the lateral plane did not shift greatly from the original starting structures. In the example provided in Figure 48a, the DPPC-DMPC I system still contains a structure in the form of lipid

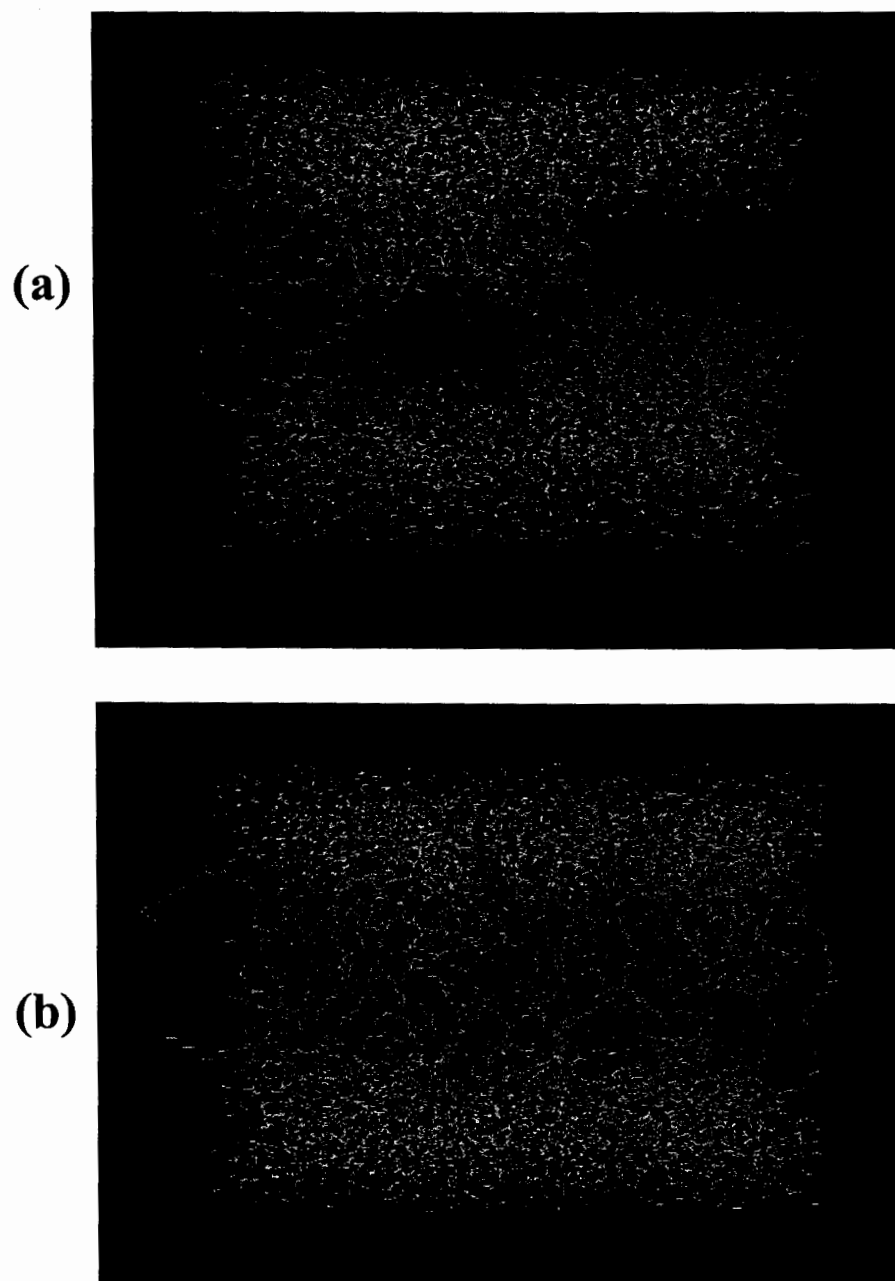


Figure 48. Snapshots from MD simulations of (a) DPPC-DMPC I and (b) DPPC-DMPC II after 50 ns.

domains in which no miscibility is observed. On the other hand, visual inspection of the system, DPPC-DMPC II, reveals a fully blended structure in which the bilayer is presumably in a form similar to its starting arrangement where the lipids were placed in a systematically alternating arrangement. It is very plausible that a simulation period of 50 ns is not sufficient enough time to permit lateral diffusion of the lipids within the bilayer.

II. Evolution of the Packing Density

The packing density of phospholipid bilayers has been a controversial subject for quite some time due to variations in the determined values.^{69,72,73,68} Primarily, this can be attributed to difficulties in the experimental approaches that have been employed to study the L_{α} phase of bilayers. This is rather problematic as often times the MD forcefields are parameterized in order to accurately reproduce experimental data such as packing density. However, more recent experimental studies have alleviated concerns about the accuracy of packing density measurements.⁷² The packing density is an extremely important parameter as it dictates many other properties of the bilayer. For example, the conformational behavior of the chains is highly dependent on the packing density of the monolayer or bilayer. This effect was observed in our studies of fatty acids (Chapter III), as it was shown that S_{CD} significantly varied from one packing density to the next. In our studies of phospholipid bilayers, we began with a box size that yielded an extremely low packing density. However, equilibrium is obtained once sufficient time has elapsed after the pressure coupling scheme has been applied to the system. Figure 49 contains a plot of packing density as a function of simulation time for all of the systems investigated. In general, we observe that a packing density of approximately 60 \AA^2 is

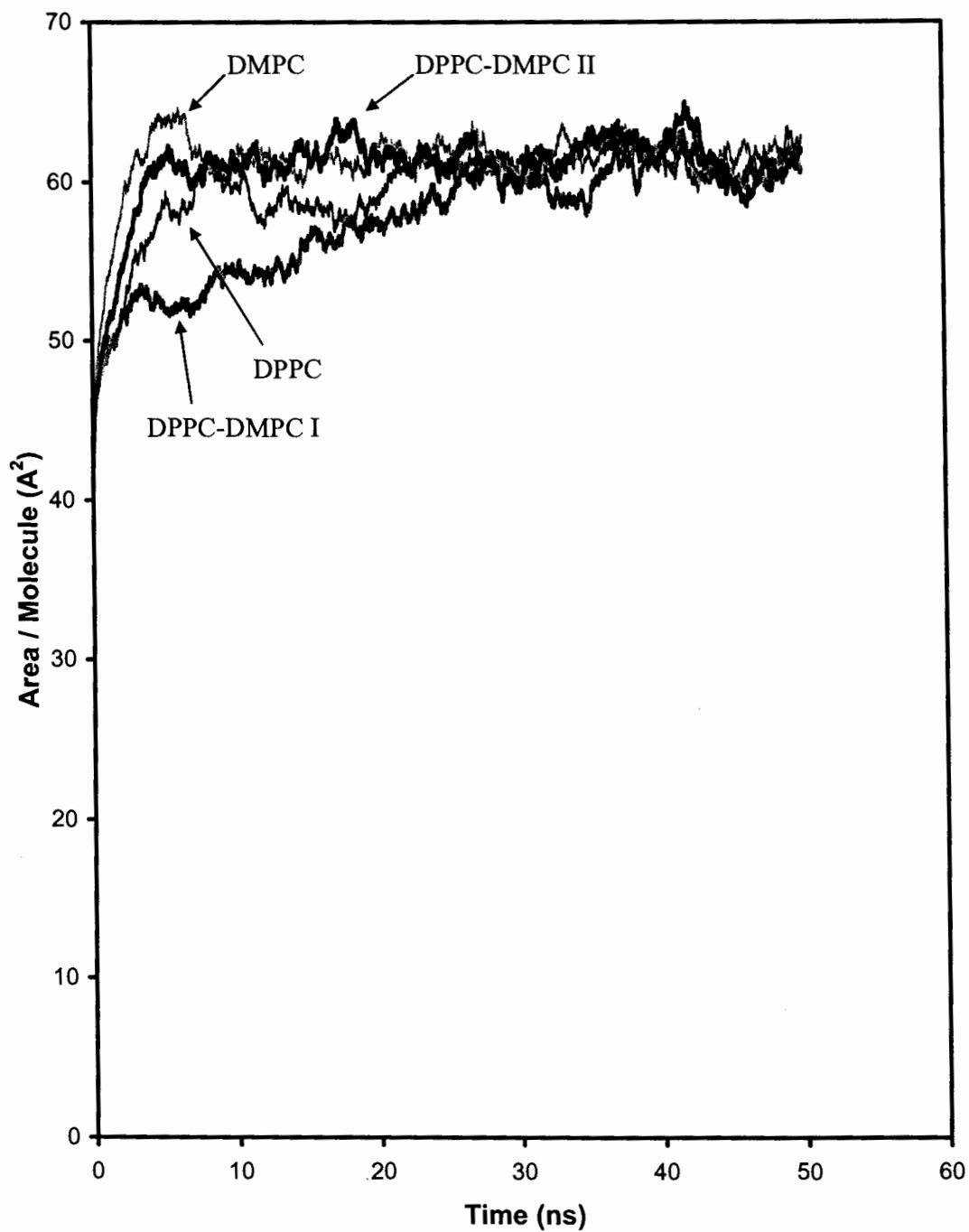


Figure 49. Packing density as a function of simulation time for lipid bilayers of DPPC, DMPC, DPPC-DMPC I, and DPPC-DMPC-II.

reached after 30 ns. This packing density is expected as this value is the same or only slightly lower than what has been determined in previous simulations of DPPC using the same forcefield and with recent simulations using other forcefields as well.^{75,74,76,77} In comparison to experimental data, we have already provided a thorough discussion of the differences that have been previously reported in the literature using several different techniques. However, it has been established that 64 \AA^2 and 60 \AA^2 are considered reliable values of the packing density for the L_α phase of DPPC and DMPC, respectively.

72

It is important to note that the system labeled DPPC-DMPC I takes longer time to reach equilibrium, approximately 10 ns more than the other bilayers. We must keep in mind that this system was started at a configuration in which the two different lipids were in a formation of separate domains. Therefore, it is very likely that this bilayer took more time to reach equilibrium than the other systems due to the immiscibility of the two different lipids. The other three lipid systems reach an equilibrium packing density value at approximately 20 ns. After this time, fluctuations of several Å^2 are observed for the remainder of the simulations.

III. Molecular Distribution in the Simulation Box

The one-dimensional distribution of molecules within the simulation box can be provided by atomic density plots along the z-axis. This type of analysis is especially useful for thickness measurements of the bilayer or water phases. As an example, Figure 50 contains density plots for DPPC and DMPC and the respective H_2O layers present in

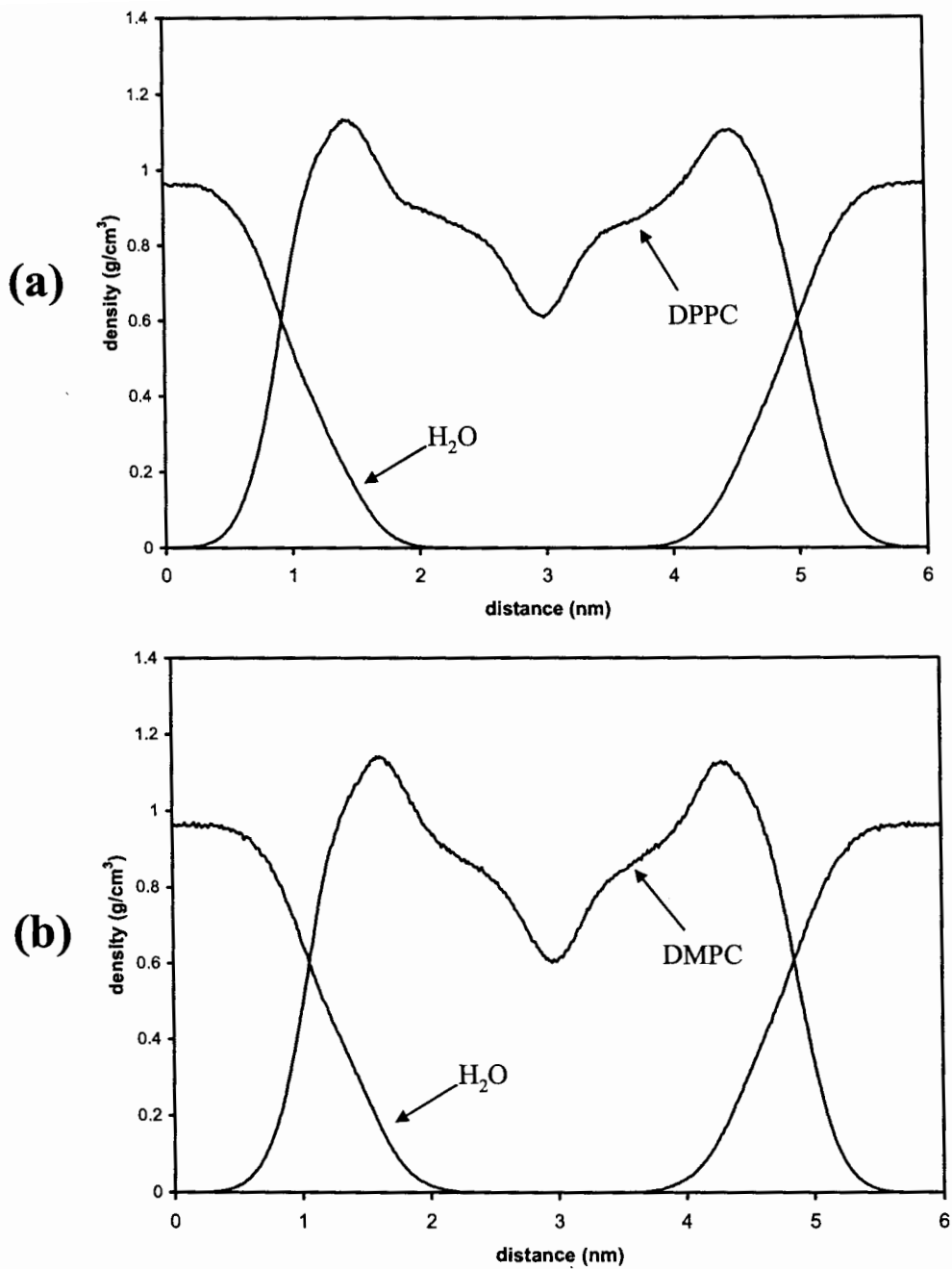


Figure 50. Plot of density as a function of distance along the z-axis of the simulation box for (a) DPPC and (b) DMPC.

both bilayer systems. For DPPC (Figure 50a), the density of lipid is zero until 0.5 nm along the z-axis where there is a sharp increase. At this point, the large rise in lipid density corresponds to the headgroup region of the phospholipid. Further along the z-axis, there is a minimum (*ca.* 3 nm) that is reached for the lipid density, corresponding to the ends of the two phospholipid chains. The increase in intensity after this point is a result of the density of the second phospholipid, which eventually reaches a maximum and corresponds to the headgroup region of the second lipid. The presence of H₂O is evident by the high intensity peaks at the top (4 - 6 nm) and bottom (0 - 2 nm) of the simulation box. We observed the same patterns in the DMPC bilayer, as illustrated in Figure 50b. While the density plots of DPPC and DMPC appear very similar, one may discern a difference in the thickness of the two bilayers. The thickness can be measured as the difference between the two points in Figure 50 where the density of H₂O and DPPC are equivalent, which correspond to the furthest ends of the headgroup regions for each phospholipid. Based on this calculation we find the DPPC bilayer to be 40.84 Å thick while the slightly thinner DMPC system measures at a 37.85 Å. The difference of approximately 2.99 Å in thickness between the two bilayers most certainly reflects a difference of two methylene groups in the chain lengths of the phospholipids. The value obtained for DPPC is in agreement with recent simulations⁷⁶ and differs from experimental results by approximately 2 Å, which have recently estimated a value of 38.5 Å.⁷²

Analysis of phospholipid distribution for the mixed bilayer systems revealed some interesting results. Figure 51 contains atom density plots for (a) DPPC and (b) DMPC in

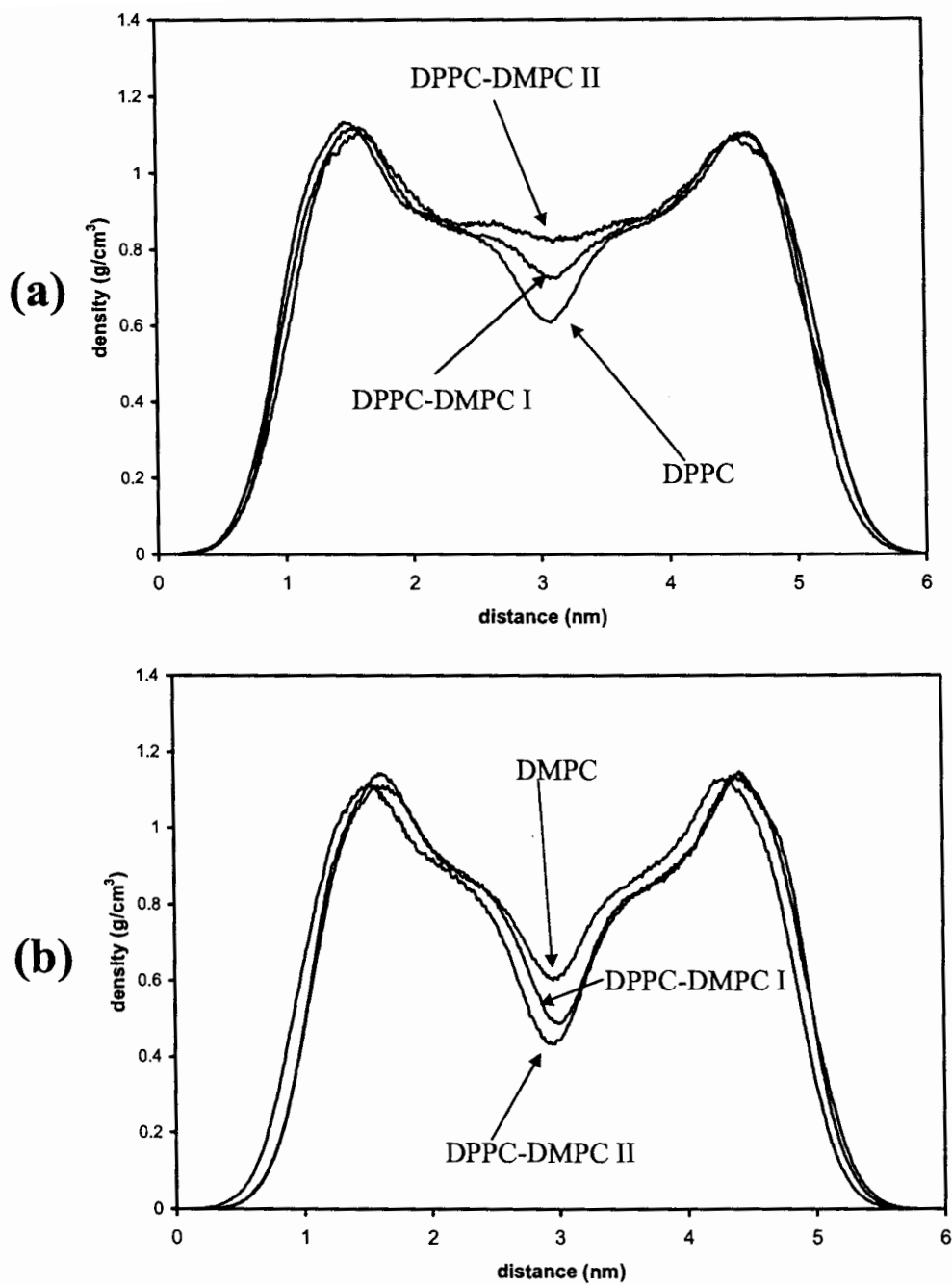


Figure 51. Plot of density as a function of distance along the z-axis of the simulation box for (a) DPPC and (b) DMPC. Each figure contains plots for the pure, DPPC-DMPC I, and DPPC-DMPC II systems.

all three respective systems, i.e. pure, DPPC-DMPC I, and DPPC-DMPC II. The line density plots for pure systems of both DPPC (Figure 51a) and DMPC (Figure 51b) demonstrate a minimum, which occurs in the middle of the plot. In both cases, this corresponds to the regions near the ends of the aliphatic lipid chains. Presumably, atoms are present at this site due to interactions between the phospholipid tails of the two monolayers. In the case of DPPC (Figure 51a), the middle region becomes greater in intensity when comparing the pure system with the two mixed systems. It is our assumption that more chain interactions occur by way of chain entanglements and overlap in the mixed bilayers as compared to a pure DPPC system. This would explain why increasing concentrations of DMPC in the bilayer would cause the minimum in the middle of the plot to diminish. This occurs for both the DPPC-DMPC I and DPPC-DMPC II systems. The disappearance of the minimum is less for DPPC-DMPC I than for DPPC-DMPC II, which is most likely because less mixing of the lipids occurs in the DPPC-DMPC I system. Recall that DPPC-DMPC I is the system with initial phase-segregated lipid domains. However, in the DPPC-DMPC II system, where DPPC and DMPC form an alternating structure, the minimum is not present. This is a clear indication that more overlap or chain entanglement is present in the DPPC-DMPC II bilayer than the other systems.

When comparing the data for DPPC and DMPC, we find complementary data to that reported above, which provide an illustration of the bilayer structure. In Figure 51b density plots for DMPC are provided for the three bilayer systems: DMPC, DPPC-DMPC I, and DPPC-DMPC II. Opposite to what was seen in the case of DPPC, we

observe that density in the middle of the two monolayers decreases when comparing the pure DMPC bilayer with the mixed systems. The peak minimum is lower than pure DMPC in the case of the DPPC-DMPC I bilayer (lipid domain structures) and even lower for the DPPC-DMPC II system (alternating lipids). Thus, we can reason that some chain entanglements and overlaps exist for DMPC in the bilayer with lipid domains (DPPC-DMPC I), but even more are present in the alternating lipid system (DPPC-DMPC II).

IV. Phospholipid Chain Conformation

To gain an understanding of the differences in conformational behavior of the aliphatic chains for the various lipid bilayer systems, we have calculated the deuterium order parameter. This data was determined for both chains of each phospholipid as a function of the chain length. As an example, the S_{CD} for DPPC and DMPC averaged over the last 10 ns of the 50 ns simulation is provided in Figure 52. The S_{CD} for each chain is plotted separately to demonstrate any differences which may exist between the two chains of the phospholipid. In each case, for DPPC and DMPC, we observe a difference in S_{CD} between Chain 1 and Chain 2 at the beginning and ends of the aliphatic portion of the molecule. This effect is more pronounced near the headgroup region of the phospholipid than at the tail portion of the chains. Also noteworthy in Figure 52 is the difference between the S_{CD} values for DPPC and DMPC. Overall, the order for DPPC is greater than that for DMPC and this is especially evident at the beginning of the chains near the headgroup and also at the end of the chains. The data obtained for DPPC are in agreement with recent experimental results⁷³ as well as with the data presented in the comprehensive review of lipid bilayer simulations by Tieleman *et. al.*⁶⁰

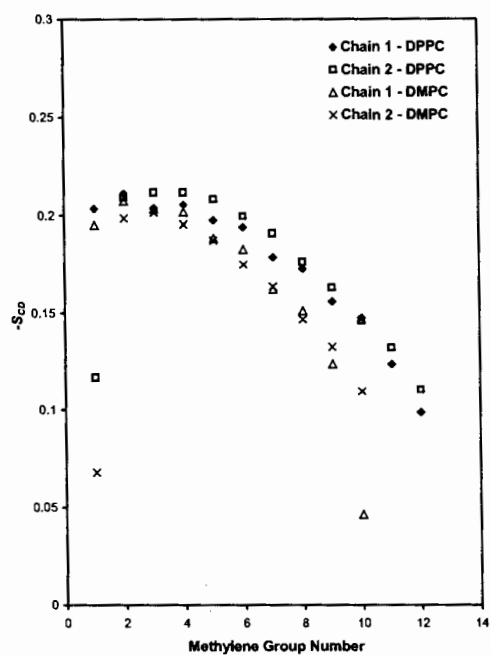


Figure 52. Deuterium order parameters as a function of chain length for both aliphatic chains of pure systems of DPPC and DMPC. Results from last 10 ns of the 50 ns simulation.

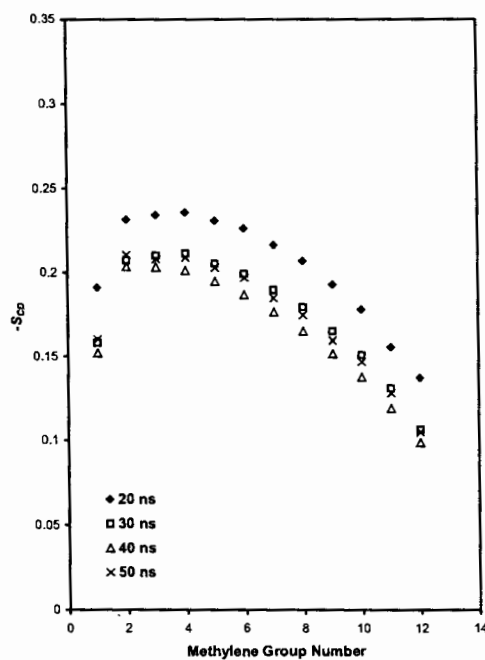


Figure 53. Deuterium order parameters as a function of chain length for the aliphatic chains (average of both chains) of a pure DPPC bilayer at various points during the simulation.

In Section II of this Chapter we found that it took anywhere from 20 to 30 ns for the packing density to reach an equilibrium value. It is reasonable to assume that the conformational behavior of the chains should also require a similar amount of simulation time to attain equilibrium. Therefore, we calculated the S_{CD} values at various points in the simulation to determine if this trend persists for this parameter as well. We monitored S_{CD} at 20, 30, 40 and 50 ns for the phospholipid, DPPC, in each of the systems that it was present. Thus, any reported values for these times refer to averages that were obtained for 10 ns prior to and including this time. For example, reported values at 30 ns represent data that was obtained by averaging from 20 ns to 30 ns. Figure 53 contains the S_{CD} values for DPPC at the indicated points during the simulation for the pure bilayer system of DPPC. We find that this system requires approximately 30 ns to reach equilibrium. Initially, we observe greater order in this system as indicated by the S_{CD} values obtained at 20 ns, however, the data at 30, 40 and 50 ns are more in accordance with each other. The same test was administered for the DPPC molecules present in the DPPC-DMPC I system, which contains the lipid domains. As evident in Figure 54, the DPPC S_{CD} values do not attain equilibrium until 40 ns. The plots obtained after 40 and 50 ns overlap and provide very good agreement, while the data at 20 and 30 ns demonstrate higher order in the bilayer. In contrast, the S_{CD} values for DPPC in the DPPC-DMPC II bilayer (alternating lipid structure) are at equilibrium at 20 ns as all reported values overlay on the plot of S_{CD} as a function of methylene group (Figure 55). This may be expected as the system with lipid domains (DPPC-DMPC I) may require more time for the chains to establish equilibrium as there height differences in the bilayer when traversing from one region to the other.

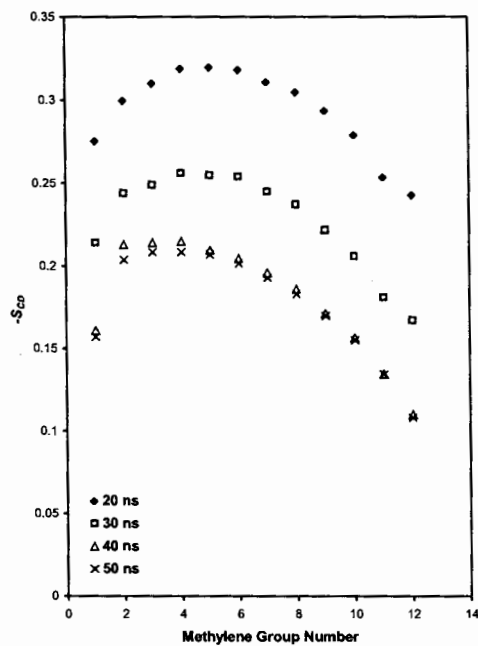


Figure 54. Deuterium order parameters as a function of chain length for the aliphatic chains (average of both chains) of DPPC from the DPPC-DMPC I bilayer at various points during the simulation.

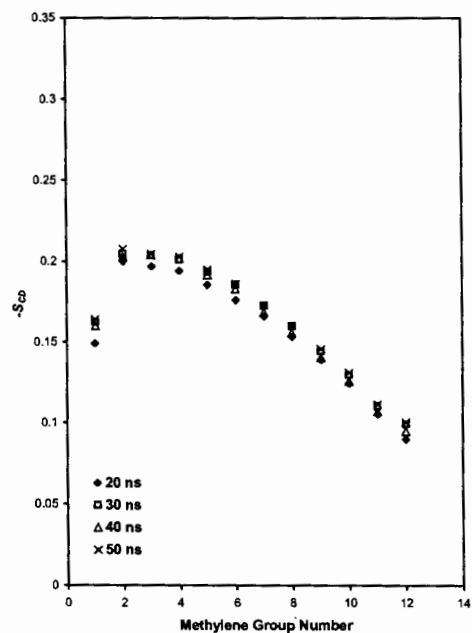


Figure 55. Deuterium order parameters as a function of chain length for the aliphatic chains (average of both chains) of DPPC from the DPPC-DMPC II bilayer at various points during the simulation.

In an attempt to probe the overall differences between DPPC and DMPC in the three different bilayer environments, Figures 56 and 57 contain plots for each phospholipid, respectively, in a pure bilayer only containing that lipid as well as the mixed systems, DPPC-DMPC I and DPPC-DMPC II. These data were obtained from averages over the last 10 ns of the 50 ns simulations to be certain that we were sampling from equilibration periods. For DPPC, we found less order in DPPC-DMPC II than in the respective pure system, which is evident in Figure 56. Less differences were observed between the DPPC pure system and DPPC in the DPPC-DMPC I bilayer. One may explain this finding as a result of the difference in S_{CD} for pure DPPC and DMPC. In Figure 52 we demonstrated that there is less order in pure systems of DMPC than DPPC. Therefore, if mixed the phospholipids in a bilayer in which domains of each lipid were present (DPPC-DMPC I), we would expect DPPC in this system to have higher order than in a corresponding system where DPPC and DMPC alternated (DPPC-DMPC II) throughout the bilayer. When we examine DMPC in a pure bilayer and the two mixed bilayer systems we observe an opposite effect as shown in Figure 57. The pure DMPC bilayer has lower order than DMPC present in the lipid domain bilayer (DPPC-DMPC I) and even less order than alternating structure system (DPPC-DMPC II). From these results, we can deduce that the order of DMPC is increased by providing some contact with DPPC domains as in the case of the DPPC-DMPC I bilayer. This effect is enhanced even more when the intimacy of contact between the two phospholipids is increased as permitted by the situation in the DPPC-DMPC II system.

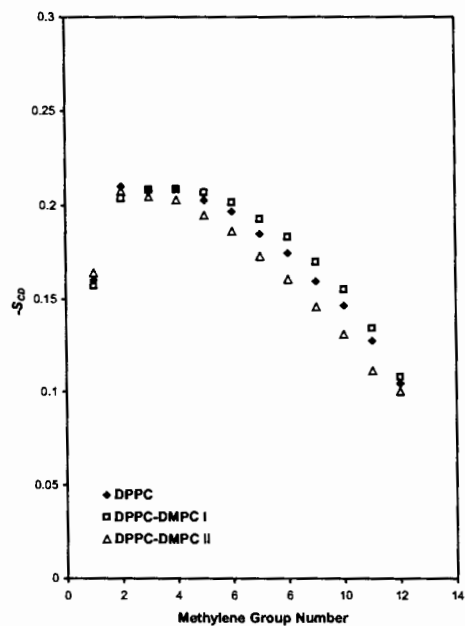


Figure 56. Deuterium order parameters as a function of chain length for the aliphatic chains (average of both chains) of DPPC from the pure, DPPC-DMPC I, and DPPC-DMPC II bilayers. Results from last 10 ns of the 50 ns simulation.

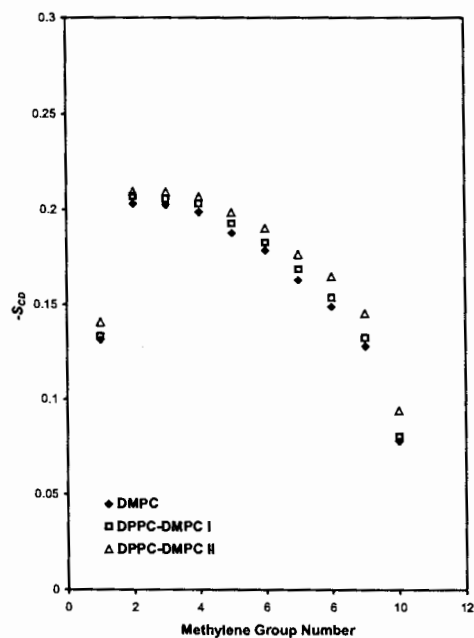


Figure 57. Deuterium order parameters as a function of chain length for the aliphatic chains (average of both chains) of DMPC from the pure, DPPC-DMPC I, and DPPC-DMPC II bilayers. Results from last 10 ns of the 50 ns simulation.

V. Radial Distribution Functions

Important structural information can be gained by analyzing radial distribution functions of various atom groups in a MD simulation. This is especially true in lipid bilayer studies as one may be interested if any ordered type of structure is formed between the phospholipid headgroup and H₂O. In addition, we can also examine the behavior of the lipid chains relative to each other in order to gain an understanding of their disposition and phase behavior. We first address the intermolecular RDF of nitrogen-phosphorous (N-P) pairs for the phospholipids of DPPC in pure bilayer system. In this case, the RDF will reveal if any structure is present when we examine the positions of nitrogens atoms in all surrounding lipids relative to phosphorous in each phospholipid. This data is provided in Figure 58 where we observe a sharp intense peak at approximately 0.5 nm followed by much less prominent peaks at longer distances. This is a typical result for a system without long-range structure and is expected in these circumstances given that the phospholipids are in the L_α phase. This data is concurrent with recent results obtained for DPPC.⁷⁷ For all of the bilayer systems studied, pure DPPC, pure DMPC, DPPC-DMPC I and DPPC-DMPC II, we observed the same results for both DPPC and DMPC. Thus, the headgroup positions and structure of the molecules are unaffected by the difference in chain length between DPPC and DMPC.

We also calculated the RDF between the phospholipid headgroups and H₂O. Typically, in systems where hydrogen bonding is present, one expects to see hydration shells surrounding the solvated species. This is normally evident by a series of peaks in

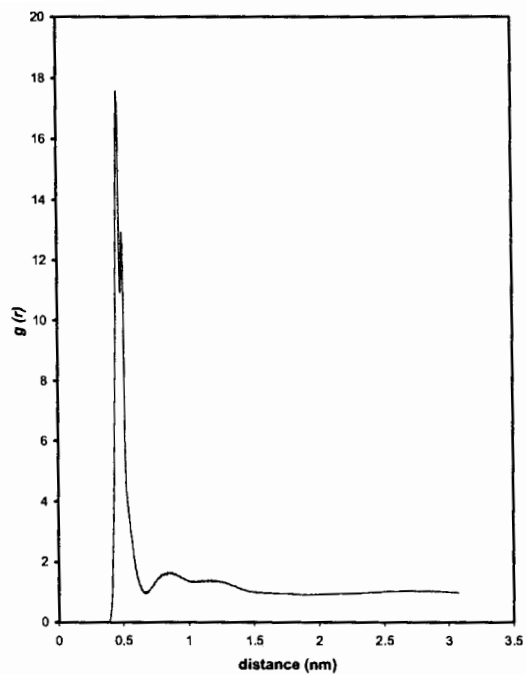


Figure 58. Radial distribution function of N-P pairs for DPPC. Results from last 10 ns of the 50 ns simulation.

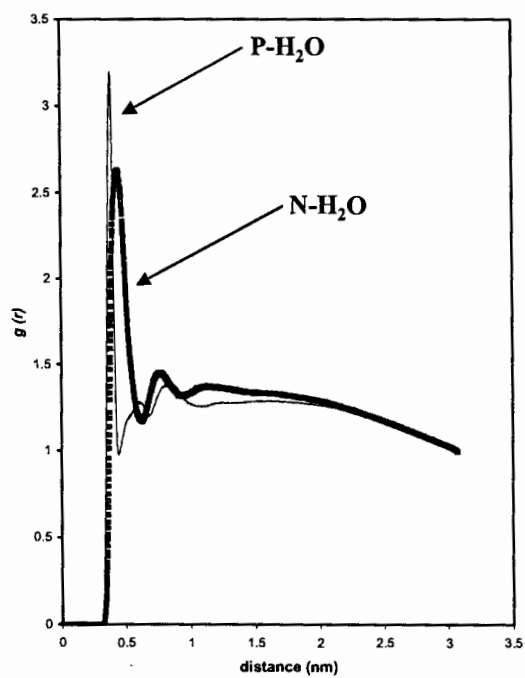


Figure 59. Radial distribution function of P-H₂O and N-H₂O pairs for DPPC. Results from last 10 ns of the 50 ns simulation.

the RDF, which is indicative of higher second order structure beyond the first solvation shell. For a pure DPPC bilayer, we provide RDF functions of the oxygen atom in H₂O relative to phosphorous and nitrogen in the headgroup of the phospholipid. As shown in Figure 59, the RDF for phosphorous and H₂O consists of an initial peak followed by two peaks of lesser intensity. This is indicative of up to three hydration shells surrounding phosphorous. In comparison, the RDF for H₂O relative to nitrogen reveals a different structural pattern in which the first peak is wider, denoting less order, and is followed by only one clearly resolve peak. Based on this observation, we may deduce that hydrogen bonding between H₂O and the phosphate group is more prevalent than is the case with the quaternary amine.

VI. Conclusions

Several systems of pure and mixed bilayer systems were investigated including DPPC, DMPC, DPPC-DMPC I, and DPPC-DMPC II. The systems denoted as DPPC-DMPC I and DPPC-DMPC II represent cases in which mixed bilayer systems of DPPC and DMPC were arranged in two different starting configurations, either an alternating pattern or block arrangement, respectively. The conformational order of these systems was quantified by several parameters, such as the molecular packing density, the deuterium order parameter, atom density, and the radial distribution function. Overall, all bilayer systems achieve a packing density of approximately 60 Å². Generally, the simulation time required to reach this equilibrium value depends on the lipid components of the membrane, with the mixed bilayer systems requiring greater equilibration periods than pure bilayer systems. In terms of the order of the alkyl chains, we find greater

disorder in the bilayers containing pure DMPC than those with pure DPPC. This may be expected as the longer chains, which are present in the DPPC bilayer, would lead to better van der Waals interactions allowing the chains to achieve greater order. As can be expected, the mixed bilayer systems demonstrate behavior intermediate to the pure systems when examining the conformational order of the chains as well as atom density plots of the phospholipids. These results also demonstrate that the order parameter may, in some cases, take longer to reach equilibrium than other MD calculated parameters. This was especially evident in the case of one of the mixed bilayer systems in which the order parameter did not reach an equilibrium value until after 40 ns.

Chapter V

Scanning Probe Microscopy of

Human Hair Fibers

Often we lose the present while preparing for the future.

Ms. Silvia Mendiola Buj

Atomic Force Microscopy (AFM) and Lateral Force Microscopy (LFM) were used to investigate the morphologic and surface changes associated with various surface modifications to human hair. These included extraction with a series of solvents, bleaching, and treatment with a cationic copolymer. The ability of these techniques to distinguish the changes in surface properties, including morphology and friction coefficient, as manifested in changes brought about by the indicated surface modifications was assessed. While topographic morphology can easily be investigated with contact AFM, LFM offers an additional tool for probing the surface distribution of oils and waxes. The removal of surface lipids from the fiber surface was accomplished using Soxhlet extraction with *t*-butanol and *n*-hexane, while the free internal lipids (within the fiber structure) were removed by extraction with a mixture of chloroform and methanol (70:30, v/v). Additionally, the surface of hair was modified with the cationic polymer, co(vinyl pyrrolidone-methacrylamidopropyl trimethylammonium chloride) [PVP/MAPTAC], and its distribution on the surface was monitored. Ambient AFM and LFM studies of surface modified and native fibers clearly indicate that when investigated as a function of tip loading force, the different modifications result in changes of the friction coefficient, which increase in the order: native, bleached, solvent extracted, and polymer treated hair. Friction images show surface variations that are interpreted as areas of varying lipid film coverage. Additionally, topographic images of the fibers show the presence of small pores, which become increasingly prevalent upon solvent extraction.

I. Introduction

Studies of the morphological, physical, and chemical properties of human and animal hair fibers have arisen due to a great deal of interest that has been expressed within the multi-billion dollar personal care and textile industries as to the fundamental properties of hair and wool, and how various cosmetic and chemical treatments manifest within the fiber surface. Consequently, a variety of surface sensitive probe techniques, including X-ray Photoelectron Spectroscopy (XPS), Scanning Electron Microscopy (SEM), and Transmission Electron Microscopy (TEM), have been used to investigate the physical and chemical properties of hair and wool fibers. Most of what is currently known about the surface properties of hair has been obtained using these techniques.

The morphological structure of human hair consists of an inner core, the cortex, which is surrounded by overlapping flat cuticle cells that are arranged in a manner analogous to fish scales or roof shingles. Several reviews have been published that describe the morphological and chemical structure of hair^{172,173}, however, the recent review on the human hair cuticle by Swift is the most up-to-date treatise on this subject, thus, his nomenclature and description of the cuticle will be drawn upon in this report.⁵ Each cuticle cell, which is *ca.* 0.5 μm thick and 60 μm square, consists of an Upper β -layer, A-layer, exocuticle, endocuticle, inner layer, and Lower β -layer. These cuticular subcomponents are lamellar and arranged in the order listed above from the exterior of the fiber to its interior. The Upper and Lower β -layers constitute what is known as the cell membrane complex (CMC), which is unlike most biological phospholipid bilayer cell

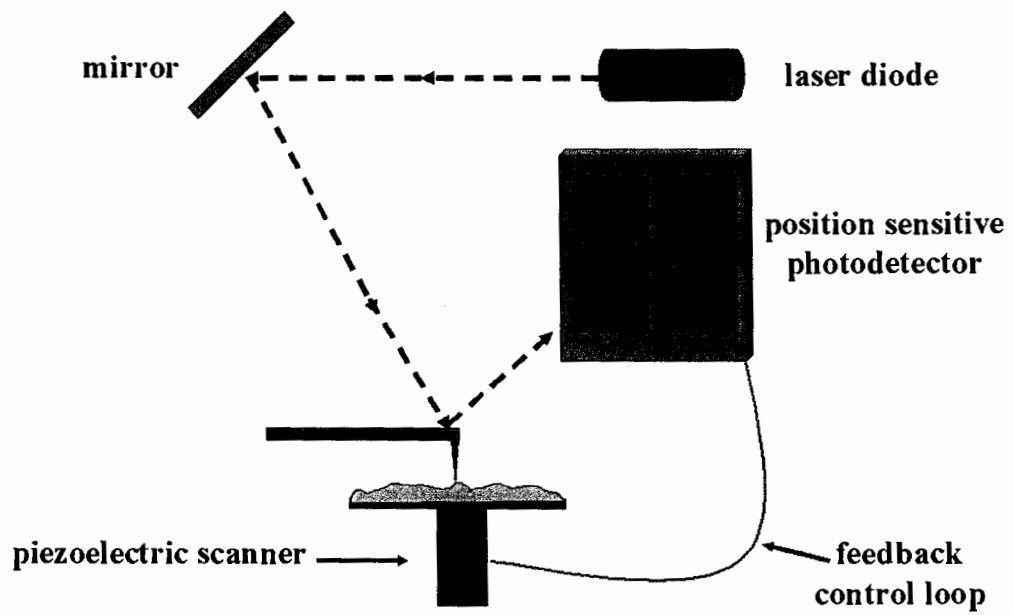


Figure 60. General scheme of a scanning probe microscope. Adapted from Howland *et. al.*

membranes. It is believed that the Upper β -layer, exposed to the surface and to overlying cuticle cells, consists predominantly of 18-methyl eicosanoic acid.³ Additionally, the cell membrane complex contains a δ layer, which is the intercellular cement that joins the Lower β -layer of one cuticle cell with the Upper β -layer of an underlying cuticle cell. The A-layer, exocuticle, and inner layer are thought to be proteinaceous in nature and have been shown to be extremely rich in disulphide bonds.⁵ The endocuticle, on the other hand, is generally low in cystine, but is also comprised of proteinaceous material. Human hair usually contains *ca.* 10 layers of cuticle cells at the root of the fiber, however, this number diminishes along the length of the fiber toward the tip direction.¹⁷⁴

The introduction of Atomic Force Microscopy (AFM) in the late 1980s¹⁷⁵ has permitted the detailed investigation of biological materials including proteins, DNA, lipids, and cellular structures, from the micron to molecular level.¹⁷⁶ One distinct advantage of AFM and related techniques is that the subject materials may be investigated under near-physiological conditions. For example, AFM can be performed under vacuum, in air, or under liquids. Thus, the common problems associated with metal coating or exposure to UHV environments can be avoided. In fact, several papers have appeared which demonstrate the suitability of AFM for studying hair fibers. For example, a considerable amount of interest has focused on quantifying the cuticle step heights of human hair,¹⁷⁷⁻¹⁷⁹ and characterizing the surface roughness of the morphological components of the cuticle, i.e. the exocuticle, endocuticle, and the A-layer.¹⁷⁸ Furthermore, hair fibers are expected to adopt quite different morphologies in humid environments compared to desiccated high vacuum environments, typically

encountered with electron probe techniques. Several studies have demonstrated the use of AFM to study hair at various degrees of hydration ¹⁷⁹ and at a range of pH levels. ^{179,180} Other studies, primarily interested in the adsorption of cationic polymers onto hair, have also been reported. ¹⁸¹⁻¹⁸⁴ Most recently, atomic force microscopy was used to image hair fibers as a function of distance along the fiber axis, i.e. from root to tip. ¹⁸⁵ These results are consistent with one of the authors' previous findings using SEM, ¹⁸⁶ in which changes in the cuticle structure were observed along the length of the fiber. Several AFM studies have been reported on wool, ^{187,188} which is structurally similar to human hair except it contains fewer cuticle layers. Parbhu *et. al.* ¹⁸⁹ used force-volume and nano-indentation techniques to measure the hardness and relative elastic moduli of the morphological components of the wool fiber. Their results were in agreement with what one would expect considering the chemical composition of the various components of the wool fiber.

In AFM, one obtains a topographical image by measuring the vertical deflection of a soft cantilever, to which a sharp tip is attached, as the tip is rastered over the surface (See Figure 60.). ¹⁹⁰ The cantilever deflections normal to the surface are representative of topographical surface features and surface hardness. In addition to AFM, Lateral Force Microscopy (LFM) is a complementary technique in which the torsional twisting of the tip and cantilever is monitored to provide a measure of the drag or friction of the tip on the surface. ¹⁹¹⁻¹⁹³ LFM can be used to study the frictional drag properties of individual hair fibers at the local level and thus, hopefully provide a fundamental understanding of

the underlying properties responsible for macroscopic combing forces on bulk fiber assemblies.

Although several AFM investigations have been completed on human hair and wool fibers, to our knowledge, only a limited amount of information pertaining to the LFM of these fiber types has appeared in the literature.^{187,178} Since LFM offers the additional capability of distinguishing different chemical functionalities of the fibers, this technique holds great promise for obtaining a more fundamental understanding of the fiber surface. We herein report combined AFM and LFM investigations of various hair fiber types including untreated native, chemically treated (bleached), delipidized (by solvent extraction), and polymer treated hair. Variations in the structural and frictional properties of the fiber surface as a function of treatment are demonstrated.

II. Materials and Methods

Subject materials

In this study we compare native with solvent-extracted and bleached hair. Oriental human hair (International Hair Importers & Products, Inc.) was used for all investigations due to its high radius of curvature as compared to other hair types, which facilitates surface scanning in the AFM/LFM instrument. The hair is supplied in bundles, 240 mm in length. We examined fibers that were 15 mm in length *ca.* 90 mm from the root of the hair. Native hair, as supplied by the distributor, was compared with hair extracted with a series of solvents. The effect of solvent extraction on hair was investigated first by treatment with *t*-butanol and *n*-hexane, each for 4 hours, then with a

mixture of chloroform/methanol (70:30, v/v) for 6 hours. In each procedure, 3 g of hair was treated with 250 mL of solvent in a Soxhlet extractor. Additionally, we examined the effect of bleaching hair by using a commercial product consisting of Clairol Professional BW 2 bleaching powder and Emiliani Professional 20 Volume clear developer.

The cationic polymer, co(vinyl pyrrolidone-methacrylamidopropyl trimethylammonium chloride) [PVP/MAPTAC], was employed to modify the surface properties of hair. It is a commercial product sold under the trade name of Gafquat HS-100 (ISP). Treatment of hair with this material consisted of soaking hair in a 1% polymeric solution followed by rinsing and drying.

For AFM studies, hair fibers were mounted to steel sample studs using nail polish. Attempts to use epoxy or other adhesives, which have been used in other studies, indicated a tendency for the epoxy to wet the fibers, particularly at the cuticle edge. Consequently, images of fibers obtained using epoxy may be considered suspect. In contrast, typical nail polish showed no tendency to wet the fiber surface but did offer good stability.

AFM/LFM instrumentation

Contact mode AFM and LFM studies were performed using a Park Scientific Instruments AutoProbe™ CP using a 100 μm piezoelectric tube scanner. The instrument used was the “beam-bounce” type in which a diode laser beam is focused onto the back

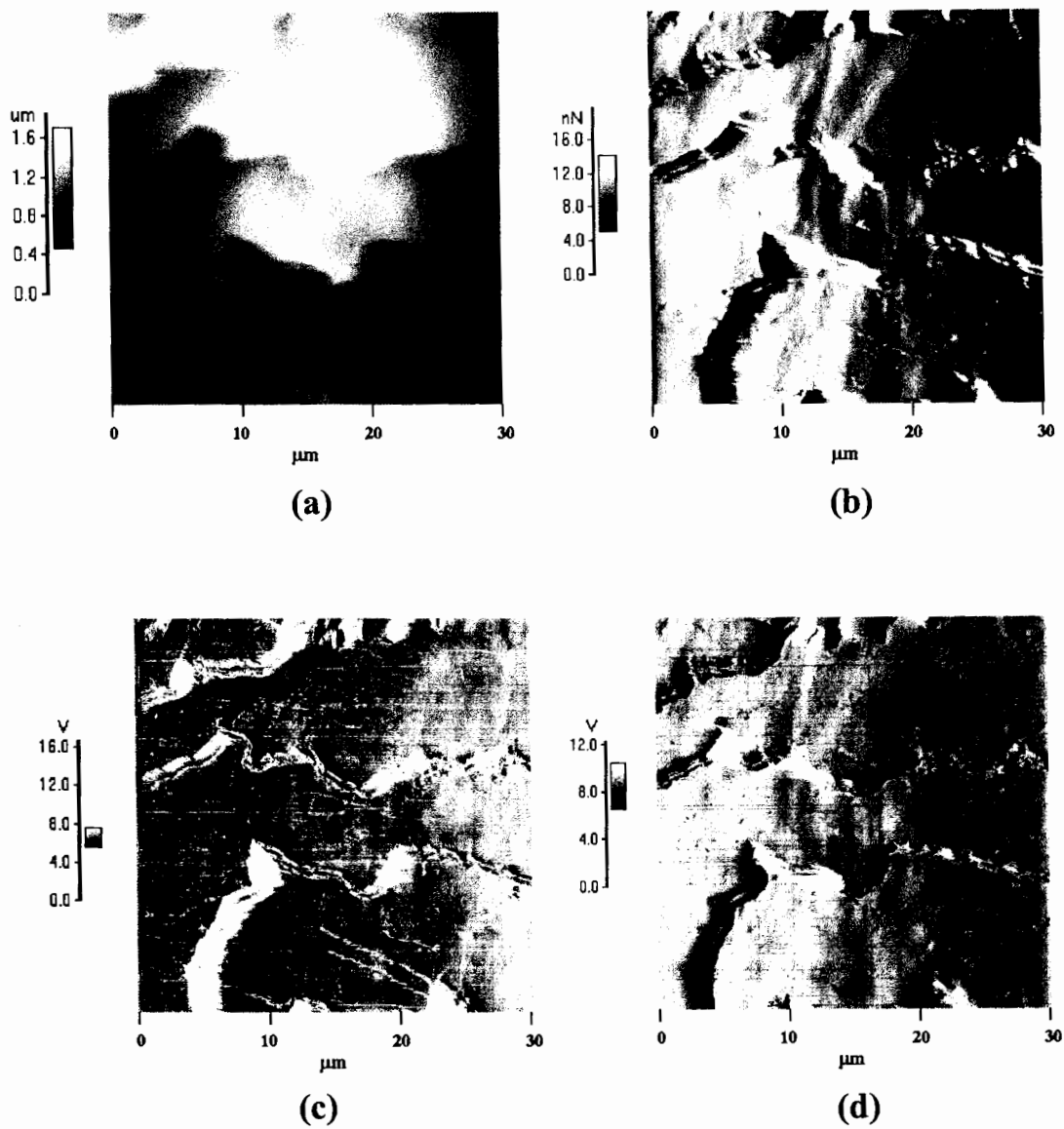


Figure 61. Typical image data scans (30 μm) obtained during AFM/LFM analysis: (a) topography, (b) error signal, (c) LFM-Forward, (d) LFM-reverse.

(top) of the cantilever. The variation in the angle of reflection is used to monitor the normal and torsional cantilever deflection by means of a four-quadrant position sensitive photodetector. Commercial triangular Si_3N_4 cantilevers 140 μm long ($k = 0.10 \text{ N/m}$) with pyramidal tips were used in the analysis. We operated the instrument in constant force mode, in which the sample vertical height is continuously adjusted via an electronic feedback loop so that the probe maintains a constant force with the sample.

Simultaneous collection of topographic (normal cantilever deflection) and LFM (torsional deflection) image data was recorded. The variation of the measured deflection signal and the deflection setpoint, known as error signal, is a sensitive probe for surface details and was collected simultaneously with LFM and topography data. The data presented is unfiltered and are representative of many images collected for each sample type.

III. Results and Discussion

A typical set of simultaneously obtained topographic, error signal, LFM-forward, and LFM-reverse scan images of native human hair is shown in Figure 61. The topographic image shown in Figure 61a illustrates the cuticle structure of human hair fibers. Figure 61b, displaying the differential error signal, accentuates the details of the cuticle surface since error signal is more sensitive to local variations and defects than is topographic data. The LFM data, depicted in Figures 61c and 61d, illustrates the torsional bending of the cantilever as it rasters across the sample in each direction. Since the LFM detector always measures positive torsional deflection as clockwise twisting of the cantilever, what appears light in one LFM scan direction will appear dark in the other

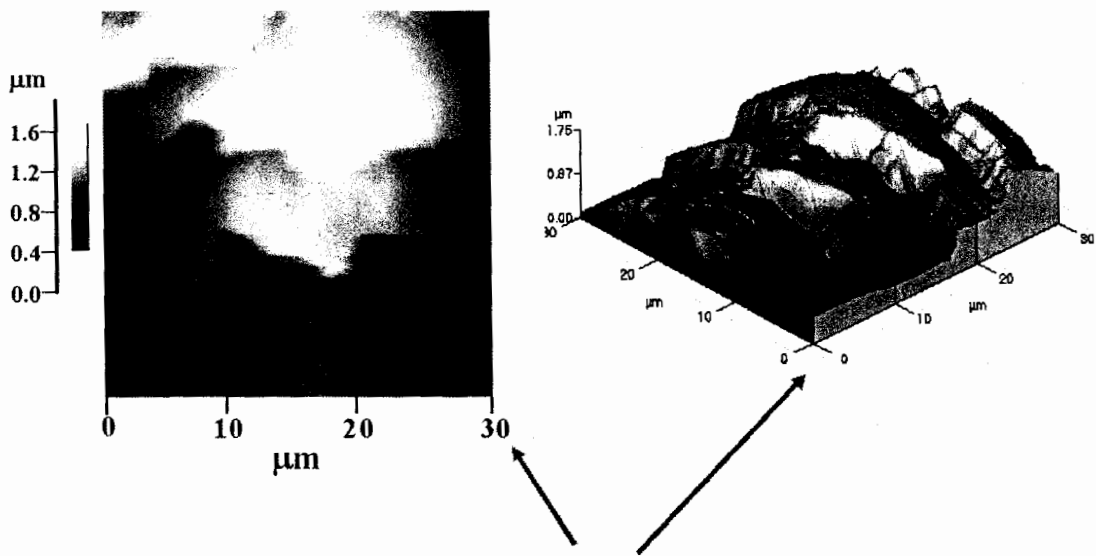


Figure 62. Three-dimensional representation of topography.

scan direction. In Figure 61c (LFM-forward), dark represents areas that are higher in friction whereas light is indicative of lower frictional regions. The opposite is true for Figure 61d (LFM-reverse), in which light corresponds to high friction and dark represents low friction. There are clear variations in friction across the fiber surface but as shown below, differences in friction between one sample type and another are significantly more pronounced. For further illustration, Figure 62 contains a three-dimensional representation of the AFM image in Figure 61a.

Microdeposits-Native Hair

When comparing the native, bleached, and solvent extracted hair we found that native hair, as received from the manufacturer, typically contained small micro-deposits on the surface as shown in Figure 63. The deposits, generally 100 nm in diameter, are characterized as having higher friction, as seen in Figures 63b and 63c, than the remaining fiber surface. One interpretation of the features may be low-profile high molecular weight oils or waxes present on the fiber surface. After solvent extraction or bleaching the number of deposits was found to decrease considerably. Due to the physical dimensions of the deposits, they may be classified as crater-shaped features. It is well known that tip defects such as holes at the apex of the tip, can cause sharp, high aspect ratio surface features to appear as craters on the surface. However, since we have seen them on many different fiber surfaces using different tips, it is clear that they are actual properties of the surface and not experimental artifact. The outside edges of the features are often seen as opposing colors in the LFM forward and reverse images indicating that the periphery of the craters are composed of a softer material than the

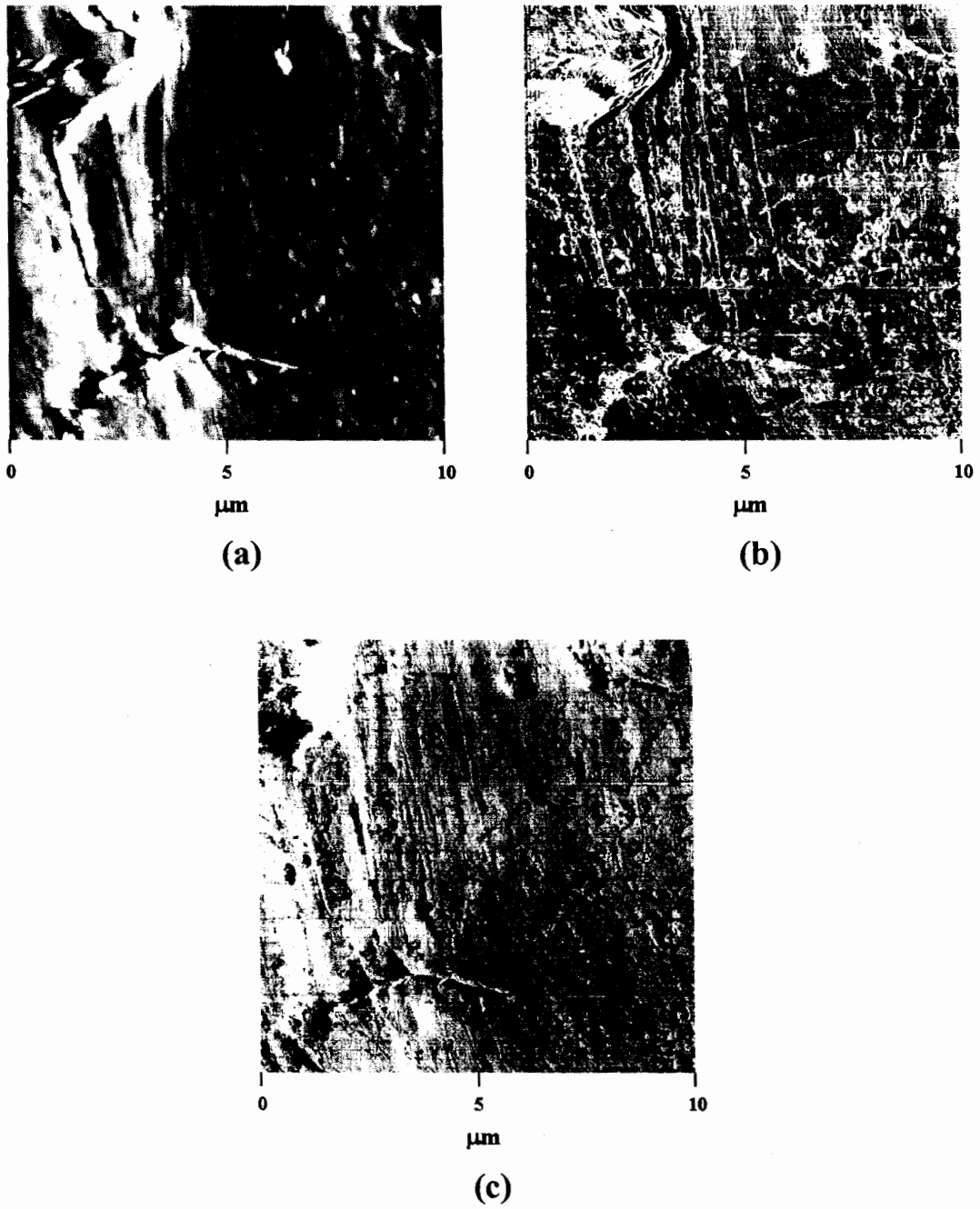


Figure 63. (a) Error signal, (b) LFM-forward, and (c) LFM-reverse images (10 μm) for virgin hair, illustrating surface deposits on hair.

remaining surface. If compared to solvent extracted or bleached fibers, we do not observe these features (See Figure 64.).

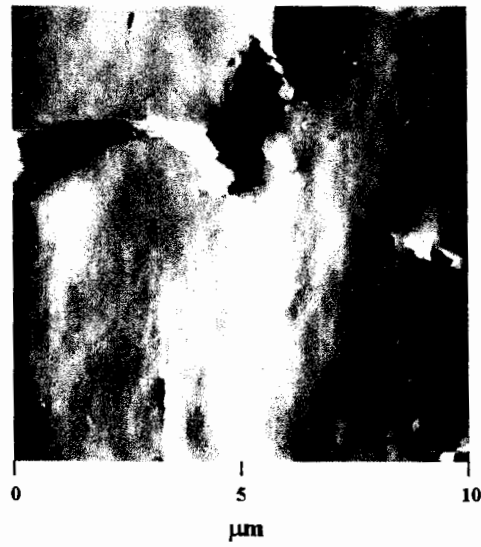
Nanopores

Another striking feature of the hair surface was the presence of a large quantity of nanopores. Figure 65 provides a representative site on solvent extracted hair in which a considerable population of nanopores can be seen. The average diameter of the pores was determined to be $150 \text{ nm} \pm 25 \text{ nm}$ with their depth estimated to be $8.0 \text{ nm} \pm 2.5 \text{ nm}$. The pore depth may be greater than the measured value due to limitations of the probe to reach the bottom of the pore (finite aspect ratio). As stated in Table I, the nanopores were found in 21% of the sites examined in native hair, 42% in bleached, and 70% in solvent extracted hair.

<u>Type of Hair</u>	<u>Frequency of Occurrence</u>	<u>No. of Sites Examined</u>
Native	21%	24
Bleached	42%	19
Solvent Extracted	70%	23

Table I. The frequency of appearance of nanopores in various types of hair.

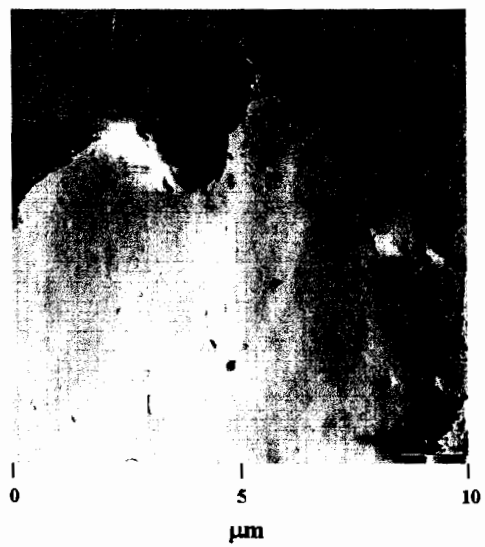
Please note that Figure 65 represents the most extreme case of visible nanopores. Often, we observed a less dense population of nanopores in a given scan area. For example, close inspection of the upper left portion in the image shown by Figure 61b reveals fewer pores than that shown in Figure 65. Overall, these features may be interpreted as surface damage, however, their presence in both native and treated fibers indicates that they may



(a)



(b)



(c)

Figure 64. (a) Error signal, (b) LFM-forward, and (c) LFM-reverse images (10 μm) for solvent extracted hair.

occur naturally on the fiber surface. As a result of oxidative/alkaline treatment or solvent extraction, many of the surface lipids are dissolved/solubilized and removed, revealing the actual hair surface with nanopores present. We attribute their increased occurrence in bleached and solvent extracted hair as resulting from dissolution of the surface lipids and exposure of the fiber surface. To our knowledge, accounts of the nanopores have not appeared in the literature, however, their presence is occasionally evident in unpublished hair micrographs.¹⁹⁴ Additionally, one can observe nanopores in the recent publication by Swift and Smith in an image they obtained 250 nm from a fiber's root.¹⁸⁵ These authors made no mention of the presence of nanopores, most likely because the majority of their scan data was for larger areas than that published herein, making it difficult to resolve the pores. It is also probable that nanopores have not been previously observed in most scanning electron microscope (SEM) studies, since a 10 nm coating of gold is usually sputtered on the hair sample in order to make it electro-conductive, a layer that could effectively mask the presence of such surface features.¹⁸⁷ The crater-shaped deposits on the native hair shown in Figure 63 may be nanopores that have accumulated surface deposits, such as sebum, which is a complex mixture of eight lipid classes present on the surface of hair.¹⁹⁵

The image of virgin hair, shown in Figure 66, demonstrates the ability of AFM/LFM to detect micro-grooves that are found on the hair surface. Again, these would be difficult to detect with a SEM, since the grooves are generally less than 10 nm in depth. Even more interesting are the patterns adopted by the micro-grooves, in which

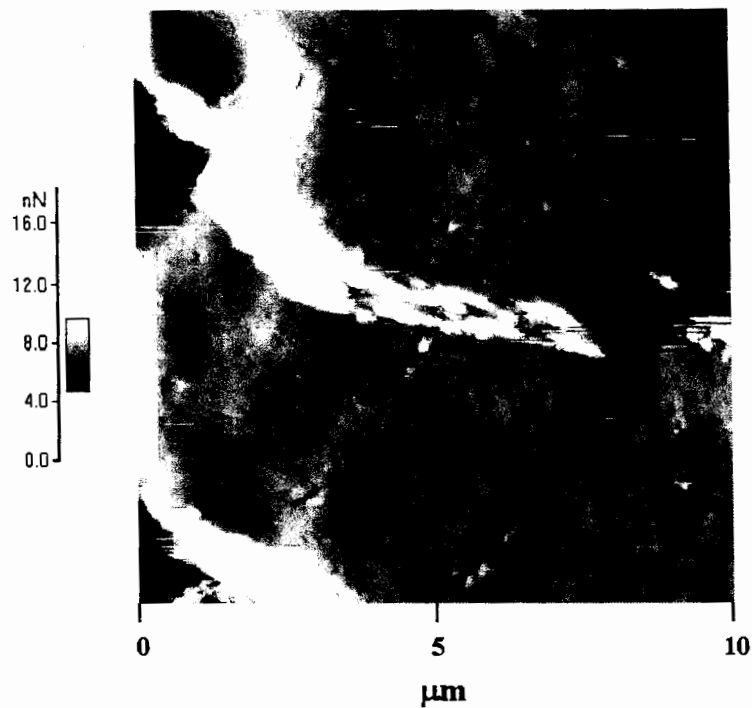


Figure 65. Error signal image (10 μm) of solvent extracted hair revealing nanopores on the hair surface.

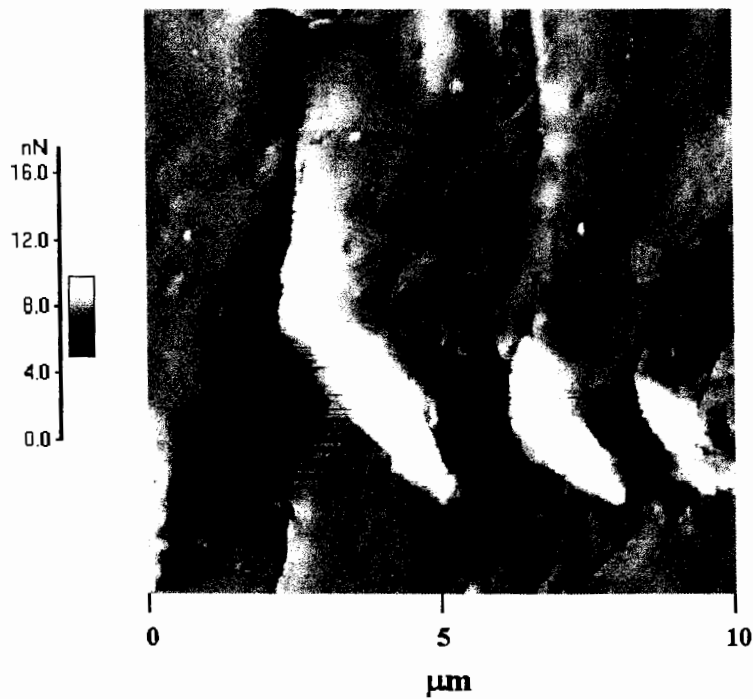


Figure 66. Error signal image (10 μm) of virgin hair revealing micro-grooves on the surface.

case the grooves are aligned with the jagged edges where the cuticle has been chipped away.

Polymer Modified Hair

A fiber surface modified with a cationic copolymer, PVP/MAPTAC, was also investigated. The copolymer was found to form crater-shaped structures on the fiber surface in 38% of the examined regions (See Figure 67.). The inner and outer diameters of the crater-shaped structures were $70 \text{ nm} \pm 11 \text{ nm}$ and $202 \text{ nm} \pm 47 \text{ nm}$, respectively. Since the diameter of the nanopores was found to be 149 nm , it is plausible that the polymer may bind preferentially to the perimeter of the pores, whose edges would presumably have a higher electric field than the more homogenous portion of the hair surface.¹⁹⁶

Frictional Information from LFM

Figure 68 shows: (a) LFM-forward scan, (b) LFM-reverse scan, (c) Difference Image, and (d) a histogram corresponding to the pixel population in the Difference Image (Forward – Reverse). Lighter colors in the Difference Image correspond to larger differences and higher friction while progressively darker-colored areas are indicative of lower friction regions. The histogram provides the number of pixels in the Difference Image that correspond to each signal difference value. For this particular image set, a bimodal distribution of the signal differences was observed with the small (white) peak at approximately 35 V corresponding to large signal differences (higher friction) and the large peak (various shades of grey) with its maximum at small signal differences (lower

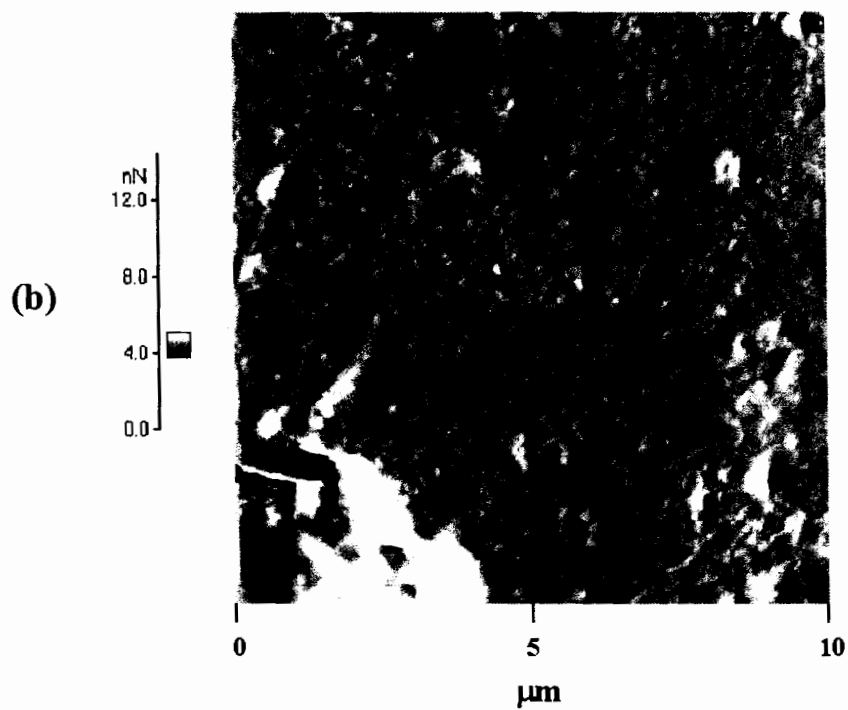
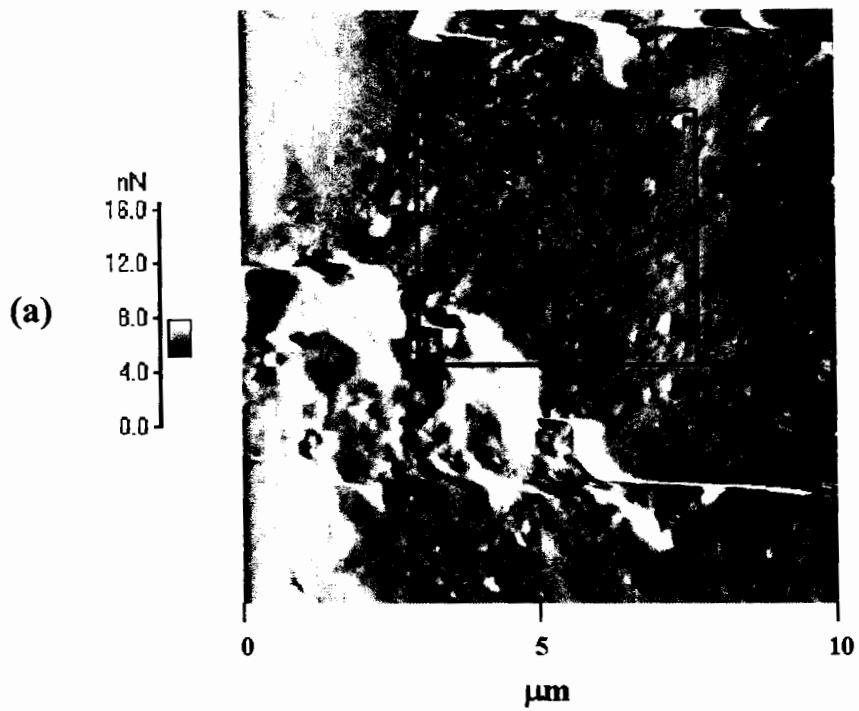


Figure 67. Error signal images [(a) - 10 μm , (b) - 5 μm] of hair treated with PVP/MAPTAC.

friction). This distribution is due to the fact that the regions far from the cuticle edge, lying just below the upper cuticle, are characterized by lower friction (darker coloration). Presumably, the region of the cuticle far from its edge might be less damaged because it is freshly exposed to the environment by the breakage and removal of the upper cuticle.⁵ The smaller (white) peak, higher friction, is in all likelihood due to excessive twisting of the cantilever when traversing over the cuticle step. Smaller imaging areas show more uniform friction maps with narrower pixel distributions. In order to obtain a LFM signal difference value representative of the cuticle surface and not the cuticle edge, we selected the maximum of the histogram peak on the left of the histogram (lower friction). Doing so provides a representative value of signal difference for the majority of the investigated surface, with the exception of the cuticle edge.

In normal practice, the LFM signal is a voltage differential corresponding to the side-to-side deflection of the reflected laser beam. In principle, by knowing the precise geometry of the instrument optics and torsional force constant of the cantilever, one should be able to calibrate a frictional force for the image. In practice, such details are not well characterized in a typical LFM instrument and one is left with a signal that is only proportional to the frictional force. Nevertheless, one can obtain the relative friction coefficient between different samples, which can then be used for surface characterization. From a classical standpoint, the kinetic frictional force between the tip and surface can be described by:¹⁹⁷

$$F_f = \mu \cdot F_l \quad (18)$$

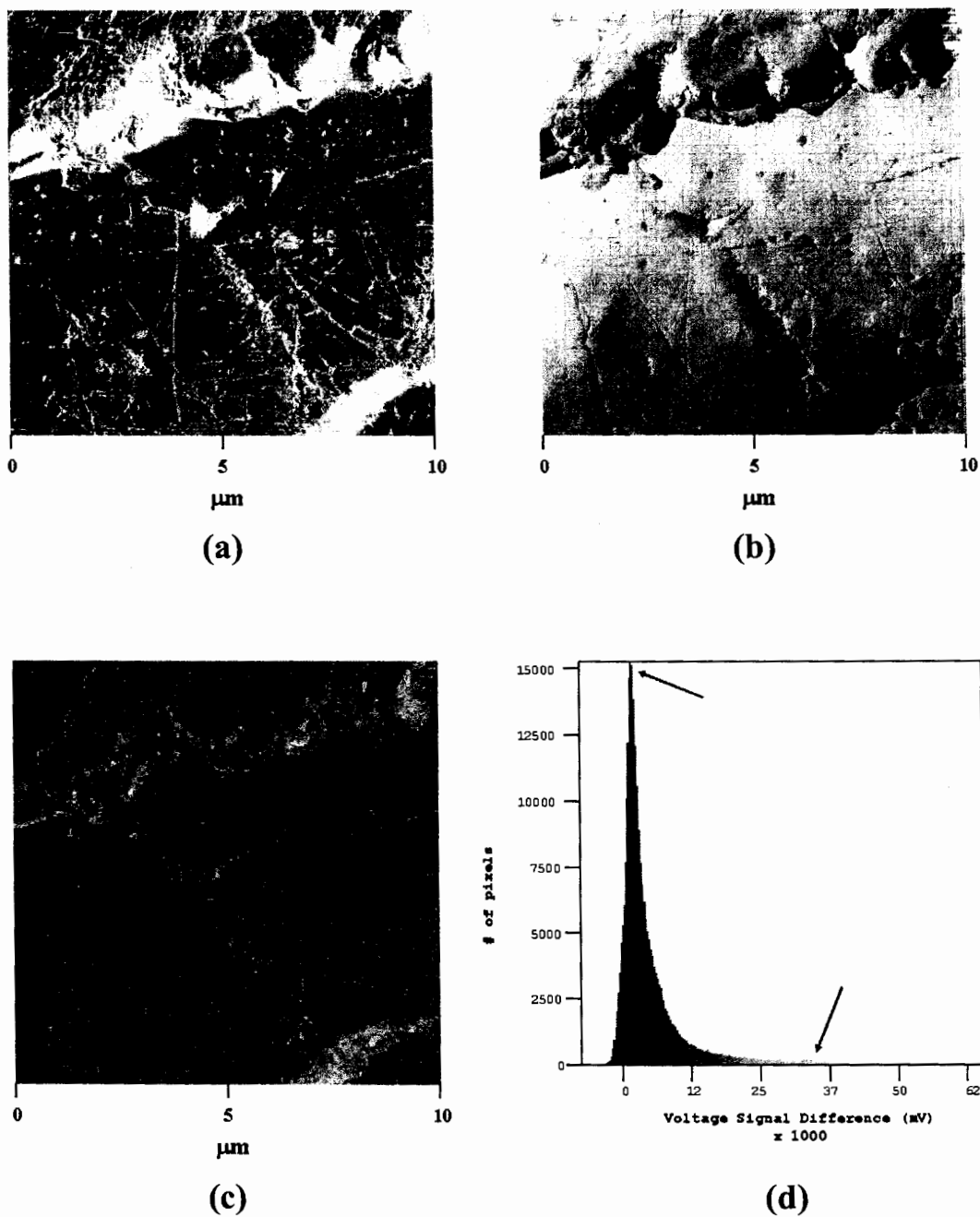


Figure 68. (a) LFM forward, (b) LFM reverse, (c) Difference Image, and (d) Difference Image histogram for a 10 μm scan of solvent extracted hair.

where μ is the friction coefficient (specific for a pair of surfaces), F_l is the loading force (proportional to the setpoint in LFM), and F_f is the frictional force (proportional to the absolute value of the LFM signal). Both F_l and F_f are dependant on the contact area between the tip and sample surface. This dependency is best described on a microscopic level. The contact area between the tip and sample is composed of a collection of weak and transient bonding pairs between the surfaces. The shear force, f , is the force per bond and each bond can be considered to have a particular area, a . The sum of these areas is the contact area and the total shear force for i such bonding pairs is the frictional force:

$$F_f = \sum_i f_i a_i \quad (19)$$

The number of contact points (contact area) is, in turn, dependant on loading force.

$$\sum_i a_i \propto F_l \quad (20)$$

Combining Equations 19 and 20 into Equation 18 removes the area dependence on the friction coefficient. To obtain a measure of the frictional force from LFM data we note that for small angle deflection, the cantilever torsional force constant should be independent of deflection angle. Consequently, the LFM deflection signal should be linearly dependant on frictional force (torsional force on the cantilever).

In differential form, Equation 18 becomes

$$dF_f = \mu dF_l + F_l d\mu \quad (21)$$

For constant μ (valid for small F_l), we obtain for the friction coefficient:

$$\mu = \left(\frac{\partial F_f}{\partial F_l} \right) \propto \left(\frac{\partial |V_{LFM}|}{\partial F_l} \right) \quad (22)$$

Therefore, the slope of a plot for the change in LFM signal vs. loading force (setpoint) will provide a relative measure of the frictional coefficient.

Lateral force measurements in combination with AFM can provide fundamental information about the physical and chemical properties of a surface. Soft materials, such as gels and waxes, allow the tip to penetrate the surface resulting in an increase in drag coefficient, which, in turn, causes the cantilever to experience greater torsion.¹⁹⁸ In contrast, hard crystalline materials restrict tip penetration into the surface resulting in a lower drag coefficient, typically characterized by lower friction. As pointed out above, the measured friction in a given image depends on the coefficient of friction and on the loading force. In order to obtain the relative coefficient of friction, the contribution of the loading force to the measured friction must be evaluated. To do this, the friction on a surface is plotted as a function of loading force. The slope of this plot provides a relative measure of the coefficient of friction between the probe tip and the sample. In practice, a more easily comparable LFM data set is obtained by collecting simultaneous (interlaced) LFM images for the right-to-left and left-to-right scan directions, then subtracting them.

Shown in Figure 69 is a plot of $\Delta(\text{LFM } V)$ vs. loading force. The slope for each hair treatment type is indicated on the plot. Each data set shown in Figure 69 represents the series of data that most closely resemble the average slopes shown in Table II.

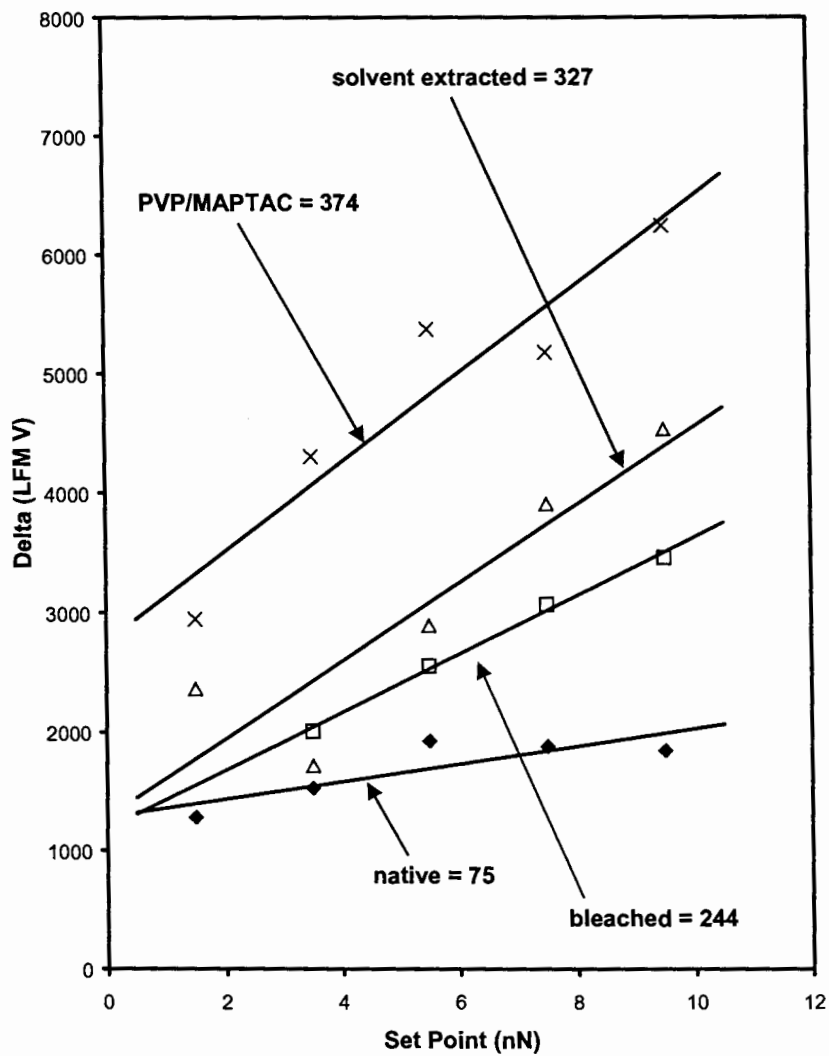


Figure 69. Arbitrary voltage difference as a function of set point (normal force) for various hair treatment protocols. The average slope is reported for each data set.

<u>Type of Hair</u>	<u>Friction Coefficient (μ)</u>	<u>No. of Sites Examined</u>
Native	65 \pm 30	4
Bleached	255 \pm 81	3
Solvent Extracted	265 \pm 92	7
PVP/MAPTAC	383 \pm 124	4

Table II. Friction coefficient for various hair types based on average slopes of $\Delta(\text{LFM V})$ versus loading force plots.

The standard deviation for each point is indicative of that obtained for an entire image (512 X 512 pixels) and is acquired by taking the width of the large peak in the histogram such as the one shown in Figure 68d. Therefore, each point on the chart in Figure 6 represents an average of 262,144 difference values exclusive of the extremely large difference values, which correspond to excessive twisting of the cantilever at the cuticle edge (small peak in the histogram). The slopes reported in Table II represent the average obtained for different regions on four or more hair fibers. The data set in Figure 69 is representative of all the data recorded, for which the average values are provided in Table II. We also note that, in general, the friction vs. load plots do not pass through the origin as expected from theory. This effect results from variations in imaging conditions from one fiber to another and from one location on a given fiber to another. The slopes, which are related to the friction coefficients, are not affected by these variations in imaging conditions and thus, provide a reliable measure of relative friction. The plot of the native fiber resulted in the smallest slope followed by bleached, solvent extracted, and polymer treated hair. These results are consistent with dry combing values obtained experimentally with a Dia-Stron Miniature Tensile Tester,¹ which measures the force

required to comb through a bulk of hair fibers, in essence providing information with regard to inter-fiber friction. The slope of the copolymer is considerably higher than the other fiber types. The cationic copolymer is commonly used as a conditioning styling aid in the personal care industry and is known to preferentially bind to the negative fiber surface by coulombic interactions. As previously shown,¹ the copolymer will increase dry combing forces and, conversely, decrease wet combing forces. This conditioning effect is apparently not related to surface friction but more likely a result of reducing the capillary forces inherent in bundles of wet fibers. The bulk effect is unrelated to the details of the surface except in relation to wettability. The overall finding of increased surface friction as a result of increased exposure of the nanopores on the fiber surface, in the case of extracted and bleached hair, or as a result of excess coverage with a soft polymer is consistent with expectations, since the LFM experiments were performed with the fibers in the dry state.

In all materials studied, we find that the effects of increased friction are invariably due to local effects of the fiber surface and not to large-scale effects involving the cuticle geometry. Small surface features with the appearance of pores are evident in all samples but are more prevalent in the extracted samples indicating that removal of surface oils results in exposure of the pores. The pores are currently believed to be natural features of the fiber surface. The quantitative data obtained from the measurements of the LFM signal as a function of loading force allowed an estimation of a parameter related to fiber-probe friction. This parameter is found to correlate well with macroscopic combing analysis.

References

Never have we been so connected, yet so out of touch.

Ms. Kristen M. Pesci

- (1) McMullen, R. L.; Jachowicz, J.; Kelty, S. P. *IFSCC Magazine* **2000**, 3, 2.
- (2) McMullen, R. L.; Kelty, S. P. *Scanning* **2000**, 23, 337.
- (3) Jones, L. N.; Rivett, D. E. *Micron* **1997**, 28, 469.
- (4) Swift, J. A. Morphology and histochemistry of human hair. In *Formation and Structure of Human Hair*; Jolles, P., Zahn, H., Hocker, H., Eds.; Birkhauser Verlag: Basel, 1997; pp 149.
- (5) Swift, J. A. *J. Cosmet. Sci.* **1999**, 50, 23.
- (6) Wertz, P. W. Integral lipids of hair and stratum corneum. In *Formation and Structure of Human Hair*; Jolles, P., Zahn, H., Hocker, H., Eds.; Birkhauser Verlag: Basel, 1997; pp 227.
- (7) Breakspear, S.; Smith, J. R.; Luengo, G. *J. Struct. Biol.* **2004**, *In Press*.
- (8) Smith, J. R.; Swift, J. A. *Micron* **2004**, *In Press*.
- (9) Nunn, J. R. *J. Chem. Soc.* **1951**, 154, 1740.
- (10) Cundy, D. J.; Gurr, P. A. *Org. Prep. Proced. Int.* **2000**, 32, 461.
- (11) Naito, S.; Sakamoto, K.; Yoshino, K.; Morita, K.; Sugita, J. EP 0 483 689 A1. In *European Patent Office*; European Patent Office: Japan, 1992; pp 1.
- (12) Smith, J. R.; Hill, M. A. W.; Swift, J. A. *Internet J. Chem.* **2002**, 5, 3.
- (13) Fainerman, V. B.; Vollhardt, D.; Roth, A.; Fricke, M.; Volkmer, D. *Journal of Physical Chemistry B* **2004**, 108, 16163.
- (14) Johann, R.; Vollhardt, D. *Materials Science & Engineering, C: Biomimetic and Supramolecular Systems* **1999**, C8-C9, 35.
- (15) Johann, R.; Symietz, C.; Vollhardt, D.; Brezesinski, G.; Moehwald, H. *Journal of Physical Chemistry B* **2000**, 104, 8512.
- (16) Kenn, R. M.; Bohm, C.; Bibo, A. M.; Peterson, I. R.; Mohwald, H.; Als-Nielsen, J.; Kjaer, K. *J. Phys. Chem.* **1991**, 95, 2092.
- (17) Kjaer, K.; Als-Nielsen, J.; Helm, C. A.; Tippman-Krayer, P.; Mohwald, H. *J. Phys. Chem.* **1989**, 93, 3200.
- (18) Le Calvez, E.; Blaudez, D.; Buffeteau, T.; Desbat, B. *Langmuir* **2001**, 17, 670.
- (19) Petrov, J. G.; Pfohl, T.; Moehwald, H. *Journal of Physical Chemistry B* **1999**, 103, 3417.
- (20) Riviere, S.; Henon, S.; Meunier, J.; Schwartz, D. K.; Tsao, M. W.; Knobler, C. M. *Journal of Chemical Physics* **1994**, 101, 10045.
- (21) Schwartz, D. K.; Knobler, C. M. *J. Phys. Chem.* **1993**, 97, 8849.
- (22) Langmuir, I. *J. Am. Chem. Soc.* **1917**, 39, 1848.
- (23) Tredgold, R. H. *Order in Thin Organic Films*; University Press: Cambridge, 1994.
- (24) Petty, M. C. *Langmuir-Blodgett Films*; University Press: Cambridge, 1996.
- (25) Ulman, A. *An Introduction to Ultrathin Organic Films*; Academic Press: London, 1991.
- (26) Gaines, G. W. *Insoluble Monolayers at Liquid-Gas Interfaces*; John Wiley & Sons: New York, 1966.
- (27) Nutting, G. C.; Harkins, W. D. *J. Am. Chem. Soc.* **1939**, 61, 1180.
- (28) Siepman, J. I.; McDonald, I. R. *Mol. Phys.* **1992**, 75, 255.
- (29) Siepman, J. I.; McDonald, I. R. *Phys. Rev. Lett.* **1993**, 70, 453.
- (30) Siepman, J. I. *Tenside, Surfactants, Deterg.* **1993**, 30, 247.
- (31) Siepman, J. I.; McDonald, I. R. *Mol. Phys.* **1993**, 79, 457.

- (32) Siepmann, J. I.; McDonald, I. R. *Langmuir* **1993**, *9*, 2351.
- (33) Siepmann, J. I. *Tribol. Lett.* **1995**, *1*, 191.
- (34) Siepmann, J. I.; McDonald, I. R. *Thin Films* **1998**, *24*, 205.
- (35) Hautman, J.; Klein, M. L. *J. Chem. Phys.* **1989**, *91*, 4994.
- (36) Hautman, J.; Klein, M. L. *J. Chem. Phys.* **1990**, *93*, 7483.
- (37) Hautman, J.; Bareman, J. P.; Mar, W.; Klein, M. L. *J. Chem. Soc., Faraday Trans.* **1991**, *87*, 2031.
- (38) Mar, W.; Klein, M. L. *Langmuir* **1994**, *10*, 188.
- (39) Schmid, F.; Stadler, C.; Duchs, D. *J. Phys.: Condens. Matter* **2001**, *13*, 8653.
- (40) Pal, B.; Modak, S.; Datta, A. *Surf. Sci* **1994**, *310*, 407.
- (41) Schmid, F.; Stadler, C.; Lange, H. *Colloids Surfaces A: Physicochem. Eng. Aspects* **1999**, *149*, 301.
- (42) Harris, J.; Rice, S. A. *Journal of Chemical Physics* **1988**, *89*, 5898.
- (43) Duchs, D.; Schmid, F. *J. Phys.: Condens. Matter* **2001**, *13*, 4853.
- (44) Dhathathreyan, A.; Collins, S. J. *Langmuir* **2002**, *18*, 928.
- (45) Opps, S. B.; Yang, B.; Gray, C. G.; Sullivan, D. E. *Phys. Rev. E* **2001**, *63*, 41602.
- (46) Polimeno, A.; Marijin Ros, J.; Levine, Y. K. *J. Chem. Phys.* **2001**, *115*, 6185.
- (47) Nielsen, S. O.; Lopez, C. F.; Moore, P. B.; Shelley, J. C.; Klein, M. L. *Journal of Physical Chemistry B* **2003**, *107*, 13911.
- (48) Karaborni, S.; Toxvaerd, S. *Journal of Chemical Physics* **1992**, *96*, 5505.
- (49) Karaborni, S.; Toxvaerd, S.; Olsen, O. H. *Journal of Physical Chemistry* **1992**, *96*, 4965.
- (50) Karaborni, S.; Toxvaerd, S. *Journal of Chemical Physics* **1992**, *97*, 5876.
- (51) Karaborni, S. *Langmuir* **1993**, *9*, 1334.
- (52) Cardini, G.; Bareman, J. P.; Klein, M. L. *Chemical Physics Letters* **1988**, *145*, 493.
- (53) Higashino, H.; Mizoguchi, E.; Ogawa, K. *Jpn. J. Appl. Phys.* **1997**, *36*, 319.
- (54) Momose, A.; Hirai, Y. *Thin Solid Films* **1991**, *204*, 175.
- (55) Moller, M. A.; Tildesley, D. J.; Kim, K. S.; Quirke, N. *Journal of Chemical Physics* **1991**, *94*, 8390.
- (56) Kim, K. S.; Moller, M. A.; Tildesley, D. J.; Quirke, N. *Molecular Simulation* **1994**, *13*, 77.
- (57) Bareman, J. P.; Cardini, G.; Klein, M. L. *Phys. Rev. Lett.* **1988**, *60*, 2152.
- (58) Bareman, J. P.; Cardini, G.; Klein, M. L. *Materials Research Society Symposium Proceedings* **1989**, *141*, 411.
- (59) Bareman, J. P.; Klein, M. L. *Journal of Physical Chemistry* **1990**, *94*, 5202.
- (60) Tieleman, D. P.; Marrink, S. J.; Berendsen, H. J. C. *Biochim. Biophys. Acta* **1997**, *1331*, 235.
- (61) <http://www.clinic-clinic.com>.
- (62) Merz, K. M.; Roux, B. *Biological Membranes: A Molecular Perspective from Computation and Experiment*; Birkhäuser: Boston, 1996.
- (63) Disalvo, E. A.; Simon, S. A. *Permeability and Stability of Lipid Bilayers*; CRC Press: Boca Raton, 1995.
- (64) Cevc, G.; Marsh, D. *Phospholipid Bilayers: Physical Principles and Models*; John Wiley & Sons: New York, 1987; Vol. 5.

- (65) Katsaras, J.; Gutberlet, T. *Lipid Bilayers Structure and Interactions*; Springer-Verlag: Berlin, 2001.
- (66) White, S. H.; Wiener, M. C. Determination of the Structure of Fluid Lipid Bilayer Membranes. In *Permeability and Stability of Lipid Bilayers*; Disalvo, E. A., Simon, S. A., Eds.; CRC Press: Boca Raton, 1995.
- (67) Nagle, J. F.; Tristram-Nagle, S. Structure and Interactions of Lipid Bilayers: Role of Fluctuations. In *Lipid Bilayers: Structure and Interactions*; Katsaras, J., Gutberlet, T., Eds.; Springer-Verlag: Berlin, 2001.
- (68) Nagle, J. F.; Zhang, R.; Tristram-Nagle, S.; Sun, W.; Petrache, H. I.; Suter, R. M. *Biophys. J.* **1996**, *70*, 1419.
- (69) Nagle, J. F. *Biophys. J.* **1993**, *64*, 1476.
- (70) White, S. H.; Wiener, M. C. The Liquid-Crystallographic Structure of Fluid Lipid Bilayer Membranes. In *Biological Membranes: A Molecular Perspective from Computation to Experiment*; Merz, K. M., Roux, B., Eds.; Birkhäuser: Boston, 1996; pp 127.
- (71) Tristram-Nagle, S.; Nagle, J. F. *Chem. Phys. Lipids* **2004**, *127*, 3.
- (72) Nagle, J. F.; Tristram-Nagle, S. *Biochim. Biophys. Acta* **2000**, *1469*, 159.
- (73) Petrache, H. I.; Dodd, S. W.; Brown, M. F. *Biophys. J.* **2000**, *79*, 3172.
- (74) Tieleman, D. P.; Berendsen, H. J. C. *Journal of Chemical Physics* **1996**, *105*, 4871.
- (75) Anézo, C.; de Vries, A. H.; Höltje, H.; Tieleman, D. P.; Marrink, S. J. *J. Phys. Chem. B* **2003**, *107*, 9424.
- (76) Patra, M.; Karttunen, M.; Hyvönen, M. T.; Falck, E.; Lindqvist, P.; Vattulainen, I. *Biophys. J.* **2003**, *84*, 3636.
- (77) Patra, M.; Karttunen, M.; Hyvönen, M. T.; Falck, E.; Vattulainen, I. *J. Phys. Chem. B* **2004**, *108*, 4485.
- (78) Shinoda, W.; Okazaki, S. *J. Chem. Phys.* **1998**, *109*, 1517.
- (79) Petrache, H. I.; Tu, K.; Nagle, J. F. *Biophys. J.* **1999**, *76*, 2479.
- (80) Tüchsen, E.; Jensen, M. Ø.; Westh, P. *Chem. Phys. Lipids* **2003**, *123*, 107.
- (81) Berger, O.; Edholm, O.; Jahnig, F. *Biophys. J.* **1997**, *72*, 2002.
- (82) Feller, S.; Venable, R. M.; Pastor, R. W. *Langmuir* **1997**, *13*, 6555.
- (83) Tu, K.; Tobias, D. J.; Klein, M. L. *Biophys. J.* **1995**, *69*, 2558.
- (84) Feller, S.; Pastor, R. W.; Rojnuckarin, A.; Bogusz, S.; Brooks, B. R. *J. Phys. Chem.* **1996**, *100*, 17011.
- (85) Feller, S. E.; MacKerell, A. D. *J. Phys. Chem. B* **2000**, *104*, 7510.
- (86) Chiu, S. W.; Jakobsson, E.; Subramaniam, S.; Scott, H. L. *Biophys. J.* **1999**, *77*, 2462.
- (87) Smondyrev, A. M.; Berkowitz, M. L. *J. Chem. Phys.* **1999**, *110*, 3981.
- (88) Smondyrev, A. M.; Berkowitz, M. L. *Biophys. J.* **1999**, *76*, 2472.
- (89) Smondyrev, A. M.; Berkowitz, M. L. *Biophys. J.* **1999**, *77*, 2075.
- (90) Tu, K.; Klein, M. L.; Tobias, D. J. *Biophys. J.* **1998**, *75*, 2147.
- (91) Lee, B. W.; Faller, R.; Sum, A. K.; Vattulainen, I.; Patra, M.; Karttunen, M. *Fluid Phase Equil.* **2004**, *225*, 63.
- (92) Kyrikou, I.; Georgopoulos, A.; Hatziantoniou, S.; Mavromoustakos, T.; Demetzos, C. *Chem. Phys. Lipids* **2005**, *133*, 125.
- (93) Essmann, U.; Perera, L.; Berkowitz, M. L. *Langmuir* **1995**, *11*, 4519.

- (94) Shinoda, W.; Shimizu, M.; Okazaki, S. *J. Phys. Chem. B* **1998**, *102*, 6647.
- (95) Sachs, J. N.; Petrache, H. I.; Woolf, T. B. *Chem. Phys. Lipids* **2003**, *126*, 211.
- (96) Marrink, S. J.; Lindahl, E.; Edholm, O.; Mark, A. E. *J. Am. Chem. Soc.* **2001**, *123*, 8638.
- (97) Marrink, S.-J.; Berger, O.; Tieleman, P.; Jahnig, F. *Biophys. J.* **1998**, *74*, 931.
- (98) Lindahl, E.; Edholm, O. *J. Chem. Phys.* **2001**, *115*, 4938.
- (99) Feller, S. E.; Pastor, R. W. *J. Chem. Phys.* **1999**, *111*, 1281.
- (100) Feller, S. E.; Pastor, R. W. *Biophys. J.* **1996**, *71*, 1350.
- (101) Feller, S.; Zhang, Y.; Pastor, R. W. *J. Chem. Phys.* **1995**, *103*, 10267.
- (102) Gurtovenko, A. A.; Patra, M.; Karttunen, M.; Vattulainen, I. *Biophys. J.* **2004**, *86*, 3461.
- (103) Costigan, S. C.; Booth, P. J.; Templer, R. H. *Biochem. Biophys. Acta* **2000**, *1468*, 41.
- (104) Damodaran, K. V.; Merz, K. M. *Biophys. J.* **1994**, *66*, 1076.
- (105) Smondyrev, A. M.; Berkowitz, M. L. *J. Chem. Phys.* **1999**, *111*, 9864.
- (106) Chanda, J.; Bandyopadhyay, S. *Chem. Phys. Lett.* **2004**, *392*, 249.
- (107) Bernèche, S.; Nina, M.; Roux, B. *Biophys. J.* **1998**, *75*, 1603.
- (108) Smondyrev, A. M.; Berkowitz, M. L. *Biophys. J.* **2001**, *80*, 1649.
- (109) Pasenkiewicz-Gierula, M.; Takaoka, Y.; Miyagawa, H.; Kitamura, K.; Kusumi, A. *J. Phys. Chem. A* **1997**, *101*, 3677.
- (110) Pasenkiewicz-Gierula, M.; Takaoka, Y.; Miyagawa, H.; Kitamura, K.; Kusumi, A. *Biophys. J.* **1999**, *76*, 1228.
- (111) Ohta-Lino, S.; Pasenkiewicz-Gierula, M.; Takaoka, Y.; Miyagawa, H.; Kitamura, K.; Kusumi, A. *Biophys. J.* **2001**, *81*, 217.
- (112) Balali-Mood, K.; Harroun, T. A.; Bradshaw, J. P. *Eur. Phys. J. E* **2003**, *12*, S135.
- (113) Mashi, R. J.; Scott, H. L.; Subramaniam, S.; Jakobsson, E. *Biophys. J.* **2001**, *81*, 3005.
- (114) Feller, S. E.; Yin, D.; Pastor, R. W.; MacKerell, A. D. *Biophys. J.* **1997**, *73*, 2269.
- (115) Heller, H.; Schaefer, M.; Schulten, K. *J. Phys. Chem.* **1993**, *97*, 8343.
- (116) Shinoda, W.; Mikami, M.; Baba, T.; Hato, M. *Chem. Phys. Lett.* **2004**, *390*, 35.
- (117) Feller, S. E.; Gawrisch, K.; MacKerell, D. *J. Am. Chem. Soc.* **2001**, *124*, 318.
- (118) Hyvönen, M. T.; Rantala, T. T.; Ala-Korpela, M. *Biophys. J.* **1997**, *73*, 2907.
- (119) Saiz, L.; Klein, M. L. *Biophys. J.* **2001**, *81*, 204.
- (120) Ash, W. L.; Zlomislic, M. R.; Oloo, E. O.; Tieleman, D. P. *Biochim. Biophys. Acta* **2004**, *1666*, 158.
- (121) van der Ploeg, P.; Berendsen, H. J. C. *J. Chem. Phys.* **1982**, *76*, 3271.
- (122) Kox, A. J.; Michels, J. P. J.; Wiegel, F. W. *Nature* **1980**, *287*, 317.
- (123) Chiu, S. W.; Clark, M. M.; Jakobsson, E.; Subramaniam, S.; Scott, H. L. *J. Phys. Chem. B* **1999**, *103*.
- (124) Tobias, D. J. *Curr. Opin. Structur. Biol.* **2001**, *11*, 253.
- (125) Granfeldt, M. K.; Miklavic, S. J. *J. Phys. Chem.* **1991**, *95*, 6351.
- (126) Lenz, O.; Schmid, F. *J. Mol. Liq.* **2005**, *117*, 147.
- (127) Pandit, S. A.; Berkowitz, M. L. *Biophys. J.* **2002**, *82*, 1818.
- (128) Raghavan, K.; Rami Reddy, M.; Berkowitz, M. L. *Langmuir* **1992**, *8*, 233.
- (129) Marrink, S. J.; Berkowitz, M. L.; Berendsen, H. J. C. *Langmuir* **1993**, *9*, 3122.
- (130) Goetz, R.; Lipowsky, R. *J. Chem. Phys.* **1998**, *108*, 7397.

- (131) Roux, B. *Biophys. J.* **1996**, *71*, 1346.
- (132) Jahnig, F. *Biophys. J.* **1996**, *71*, 1348.
- (133) Marrink, S. J.; Mark, A. E. *J. Phys. Chem. B* **2001**, *105*, 6122.
- (134) Marrink, S. J.; Tieleman, D. P. *J. Am. Chem. Soc.* **2001**, *123*, 12383.
- (135) Marrink, S. J.; Tieleman, D. P. *Biophys. J.* **2002**, *83*, 2386.
- (136) van Gunsteren, W. F.; Mark, A. E. *J. Chem. Phys.* **1998**, *108*, 6109.
- (137) Benz, R. W.; Castro-Román, F.; Tobias, D. J.; White, S. H. *Biophys. J.* **2005**, *88*, 805.
- (138) Mouritsen, O. G.; Jorgensen, K. *Curr. Opin. Struct. Biol.* **1997**, *7*, 518.
- (139) Pasenkiewicz-Gierula, M.; Murzyn, K.; Rog, T.; Czaplewski, C. *Acta Biochim. Pol.* **2000**, *47*, 601.
- (140) Feller, S. E. *Curr. Opin. Colloid Interface Sci.* **2000**, *5*, 217.
- (141) Merz, K. M. *Curr. Opin. Struct. Biol.* **1997**, *7*, 511.
- (142) Forrest, L. R.; Sansom, M. S. P. *Curr. Opin. Struct. Biol.* **2000**, *10*, 174.
- (143) Scott, H. L. *Curr. Opin. Struct. Biol.* **2002**, *12*, 495.
- (144) Allen, M. P.; Tildesley, D. J. *Computer Simulation of Liquids*; University Press: Oxford, 1987.
- (145) Frenkel, D.; Smit, B. *Understanding Molecular Simulation From Algorithms to Applications*; Academic Press: San Diego, 1996.
- (146) Rapaport, D. C. *The Art of Molecular Dynamics Simulation*; University Press: Cambridge, 1995.
- (147) Leach, A. R. *Molecular Modelling Principles and Applications*; Addison Wesley Longman Limited: Harlow, UK, 1996.
- (148) Cramer, C. J. *Essentials of Computational Chemistry Theories and Models*; John Wiley & Sons: West Sussex, 2002.
- (149) Berendsen, H. J. C.; Postma, J. P. M.; DiNola, A.; Haak, J. R. *J. Chem. Phys.* **1984**, *81*, 3684.
- (150) Nosé, S. *Mol. Phys.* **1984**, *52*, 255.
- (151) Hoover, W. G. *Phys. Rev. A* **1985**, *31*, 1695.
- (152) van der Spoel, D.; van Buuren, A. R.; Apol, E.; Meulenhoff, P. J.; Tieleman, D. P.; Sijbers, A. L. T. M.; Hess, B.; Feenstra, K. A.; Lindahl, E.; van Drunen, R.; Berendsen, H. J. C. *Gromacs User Manual version 3.0*; University of Groningen: Groningen, 2001.
- (153) Nosé, S.; Klein, M. L. *Mol. Phys.* **1983**, *50*, 1055.
- (154) Parrinello, M.; Rahman, A. *J. Appl. Phys.* **1981**, *52*, 7182.
- (155) Ewald, P. P. *Ann. Phys.* **1921**, *64*, 253.
- (156) Darden, T.; York, D.; Pedersen, L. G. *J. Chem. Phys.* **1993**, *98*, 10089.
- (157) Essmann, U.; Perera, L.; Berkowitz, M. L.; Darden, T.; Lee, H.; Pedersen, L. G. *J. Chem. Phys.* **1995**, *103*, 8577.
- (158) Berendsen, H. J. C.; van der Spoel, D.; van Drunen, R. *Comput. Phys. Commun.* **1995**, *91*, 43.
- (159) Lindahl, E.; Hess, B.; van der Spoel, D. *J. Mol. Mod.* **2001**, *7*, 306.
- (160) Schuettelkopf, A. W.; van Aalten, D. M. F. *Acta Cryst.* **2004**, *D60*, 1355.
- (161) Tieleman, D. P. <http://moose.bio.ucalgary.ca/>, 2004.
- (162) Ahlström, P.; Berendsen, H. J. C. *Journal of Physical Chemistry* **1993**, *97*, 13691.

- (163) van Buuren, A. R.; Marrink, S. J.; Berendsen, H. J. C. *J. Phys. Chem.* **1993**, *97*, 9206.
- (164) Berendsen, H. J. C.; Postma, J. P. M.; van Gunsteren, W. F.; Hermans, J. Interaction models for water in relation to protein hydration. In *Intermolecular Forces*; Pullman, B., Ed.; D. Reidel Publishing Company: Dordrecht, 1981; pp 331.
- (165) Ryckaert, J. P.; Ciccotti, G.; Berendsen, H. J. C. *J. Comp. Phys.* **1977**, *23*, 327.
- (166) Miyamoto, S.; Kollman, P. A. *J. Comp. Chem.* **1992**, *13*, 952.
- (167) Hill, T. L. *Introduction to Statistical Mechanics*; Dover: Mineola, NY, 1986.
- (168) Haile, J. M. *Molecular Dynamics Simulations Elementary Methods*; John Wiley & Sons: New York, 1997.
- (169) Seelig, A.; Seelig, J. *Biochemistry* **1974**, *13*, 4839.
- (170) Essex, J. W.; Hann, M. M.; Richards, W. G. *Phil. Trans. Roy. Soc. Lond. B* **1994**, *344*, 239.
- (171) van Gunsteren, W. F.; Berendsen, H. J. C. GROMOS-87 Manual Biomos BV Nijenborgh 4, 9747 AG Groningen, The Netherlands, 1987.
- (172) Robbins, C. R. *Chemical and Physical Behavior of Human Hair*, 3rd ed.; Springer-Verlag: New York, 1994.
- (173) *Formation and Structure of Human Hair*; Jollès, P.; Zahn, H.; Höcker, H., Eds.; Birkhäuser Verlag: Basel, 1997, pp 261.
- (174) Garcia, M. L.; Epps, J. A.; Yare, R. S.; Hunter, L. D. *J. Soc. Cosmet. Chem.* **1978**, *29*, 155.
- (175) Binnig, G.; Quate, C. F.; Gerber, C. *Phys. Rev. Lett.* **1986**, *56*, 930.
- (176) *STM and AFM in Biology*; Marti, O.; Amrein, M., Eds.; Academic Press: San Diego, 1993.
- (177) Smith, J. R. *Journal of Microscopy* **1998**, *191*, 223.
- (178) Smith, J. R. *J. Soc. Cosmet. Chem.* **1997**, *48*, 199.
- (179) O'Connor, S. D.; Komisarek, K. L.; Baldeschwieler, J. D. *J. Invest. Dermatol.* **1995**, *105*, 96.
- (180) You, H.; Yu, L. *Scanning* **1997**, *19*, 431.
- (181) Goddard, E. D.; Schmitt, R. L. *Cosmet. & Toil.* **1994**, *109*, 55.
- (182) Schmitt, R. L.; Goddard, E. D. *Cosmet. & Toil.* **1994**, *109*, 83.
- (183) Pfau, A.; Hössel, P.; Vogt, S.; Sander, R.; Schrepp, W. *Macromol. Symp.* **1997**, *126*, 241.
- (184) Hössel, P.; Sander, R.; Schrepp, W. *Cosmet. & Toil.* **1996**, *111*, 57.
- (185) Swift, J. A.; Smith, J. R. *Scanning* **2000**, *22*, 310.
- (186) Swift, J. A.; Bews, B. *J. Soc. Cosmet. Chem.* **1976**, *27*, 289.
- (187) Phillips, T. L.; Horr, T. J.; Huson, M. G.; Turner, P. S. *Textile Res. J.* **1995**, *65*, 445.
- (188) Crossley, J. A.; Gibson, C. T.; Mapledoram, L. D.; Huson, M. G.; Myhra, S.; Pham, D. K.; Sofield, C. J.; Turner, P. S.; Watson, G. S. *Micron* **2000**, *31*, 659.
- (189) Parbhu, A. N.; Bryson, W. G.; Lal, R. *Biochemistry* **1999**, *38*, 11755.
- (190) Magonov, S.; Whangbo, M.-H. *Surface Analysis with Scanning Tunneling and Atomic Force Microscopy*; VCH: Weinheim, Germany, 1996.
- (191) Neumeister, J. M.; Ducker, W. A. *Rev Sci Instr* **1994**, *65*, 2527.
- (192) Hamers, R. J. *Journal of Physical Chemistry* **1996**, *100*, 13103.

- (193) Den, B. A.; *J. Rev. Sci. Instrum.* **1990**, *62*, 88.
- (194) Garcia, M., Personal Communication.
- (195) Gloor, M. Determination and Analysis of Sebum on Skin and Hairs. In *Cosmetic Science*; Breuer, M. M., Ed.; Academic Press: London, 1978; Vol. 1; pp 217.
- (196) Hafey, M. J.; Watt, I. C. *J. Colloid Interface Sci.* **1986**, *109*, 181.
- (197) Wiesendanger, R. *Scanning Probe Microscopy and Spectroscopy: Methods and Applications*; Cambridge Univ. Press: Cambridge, 1994.
- (198) Overney, R. M.; Meyer, E.; Frommer, J.; Brodbeck, D.; Luethi, R.; Howald, L.; Guentherodt, H. J.; Fujihira, M.; Takano, H.; Gotoh, Y. *Nature (London)* **1992**, *359*, 133.

Appendix A

Suggested Reading

A banker is a fellow who lends you his umbrella when the sun is shining, but wants it back the minute it begins to rain.

Mark Twain

- (1) Adamson, A. W.; Gast, A. P. *Physical Chemistry of Surfaces*, 6th ed.; John Wiley & Sons: New York, 1997.
- (2) Allen, M. P.; Tildesley, D. J. *Computer Simulation of Liquids*; University Press: Oxford, 1987.
- (3) Ash, W. L.; Zlomislic, M. R.; Oloo, E. O.; Tieleman, D. P. "Computer simulations of membrane proteins," *Biochim. Biophys. Acta* **2004**, *1666*, 158.
- (4) Cevc, G.; Marsh, D. *Phospholipid Bilayers: Physical Principles and Models*; John Wiley & Sons: New York, 1987; Vol. 5.
- (5) Cramer, C. J. *Essentials of Computational Chemistry Theories and Models*; John Wiley & Sons: West Sussex, 2002.
- (6) Feller, S. E. "Molecular dynamics simulations of lipid bilayers," *Curr. Opin. Colloid Interface Sci.* **2000**, *5*, 217.
- (7) Frenkel, D.; Smit, B. *Understanding Molecular Simulation From Algorithms to Applications*; Academic Press: San Diego, 1996.
- (8) Gaines, G. W. *Insoluble Monolayers at Liquid-Gas Interfaces*; John Wiley & Sons: New York, 1966.
- (9) Haile, J. M. *Molecular Dynamics Simulations Elementary Methods*; John Wiley & Sons: New York, 1997.
- (10) Israelachvili, J. *Intermolecular & Surfaces Forces*, 2nd ed.; Academic Press: San Diego, 1992.
- (11) Jones, L. N.; Rivett, D. E. "Role of 18-methyleicosanoic acid in the structure and formation of mammalian hair fibres," *Micron* **1997**, *28*, 469.
- (12) Katsaras, J.; Gutberlet, T. *Lipid Bilayers Structure and Interactions*; Springer-Verlag: Berlin, 2001.
- (13) Leach, A. R. *Molecular Modelling Principles and Applications*; Addison Wesley Longman Limited: Harlow, UK, 1996.
- (14) Petty, M. C. *Langmuir-Blodgett Films*; University Press: Cambridge, 1996.
- (15) Rapaport, D. C. *The Art of Molecular Dynamics Simulation*; University Press: Cambridge, 1995.
- (16) Shaw, D. J. *Colloid & Surface Chemistry*, 4th ed.; Butterworth-Heinemann: Oxford, 1992.
- (17) Siepmann, J. I.; McDonald, I. R. "Simulations of self-assembled monolayers of thiols on gold," *Thin Films* **1998**, *24*, 205.
- (18) Swift, J. A. "Human hair cuticle: Biologically conspired to the owner's advantage," *J. Cosmet. Sci.* **1999**, *50*, 23.
- (19) Tieleman, D. P.; Marrink, S. J.; Berendsen, H. J. C. "A computer perspective of membranes: molecular dynamics studies of lipid bilayer systems," *Biochim. Biophys. Acta* **1997**, *1331*, 235.
- (20) Tredgold, R. H. *Order in Thin Organic Films*; University Press: Cambridge, 1994.
- (21) Ulman, A. *An Introduction to Ultrathin Organic Films*; Academic Press: London, 1991.

Appendix B

Computational Instructions

Curiosity killed the cat, but for a while I was the suspect.

Steven Wright

I. Construction of a Monolayer or Bilayer System

In order to conduct MD simulations for a multi-component molecular system, we first need to construct a molecular structure file, which is typically in the protein databank (PDB) format and provides the Cartesian coordinates of each atom present in the system. This would appear to be a rather trivial procedure for one small molecule, however, a more complicated system such as a monolayer or bilayer requires the use of an enhanced molecular editor program. We have found that the software, Deep View Swiss PDB Viewer 3.7 (GlaxoSmithKline R&D and the Swiss Institute of Bioinformatics), was able to perform most of our tasks, specifically the construction of an 8 x 8 or 16 x 16 fatty acid monolayer as well as a bilayer system of similar dimensions. This software can be found at <http://www.expasy.org/spdbv/>.

In order to construct a monolayer or bilayer system with Swiss PDB Viewer, one must first construct one molecule utilizing CS ChemDraw Ultra 5.0 (Cambridgesoft Corporation). This two-dimensional object can be *copied* to the clipboard in a Windows operating system environment and subsequently *pasted* into another program, namely CS Chem3D Pro 5.0 (Cambridgesoft Corporation). Once transferred to CS Chem3D Pro, the molecule can be saved in PDB format. At this point, the newly constructed PDB file of one molecule can be loaded twice into Swiss PDB Viewer (see Figure 70). With the *Control Panel* shown, the first molecule can be set for viewing but should not be able to move. The second molecule should be set for viewing and for movement. When the second molecule is selected in the *Control Panel*, go to the *Select* menu and choose *All*.

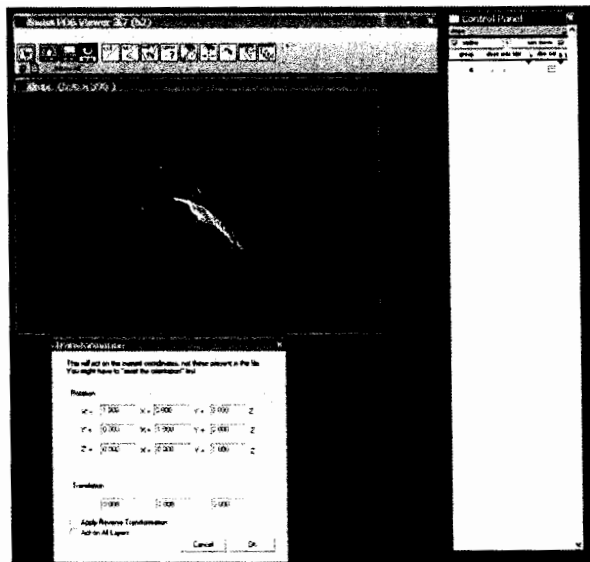


Figure 70. Demonstration of the program Swiss PDB Viewer.

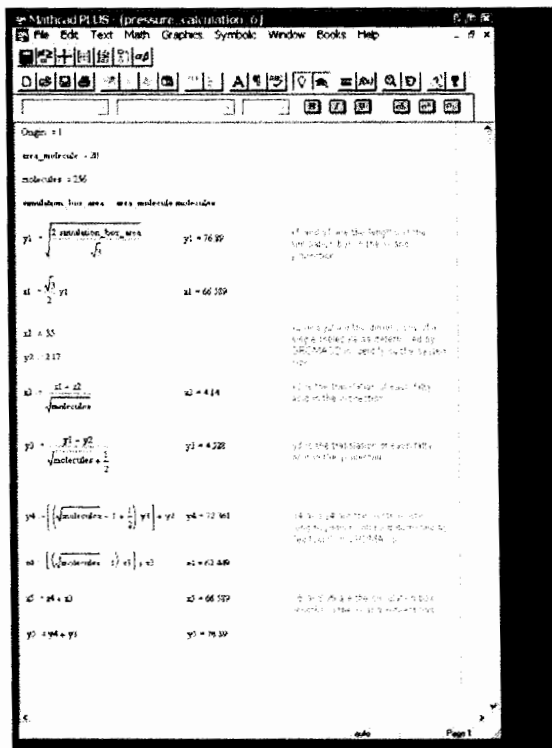


Figure 71. Calculations for simulation box vectors, based on desired packing density, for eicosanoic acid using Mathcad Plus 6.0.

Then go to the *Tools* menu and select *Apply Transformation on Current Layer*. A box should appear on the computer screen as illustrated in Figure 70. In order to translate one of the molecules we need to only put in x or y coordinates. Typically for monolayer systems, we translate along the y coordinate first then in x . After translating a molecule, the two molecules that were superimposed will appear separate. At this point we select each molecule in the *Control Panel* and choose *All* from the *Select* menu. By choosing *Create Merged Layer from Selection* under the *Edit* menu, we can combine the two layers together. The newly formed merged layer can then be saved as a separate layer. This process can be repeated in order to grow the monolayer or bilayer to its required size, for example an 8 x 8 monolayer. In order to calculate the translation of each molecule, several formulas were applied in order to provide a packing arrangement in a hexagonal lattice. This was accomplished using MathCAD Plus 6.0 (Mathsoft, Inc.) and an example is shown in Figure 71. The starting packing density was important for the monolayer systems as we employed the NVT ensemble in the MD simulations. In addition, when constructing the monolayer systems we elected to construct a system in which two monolayers separated by water constitute the entire system as shown in Figure 11 (See Chapter II). We take this approach in order to institute 2D periodic boundary conditions and also to prevent the water from migrating to any vacuum areas of the simulation box. After constructing an 8 x 8 monolayer, we load the monolayer in CS Chem3D Pro and *Save* it as a PDB file. Under the *Tools* menu, there is a *Reflect* option where we can select *Reflect through X-Y Plane*. This structure can then be *Saved* with another title. The non-reflected and reflected structures can then be loaded into Swiss PDB Viewer in

order to manipulate the two monolayers into a structure similar to the one that appears in Figure 11. Typically, we would translate one of the monolayers 76.53 Å along the z-axis.

For the phospholipid bilayers, the same procedure as described above was employed also using Swiss PDB Viewer. Typically, we translated each phospholipid 4.5 Å along the x-axis and 6 Å along the y-axis. After constructing an 8 x 8 phospholipid monolayer, we load the monolayer in CS Chem3D Pro in order to *Save* it as a PDB file. Under the *Tools* menu, there is a *Reflect* option where we can select *Invert through Origin*. This structure can then be saved to another title. Similar to as described above, the non-inverted and inverted structures can then be loaded into Swiss PDB Viewer in order to manipulate the two monolayers into a bilayer structure. Typically, one monolayer was translated 30 Å along the z-axis. The starting packing density is less important with the phospholipid bilayers as the MD simulations were executed using an NPT ensemble. This allows the box size to adjust to the appropriate size, which eventually provides the correct packing density of the bilayer.

For both the monolayer and bilayer systems, a box surrounding the system was constructed and water was added to the box using the programs *Editconf* and *Genbox*, which are part of the GROMACS software package. However, before proceeding to these steps the final PDB file that was constructed in Swiss PDB Viewer is modified using Microsoft® Excel 2002. This step is necessary in order to remove all methyl and methylene hydrogen atoms and to construct a text file with the proper spacing between columns. An example of a modified PDB file that was edited with Microsoft® Excel is

shown in Figure 72. Note that each column width is different, so that when the document is saved in *Format Text (Space Delimited)*, the resulting text file will have the proper column spacing. Table II contains the appropriate column widths and the information each column should contain for the resulting PDB file.

<u>Column</u>	<u>Information</u>	<u>Column Width (spaces)</u>
A	Record Name	7
B	Atom Serial Number	4
C	Atom Name	5.14
D	Residue Name	5.14
E	Residue Serial Number	3
F		5.14
G	Coordinates for X	8.43
H	Coordinates for Y	8.43
I	Coordinates for Z	8.43
J	Occupancy	8.43
K	Temperature Factor	8.43

Table III. Column widths and PDB file information corresponding to Figure 72.

Before formatting the PDB file as described above, we typically would remove all hydrogen atoms from the system that are connected to methylene and methyl groups. This was accomplished by writing macros with Microsoft® Visual Basic 6.3 which is embedded in Microsoft® Excel. An example macro can be found in the Appendix of this text. Once the PDB file was saved to a text document, we could then use it as an input file for the GROMACS programs, *Editconf* and *Genbox*, in order to surround the system with a simulation box and fill it with H₂O. Unfortunately, the program *Genbox* adds water to all empty spaces in the box. Therefore, water may be placed within the monolayer or bilayer as well as above or below it. In order to remove any unwanted

	A	B	C	D	E	F	G	H	I	J	K	L
1	COMPND	DMPDOPPC - 129 Molecule Blayer										
2	ATOM	1	CN1	DMP	1	-1.641	2.540	13.079	1.00	0.00		
3	ATOM	2	NTM	DMP	1	-1.433	1.511	12.084	1.00	0.00		
4	ATOM	3	CN3	DMP	1	-1.678	2.057	10.768	1.00	0.00		
5	ATOM	4	CN2	DMP	1	-2.341	0.413	12.327	1.00	0.00		
6	ATOM	5	CA	DMP	1	-0.070	1.036	12.161	1.00	0.00		
7	ATOM	6	CB	DMP	1	0.148	-0.041	11.119	1.00	0.00		
8	ATOM	7	OA	DMP	1	1.479	-0.470	11.232	1.00	0.00		
9	ATOM	8	P	DMP	1	1.938	-1.629	10.207	1.00	0.00		
10	ATOM	9	OB	DMP	1	0.719	-2.694	10.298	1.00	0.00		
11	ATOM	10	OC	DMP	1	3.391	-2.374	10.788	1.00	0.00		
12	ATOM	11	OD	DMP	1	1.700	-0.939	8.765	1.00	0.00		
13	ATOM	12	OC	DMP	1	2.016	-1.724	7.648	1.00	0.00		
14	ATOM	13	OD	DMP	1	1.723	-0.900	6.423	1.00	0.00		
15	ATOM	14	OE	DMP	1	0.389	-0.574	6.444	1.00	0.00		
16	ATOM	15	CE	DMP	1	1.975	-1.727	5.190	1.00	0.00		
17	ATOM	16	OG	DMP	1	1.889	-0.921	4.079	1.00	0.00		
18	ATOM	17	C1A	DMP	1	1.898	-1.610	2.951	1.00	0.00		
19	ATOM	18	OH	DMP	1	2.266	-2.799	2.903	1.00	0.00		
20	ATOM	19	C1B	DMP	1	1.990	-0.742	1.756	1.00	0.00		
21	ATOM	20	C1C	DMP	1	1.827	-1.524	0.469	1.00	0.00		
22	ATOM	21	C1D	DMP	1	1.514	-0.638	-0.728	1.00	0.00		
23	ATOM	22	C1E	DMP	1	1.751	-1.420	-2.014	1.00	0.00		
24	ATOM	23	C1F	DMP	1	1.438	-0.534	-3.212	1.00	0.00		
25	ATOM	24	C1G	DMP	1	1.674	-1.316	-4.498	1.00	0.00		
26	ATOM	25	C1H	DMP	1	1.361	-0.430	-5.696	1.00	0.00		
27	ATOM	26	C1I	DMP	1	1.596	-1.212	-6.982	1.00	0.00		
28	ATOM	27	C1J	DMP	1	1.284	-0.326	-8.181	1.00	0.00		
29	ATOM	28	C1K	DMP	1	1.521	-1.108	-9.466	1.00	0.00		
30	ATOM	29	C1L	DMP	1	1.226	-0.222	-10.665	1.00	0.00		
31	ATOM	30	C1M	DMP	1	1.443	-1.004	-11.950	1.00	0.00		
32	ATOM	31	C1N	DMP	1	1.130	-0.118	-13.149	1.00	0.00		
33	ATOM	32	C2A	DMP	1	0.051	0.161	5.370	1.00	0.00		

Figure 72. Example of a PDB file construction using Microsoft Excel.

	A	B	C	D	E	F	G	H	I	J	K	L
1	DMPDOPPC Blayer											
2	15576											
3	1	DMP	CN1	1	3.489	5.105	7.750					
4	1	DMP	NTM	2	3.489	5.002	7.661					
5	1	DMP	CN3	3	3.465	5.057	7.529					
6	1	DMP	CN2	4	3.398	4.893	7.695					
7	1	DMP	CA	5	3.626	4.955	7.668					
8	1	DMP	CB	6	3.547	4.847	7.564					
9	1	DMP	OA	7	3.780	4.804	7.575					
10	1	DMP	P	8	3.826	4.688	7.473					
11	1	DMP	OB	9	3.704	4.583	7.482					
12	1	DMP	OC	10	3.972	4.614	7.531					
13	1	DMP	OD	11	3.803	4.757	7.325					
14	1	DMP	OC	12	3.834	4.679	7.217					
15	1	DMP	OD	13	3.905	4.761	7.095					
16	1	DMP	OE	14	3.688	4.794	7.097					
17	1	DMP	CE	15	3.830	4.679	6.971					
18	1	DMP	OG	16	3.801	4.759	6.860					
19	1	DMP	C1A	17	3.822	4.690	6.747					
20	1	DMP	OH	18	3.859	4.575	6.743					
21	1	DMP	C1B	19	3.792	4.777	6.628					
22	1	DMP	C1C	20	3.815	4.699	6.499					
23	1	DMP	C1D	21	3.784	4.788	6.379					
24	1	DMP	C1E	22	3.808	4.709	6.251					
25	1	DMP	C1F	23	3.776	4.798	6.131					
26	1	DMP	C1G	24	3.800	4.720	6.002					
27	1	DMP	C1H	25	3.789	4.806	5.883					
28	1	DMP	C1I	26	3.792	4.730	5.754					
29	1	DMP	C1J	27	3.761	4.819	5.634					
30	1	DMP	C1K	28	3.785	4.741	5.506					
31	1	DMP	C1L	29	3.753	4.829	5.386					
32	1	DMP	C1M	30	3.777	4.751	5.257					
33	1	DMP	C1N	31	3.746	4.840	5.137					

Figure 73. Example of a GRO file construction using Microsoft Excel.

H₂O molecules, the output text file from *Genbox* can be imported into Microsoft® Excel and we can use another macro to remove any unwanted solvent molecules. An example of this macro is in the Appendix as well.

The format of the Gromos (GRO) file is shown in Figure 73, once again after it has been modified with Microsoft® Excel. Table III contains the format information for this type of file. Also note that this type of file usually contains velocity information, however, this is not shown in the Figure as this is still a starting structure and velocities have not yet been generated. Comment lines begin with a semicolon.

<u>Column</u>	<u>Information</u>	<u>Column Width (spaces)</u>
A	Residue Serial Number	5.29
B	Residue Name	5.29
C	Atom Name	6.29
D	Atom Serial Number	4.29
E	Coordinates for X	8.43
F	Coordinates for Y	8.43
G	Coordinates for Z	8.43

Table IV. Column widths and Gromos file information corresponding to Figure 73.

II. Microsoft® Visual Basic Macros for Microsoft® Excel

Macro to Remove Hydrogen Atoms

```
Sub Macro1()
'
'
For i = 1 To 3970 Step 1
  If Cells(i, 3) = "H" Then
    Range(Cells(i, 1), Cells(i, 9)).Select
    Selection.Delete Shift:=xlUp
    i = i - 1
  End If
End Sub
```

